論文 / 著書情報
Article / Book Information

題目(和文)	液体中でのレーザーアブレーションにより作製されたCeO2ナノ粒子とその光学的および電気化学的特性に関する研究
Title(English)	Study on CeO2 Nanoparticles Prepared by Laser Ablation in Liquid and their Optical and Electrochemical Properties
著者(和文)	Shi Mengqi
Author(English)	Mengqi Shi
出典(和文)	学位:博士(学術), 学位授与機関:東京工業大学, 報告番号:甲第12936号, 授与年月日:2024年9月20日, 学位の種別:課程博士, 審査員:和田 裕之,北本 仁孝,中村 健太郎,細田 秀樹,林 智広
Citation(English)	Degree:Doctor (Academic), Conferring organization: Tokyo Institute of Technology, Report number:甲第12936号, Conferred date:2024/9/20, Degree Type:Course doctor, Examiner:,,,,
学位種別(和文)	博士論文
Type(English)	Doctoral Thesis

Study on CeO_2 Nanoparticles Prepared by Laser Ablation in Liquid and their Optical and Electrochemical Properties

A doctoral dissertation
Submitted to the
Department of Chemical Science and Engineering
School of Materials and Chemical Technology
Tokyo Institute of Technology
In Partial Fulfillment of the Requirements
For the Degree of
Doctor of Philosophy

by

Shi Mengqi

July, 2024

Supervised by

Prof. Hiroyuki Wada

Chapter 1 5

General Introduction 5

1.1 Introduction to CeO_2 Nanoparticles 5

1.1.1 Structure and Application of CeO_2 Nanoparticles 5

1.1.2 Oxygen Vacancies and the Optical Properties 6

1.1.3 Enhancing Electrode Sensitivity Through Oxygen Ion Conduction 8

1.2 Laser Ablation in Liquid Method 9

1.2.1 Synthesis Methods of Nanoparticles 9

1.2.2 Coulombic Explosion [82] 10

1.2.3 Laser Melting in Liquid Process [83] 11

1.3 Objectives 12

References 12

Chapter 2 17

Experiment 17

2.1 Experimental Procedure of Powder Material in LAL Method 17

2.2 Experimental Procedure of LAL Method for Bulk Material with Focused Light 18

2.3 Characterization 19

2.3.1 X-ray Powder Diffraction (XRD) 19

2.3.2 Scanning Electron Microscopy (SEM) 19

2.3.3 Dynamic Light Scattering (DLS) 20

2.3.4 Ultraviolet-Visible Spectroscopy (UV-vis) 20

2.3.5 Energy-Dispersive X-ray Spectroscopy (EDS) 20

2.3.6 Cyclic Voltammetry (CV) 21

References 21

Chapter 3 22

Effect of Laser Fluence on CeO_2 Morphology and Optical Properties 22

3.1 Introduction 22

3.1.1 Categories of Ultraviolet Radiation 22

3.1.2 Damage of Ultraviolet Rays in Different Types 23

3.1.3 Anti-Ultraviolet Materials 24

3.1.4 Principles of UV Absorption 25
3.2 Experiment 26
3.2.1 Controlling of Experimental Conditions 26
3.2.2 Experimental Process 27
3.2.3 Analysis 27
3.3 Results and Discussion 27
3.3.1 Phase Analysis 27
3.3.2 Morphology of CeO_2 NPs Effected on Fluence 28
3.3.3 Discussion of Aggregation Phenomenon with Irradiation Time and Suspension Concentration Affection 31
3.3.4 UV Absorption Properties of Synthesized CeO_2 Nanoparticles 34
3.4 Summary 36
References 36
Chapter 4 38
Effect of Focused Laser Ablation on NPs Production and the Morphology Comparison 38
4.1 Introduction 38
4.2 Experiment 39
4.2.1 Laser Ablation in Liquid Method 39
4.2.2 Precipitation Method 39
4.2.3 Analysis 40
4.3 Results and Discussion 40
4.3.1 Comparison of LAL Method vs. Precipitation Method 40
4.3.2 Filtering Efficiency and Production Calculation 44
4.3.3 Advanced Data Science Techniques for SEM Image Analysis 47
4.4 Summary 48
References 49
Chapter 5 51
Electrochemical Properties of CeO_2 NPs in Modifying the rGO-GCE Electrode 51
5.1 Introduction 51
5.1.1 Ammonia Monitoring in the Biomedical Field 51

5.1.2 Electrochemical Gas Sensor 51
5.1.3 Modification of Graphene Oxide to Reduced Graphene Oxide 52
5.1.4 Synergistic Effect 55
5.2 Experiment 55
5.2.1 Preparation of CeO_2-rGO Nanocomposite 55
5.2.2 Morphology Analysis 56
5.2.3 Electrochemical Analysis 56
5.3 Results and Discussion 57
5.3.1 Characteristic of CeO_2-rGO composite 57
5.3.2 Calculation of Energy Band Gap by UV-vis 63
5.3.3 The Standard Test of Sensitivity for Modified Electrode Coating 65
5.3.4 Sensitivity test of Ammonia by Modified Electrode Coating 68
5.4 Summary 74
References 75
Chapter 6 78
General Conclusion 78
6.1 Conclusion 78
6.1.1 Synthesis of CeO_2 Nanoparticles 78
6.1.2 Morphological and Optical Properties 78
6.1.3 Comparative Analysis with Traditional Methods 79
6.1.4 UV Protection Applications 79
6.1.5 Application in Electrochemical Sensors 79
6.1.6 Summary 80
6.3 Prospect 80
Acknowledgment 83

Chapter 1

General Introduction

1.1 Introduction to CeO_2 Nanoparticles

1.1.1 Structure and Application of CeO_2 Nanoparticles

Cerium dioxide (CeO_2) is a rare earth metal oxide that has garnered significant attention due to its unique physicochemical properties and a wide range of applications [1]. CeO_2 has an energy bandgap of approximately 3.1 eV [2], which allows CeO_2 to participate in various chemical [1,3,4] and physical processes [2,5,6], making it a versatile material in multiple fields.

CeO_2 crystallizes in a cubic fluorite structure (Figure. 1-1), characterized by the space group Fm3m [7]. In this structure, Ce^{4+} ions are situated at the face-centered cubic (FCC) lattice sites, while O^{2-} ions occupy the tetrahedral positions. Each Ce^{4+} ion is coordinated by eight O^{2-} ions with a radius of 0.097 nm [7], creating a stable yet flexible lattice [8]. Also, it is shown that there are two other narrow absorption bands superimposed on this absorption band. The wide absorption band originates from the electronic transition of 2p orbit in O and 4f orbit in Ce, and the other two narrow absorption bands are split by the $4f^1$ spin-orbit of Ce [9]. The relatively lower bandgap of CeO_2, compared to other metal oxides like TiO_2 (3.1 eV vs. 3.23 eV for TiO_2) [10], facilitates easier electronic excitation, enhancing its applicability in various technological applications [11, 12]. A prominent feature of CeO_2 is the presence of oxygen vacancies [13], which significantly impact its physical and chemical behavior. These vacancies enable the redox transformation between Ce^{4+} and Ce^{3+}, greatly enhancing CeO_2's redox properties. The Ce^{4+}/Ce^{3+} redox cycle is vital in many

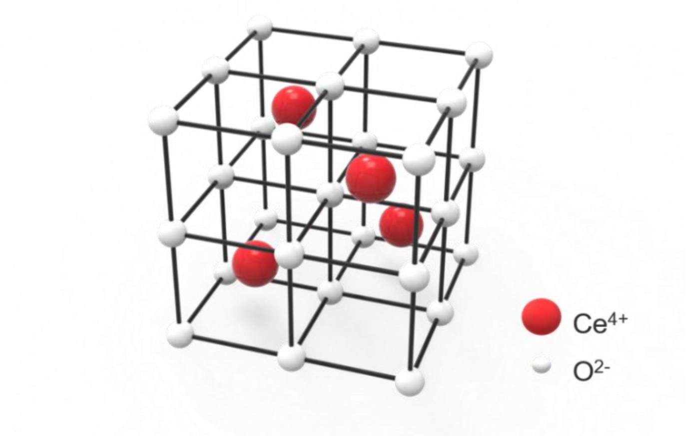

Figure 1-1. Fluorite structure of CeO_2

applications, particularly in catalysis [14, 15], where the ability to switch between oxidation states allows CeO_2 to participate in numerous reactions and environmental remediation processes.

CeO_2 nanoparticles (NPs) exhibit high chemical stability [16], oxidative activity [17], and notable diffusion coefficients for vacancies [18], especially at the nanoscale. These attributes make CeO_2 NPs suitable for a wide range of applications in human-centered science and biomedical fields [19-25]. Notably, their redox properties and high oxygen storage capacity enhance their performance in catalytic processes such as the oxidation of pollutants [19] and the water-gas shift reaction [20]. In the energy sector, CeO_2 NPs are integral to the performance of fuel cells [21] and energy storage devices [22] due to their high ionic conductivity and stability. Additionally, their biocompatibility and ability to modulate oxidative stress make CeO_2 NPs promising candidates for drug delivery systems [23], which are particularly beneficial in treating diseases characterized by oxidative damage, such as cancer [24] and neurodegenerative disorders [25].

However, among these biomedical applications, this research will specifically focus on enhancing the application of CeO_2 NPs in UV protection [26] and biosensors [27]. The ability of CeO_2 to absorb and mitigate the effects of UV radiation makes it an excellent candidate for developing advanced UV protection materials [26, 28]. This includes the creation of more effective sunscreens and protective coatings [29, 30], which can significantly reduce the harmful impacts of UV exposure on human health and materials. Furthermore, the redox properties and surface reactivity of CeO_2 NPs are highly advantageous in the development of biosensors [31, 32]. By harnessing these properties, the research aims to create highly sensitive and selective biosensors capable of detecting ammonia. This kind of ammonia detector have critical applications in medical diagnostics [33] and environmental monitoring [34]. By improving the sensitivity and specificity of CeO_2-based biosensors, this research seeks to advance their practical implementation and effectiveness.

Through a comprehensive exploration of CeO_2's structural properties and functional capabilities, this research aims to enhance the material's application in UV protection and biosensors. By focusing on these specific applications, this research will contribute to the development of advanced CeO_2-based technologies that offer significant benefits in protecting against UV radiation and in the precise detection of analytes in various fields.

1.1.2 Oxygen Vacancies and the Optical Properties

The presence of oxygen vacancies and Ce^{3+} ions significantly alters the electronic structure of CeO_2, influencing its optical properties, particularly in the ultraviolet (UV) region [35]. These oxygen vacancies create mid-gap states [36] within the band structure of CeO_2, which play a crucial role in modifying the material's interaction with

UV radiation.

Oxygen vacancies in CeO_2 introduce localized states within the band gap, commonly referred to as mid-gap states [36]. As shown in Figure 1-2, these states effectively reduce the overall energy band gap of CeO_2. In a CeO_2 crystal theoretically no defects, the band gap is typically wide, which restricts electronic transitions to higher energy UV photons. However, the introduction of oxygen vacancies narrows the band gap [37], making it easier for electrons to be excited into the conduction band [37,38]. The presence of mid-gap states facilitates a two-step transition process for electrons. Initially, electrons are excited from the valence band to these mid-gap states. Subsequently, with additional energy, these electrons can transition from the mid-gap states to the conduction band. This sequential excitation process lowers the effective energy threshold required for electronic transitions [39], thereby increasing the likelihood of electron excitation [40] under UV irradiation.

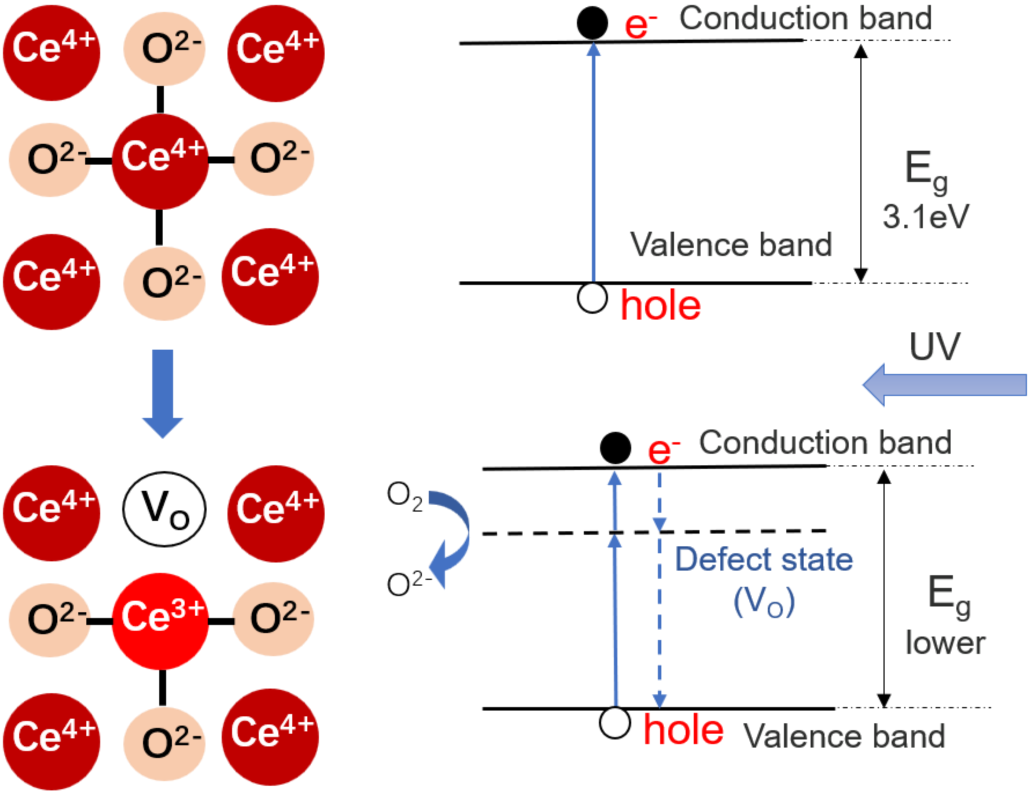

Figure 1-2. UV absorption properties effect on the oxygen vacancies

The creation of mid-gap states due to oxygen vacancies leads to enhanced absorption of UV radiation in CeO_2 [41]. When UV light irradiates the material, electrons can easily transition from the valence band to the mid-gap states and then to the conduction band [38,41]. This two-step excitation mechanism significantly increases the absorption of UV photons compared to the direct transition from the valence band to the conduction band in a defect-free CeO_2 crystal. This increased absorption is not just a matter of quantity but also quality. The energy levels of the mid-gap states are such that they enable a broader range of UV wavelengths to be absorbed. Thus, the presence of oxygen vacancies effectively broadens the absorption spectrum of CeO_2 [42]$_2$, making it a more efficient UV absorber. This phenomenon is useful in applications where extended UV absorption is beneficial, in UV protection applications, materials with a broader UV absorption range provide better protection against a wider spectrum of UV radiation.

1.1.3 Enhancing Electrode Sensitivity Through Oxygen Ion Conduction

The transformation between Ce^{3+} and Ce^{4+} states in cerium dioxide (CeO_2) is inherently unstable, leading to the formation of oxygen ion vacancies [43]. These vacancies are crucial as they facilitate oxygen ion conduction within the material. Oxygen ion conduction occurs through two primary mechanisms [44]: oxygen diffusion in the bulk phase and oxygen incorporation at the surface. In the bulk phase, oxygen ions move through the crystal lattice, while at the surface, oxygen molecules from the gas phase are incorporated into the lattice, becoming oxide ions. This dual mechanism of oxygen diffusion and incorporation is essential for maintaining the overall conductivity of CeO_2 [45].

The conversion of oxygen molecules in the gas phase into oxide ions within the crystalline structure of CeO_2 significantly impacts the material's resistivity [46]. This process effectively transforms chemical signals into electrical signals [47]. When CeO_2 is utilized as an electrode material, these changes in resistivity can enhance the electrode's sensitivity [48]. The improved sensitivity arises from the increased conductivity, which is facilitated by raising the Fermi level [49] — a process commonly achieved through donor doping with CeO_2. Another approach to enhancing the sensitivity of CeO_2-based electrodes involves controlling the structure and size of the nanoparticles [50]. By manipulating the morphology of CeO_2 nanoparticles to increase their surface area, the material's conductivity can be further improved. A larger surface area provides more active sites for oxygen incorporation and diffusion, thereby enhancing the overall oxygen ion conduction [51].

Therefore, the combination of oxygen ion conduction mechanisms and strategic modifications in the nanoparticle structure of CeO_2 plays a pivotal role in improving the sensitivity of electrodes. The unstable transformation between Ce^{3+} and Ce^{4+} creates oxygen ion vacancies, which facilitate oxygen conduction both in the bulk and at the surface. These processes result in changes in resistivity that enhance the conversion of chemical signals to electrical signals, thereby improving electrode sensitivity. Additionally, optimizing the structure and size of CeO_2 nanoparticles to increase their surface area further boosts conductivity and sensitivity.

1.2 Laser Ablation in Liquid Method

Over the past few decades, the pulsed laser ablation (PLA) technique has been recognized for its distinct capabilities in nanocrystal growth [51], thin solid film preparation [52], and other applications [53]. This synthesis method traditionally involves ablating solid targets to produce nanoparticles [54]. In its conventional form, PLA has proven effective for creating nanostructured materials [55], but it also presented limitations, such as the production of unwanted by-products and difficulties in controlling particle size and shape.

To address these issues, researchers have made several modifications to the PLA technique, leading to the development of the Laser Ablation in Liquid (LAL) method. Introduced in 1987 [56], LAL emerged as an efficient way to fabricate nanostructured metal oxides without generating by-products [57]. Compared to other synthesis methods, LAL is a green physical technique that offers controllable parameters [58] and the capability to achieve high temperatures [59], which are essential for manufacturing metastable phases in materials like cerium oxide (CeO_2).

The principle of laser ablation involves using a high-energy laser to eject a significant amount of material from the surface of a target [60]. This process requires short (~10^{-13} to 10^{-8} seconds) and intense (~10^{6} to 10^{14} W/cm^{2}) laser pulses [61]. The high energy from the laser can be delivered in various environments, including vacuum [62], gas [63], and liquid [64], provided that the medium does not excessively attenuate the laser energy. The laser's fluence on the solid surface must be sufficient to drive the material out of its equilibrium state [65], facilitating the formation of nanoparticles.

1.2.1 Synthesis Methods of Nanoparticles

Traditional chemical methods for synthesizing nanoparticles, such as precipitation [66], hydrothermal [67], and sol-gel [70] techniques, have been widely utilized in research (**Table 1**-1). Each method offers its own set of advantages and limitations. For instance, in the precipitation method [66, 71], excessive local heat during the process can cause aggregation, uneven composition, and residual raw materials. The hydrothermal method [67, 72], while effective, requires extremely high temperatures and pressures, making the control of crystal growth challenging. Sol-gel methods involve chemically hazardous raw materials and are time-consuming [73], which can limit their practicality for large-scale production. In contrast, physical methods like the Laser Ablation in Liquid (LAL) technique address many of these shortcomings. LAL is particularly effective in producing nanoparticles with controlled size and shape [74]. This technique involves using a high-energy laser to ablate a solid target material immersed in a liquid medium, creating nanoparticles with high purity and uniformity [75].

Preparation methods		**Particle size (nm)**	**Morphology**
Traditional methods	Precipitation [66]	15	Spherical
	Hydrothermal [67]	5	Octahedral
	Solvothermal [68]	8	Polyhedral
	Spray Pyrolysis [69]	17	Cubic
Laser ablation in liquid method (LAL)		5-100 (controllable)	Spherical

Table 1-1. Synthesis methods of cerium oxide nanoparticles

LAL offers several advantages over traditional methods. Firstly, it can produce nanoparticles with high purity, as the laser ablation process minimizes contamination [76]. Secondly, LAL is versatile and can be applied to a wide range of target materials, including metals [77], semiconductors [78], and ceramics [79]. The method also allows for precise control over the shape and size of the nanoparticles, resulting in highly uniform particles. Additionally, LAL is an environmentally friendly technique [76] as it avoids the use of hazardous chemicals and can be performed under mild conditions. The process of LAL involves directing a laser, such as a YAG laser [80], through a series of optical components like a half-wave plate (HWP) and a polarizing beam splitter (PBS) to precisely target the material [81]. The laser energy causes the target material to evaporate and form a plasma plume in the liquid medium. This rapid cooling of the plasma leads to the formation of nanoparticles. The resulting nanoparticles are typically spherical, with controllable sizes and high uniformity, making them ideal for various applications in catalysis [19], sensors [31], and biomedicine [23]. While traditional methods for nanoparticle synthesis have their own set of challenges, the Laser Ablation in Liquid method provides a superior alternative by producing nanoparticles that are purer, more uniform, and environmentally friendly. The ability to control the size and shape of the nanoparticles makes LAL a highly valuable technique in the field of nanomaterials.

1.2.2 Coulombic Explosion [82]

The principle of Coulombic explosion is crucial for understanding how laser ablation produces nanoparticles. When a high-intensity laser beam is focused onto a target material, such as cerium oxide (CeO_2), the laser's electromagnetic field ionizes the material's surface atoms by stripping away their outer valence electrons. These electrons, responsible for chemical bonding, leave the atoms positively charged. As a result, the positively charged ions experience strong Coulombic repulsion. This repulsion is powerful enough to break the material's cohesive forces, causing it to disintegrate rapidly into a plasma of ionized particles. This phenomenon, known as a

Coulombic explosion, produces a plasma cloud consisting of energetic ions, electrons, and neutral atoms. As the plasma cools, the ions recombine to form nanoparticles. The precise control of laser parameters ensures the production of uniformly small nanoparticles.

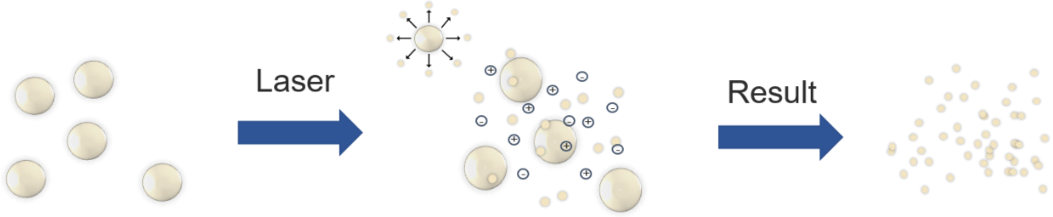

Figure 1-3. schematic of coulombic explosion

1.2.3 Laser Melting in Liquid Process [83]

Another significant principle in LAL is the laser melting process, which is critical for controlling the spherical shape and preventing the aggregation of nanoparticles. This process involves the selective heating of irregularly shaped raw particles dispersed in a liquid medium. Rapid heating from the laser induces the formation of nanobubbles at the surface of the particles, which act as thermal insulators, enhancing the heating process and ensuring uniform temperature distribution. The photothermal effect plays a pivotal role in this process. When the surface temperature of the particles exceeds the spinodal temperature of the nanobubble barrier but remains below the melting point, the particles transform into spherical shapes. The spherical shape is thermodynamically stable, minimizing surface energy and enhancing stability. The laser melting process can be controlled by adjusting laser parameters such as pulse duration and energy, allowing for the production of nanoparticles with precise and uniform shapes and sizes. For CeO_2 nanoparticles, achieving a spherical shape is crucial as it enhances their surface area and catalytic properties.

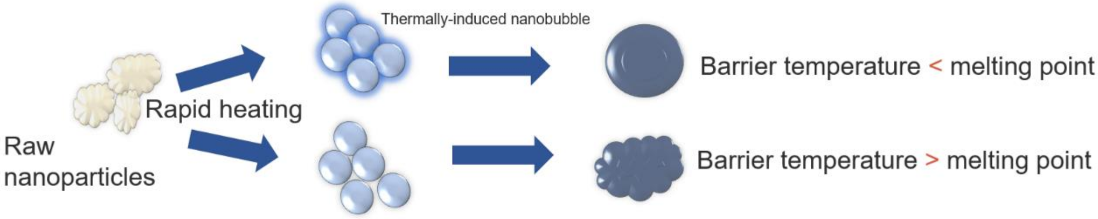

Figure 1-4. Laser Melting in Liquid Process

In summary, the principles of Coulombic explosion and laser melting are fundamental to the effectiveness of LAL in producing small, spherical, and uniform CeO_2 nanoparticles. Coulombic explosion facilitates the initial creation of nanoparticles, while the laser melting process ensures that these particles achieve a controlled spherical shape, enhancing their stability and usability in various applications.

1.3 Objectives

The primary objectives of this research are threefold, focusing on enhancing the synthesis, characterization, and application of CeO_2 nanoparticles (NPs) through the Laser Ablation in Liquid (LAL) method and improving their use in UV protection and biosensors.

Firstly, the study will explore the effects of several parameters (irradiation time, irradiation fluence, and concentration of the suspension) on the synthesis of CeO_2 NPs from powder targets using the LAL method. Especially study on the laser fluence impacts the optical properties of CeO_2 NPs, particularly UV absorption.

Secondly, the research aims to improve the yield of NPs by adjusting the laser process to focused light. This method's advantages will be compared with the traditional chemical precipitation method concerning the morphology of the CeO_2 NPs. The concentration of the NPs post-filtration will be quantified using a calculation method, and advanced data science techniques will be employed to aid in the SEM data analysis.

Lastly, the synthesized CeO_2 NPs will be used to modify the sensitivity of the glassy carbon electrode (GCE) by coating it with a CeO_2/reduced graphene oxide (rGO) composite. This part of the study aims to enhance the sensitivity of NH^{4+} monitoring. During this process, graphene oxide (GO) will be transformed into rGO, and uniform doping with CeO_2 will be achieved. The synergistic effects between CeO_2 and rGO are expected to improve the conductivity and sensitivity of the modified GCE electrode.

These objectives aim to advance the understanding and application of CeO_2 nanoparticles, particularly in UV protection and biosensor technologies, leveraging the unique advantages of the LAL method and the synergistic properties of CeO_2/rGO composites.

References

[1] A. B. Shcherbakov, V. V. Reukov, A. V. Yakimansky, E. L. Krasnopeeva, O. S. Ivanova, A. L. Popov, V. K. Ivanov. *Polymers*, 13 (2021) 924.

[2] Xue-Hong, L., Jian-Min, Z., Jun-Jie, Z., Jing-Zhong, X., Hong-Yuan, C., *Chem. Commun.,* 10, (2001) 937.

[3] Y. Zhang, S. Zhao, J. Feng, S. Song, W. Shi, D. Wang, H. Zhang. *Chem*, 7, 8 (2021) 2022.

[4] C. Chen, S. Zhao, X. Li, T. Tan, W. Liao, H. You. *Colloids Surf. A: Physicochem.*

Eng. Asp., 694 (2024) 134194.

[5] A. Alemayehu, D. Zákutná, T. Wangle, D.N. Rainer, M. Klementová, P. Ecorchard, M. Dopita, M. Cologna, V. Tyrpekl. *J. Eur. Ceram. Soc.*, 44, 5 (2024) 3456.

[6] S. Kurtaran, G. Kilic, S.A.M. Issa, H.O. Tekin. *Ceram. Int.*, 48, 17 (2022) 25041.

[7] V. Levchenko. Green Tribology: New Generation of the Nanostructured Composite Coatings – Orientants in Engineering, Lomonosov Moscow State University, Russia, 09:50-10:30, April 19, 2017.

[8] M. Pan, S. Zhang, Y. Xu, R. *Li. Appl. Surf. Sci.*, 448 (2018) 435.

[9] C. Li, Y. Han, F. Ma. *Adv. Condens. Matter. Phys.*, 28 (2014) 32.

[10] D. Domtau, J. Simiyu, E. Ayieta, B. Muthoka, J. Mwabora. *J. Mater. Phys. Chem.*, 4 (2016) 1.

[11] M. Noor, M.A. Al Mamun, A.K.M. Atique Ullah, A. Matsuda, G. Kawamura, M.A. Hakim, M.F. Islam, M.A. Matin. *J. Phys. Chem. Solids*, 148 (2021) 109751.

[12] X. Wang, J. Wang, Y. Sun, K. Li, T. Shang, Y. Wan. *Front. Chem.*, 10 (2022) 1089708.

[13] W. Zheng, L. Hao, Y. Zhou, B. Gu, Z. Jiang, Y. Fang. *Prog. Org. Coat.,* 192 (2024) 108481.

[14] Z. Su, W. Yang, C. Wang, S. Xiong, X. Cao, Y. Peng, W. Si, Y. Weng, M. Xue, J. Li. *Environ. Sci. Technol.*, 54, 19 (2020) 12684.

[15] L. Wang, Y. Yu, H. He, et al. *Sci. Rep.*, 7 (2017) 12845.

[16] X. Zhuang, E. Magnone, S.W. Han, J.H. Park. *Ceram. Int.*, 50, 13, Part B (2024) 24801.

[17] P. Miceli, S. Bensaid, N. Russo, D. Fino. *Chem. Eng. J.*, 278 (2015) 190.

[18] F. Millot, P. De Mierry. J. *Phys. Chem. Solids,* 46, 7 (1985) 797.

[19] R. Ma, S. Zhang, T. Wen, P. Gu, L. Li, G. Zhao, F. Niu, Q. Huang, Z. Tang, X. Wang. *Catal. Today*, 335 (2019) 20.

[20] T. Shido, Y. Iwasawa. *J. Catal.*, 136, 2 (1992) 493.

[21] L. Yu, J. Xi. *Int. J. Hydrogen Energy*, 37, 21 (2012) 15938.

[22] W. Zhu, Z.-Y. Shen, F. Song, X. Zeng, W. Luo, Z. Wang, Y. Li. *Ceram. Int.*, 50, 11, Part A (2024) 19365.

[23] A. Sanmugam, S. Abbishek, S. Logesh Kumar, A.B. Sairam, V.V. Palem, R. Suresh Kumar, A.I. Almansour, N. Arumugam, D. Vikraman. J. Mech. B*ehav. Biomed. Mater.*, 145 (2023) 106033.

[24] S. Balaraman, B. Iruson, S. Krishnmoorthy, M. Elayaperumal, S. Sangaraju. *Chem. Phys. Impact*, 6 (2023) 100167.

[25] S. Naz, J. Beach, B. Heckert, T. Tummala, O. Pashchenko, T. Banerjee, S. Santra. *Nanomedicine*, 12, 5 (2017) 545.

[26] M. Aklalouch, A. Calleja, X. Granados, S. Ricart, V. Boffa, F. Ricci, T. Puig, X. Obradors. *Sol. Energy Mater. Sol. Cells,* 120, Part A (2014) 175.

[27] A.S. Finny, A. Othman, S. Andreescu. *Metal Oxides*., (2020) 259.

[28] Z. Li, L. Tong, Y. Ma, L. Zhao. *Ceram. Int.*, 50 (2024) 20431.

[29] T. Herrling, M. Seifert, K. Jung. (2013). *Cerium Dioxide: Future UV-filter in Sunscreen?*

[30] M. Aguirre, M. Paulis, J.R. Leiza. Waterborne Acrylic/CeO_2 Nanocomposites for UV Blocking Clear Coats. *IntechOpen*, 2019.

[31] A. Karimi, A. Othman, S. Andreescu. *Methods Enzymol.*, 571 (2016) 177.

[32] N. Pachauri, K. Dave, A. Dinda, P.R. Solanki. *J. Mater. Chem. B*, 6, 19 (2018) 5428.

[33] A.B. Shcherbakov, V.V. Reukov, A.V. Yakimansky, E.L. Krasnopeeva, O.S. Ivanova, A.L. Popov, V.K. Ivanov. *Polymers (Basel),* 13, 6 (2021) 924.

[34] S.B. Khan, M. Faisal, M.M. Rahman, A. Jamal. *Sci. Total Environ.*, 409, 15 (2011) 2987.

[35] B. Choudhury, A. Choudhury. *Mater. Chem. Phys.*, 131, 3 (2012) 666.

[36] H.H. Pham, L.-W. Wang. *Phys. Chem. Chem. Phys.*, 17 (2015) 541.

[37] B. Choudhury, P. Chetri, A. Choudhury. J. Exp. Nanosci., 10, 2 (2013) 103.

[38] T. Sonoda, M. Kinoshita, Y. Chimi, N. Ishikawa, M. Sataka, A. Iwase. Nucl. Instrum. Methods Phys. Res. B, 250, 1–2 (2006) 254.

[39] M. Noor, M.A. Al Mamun, A.K.M. Atique Ullah, A. Matsuda, G. Kawamura, M.A. Hakim, M.F. Islam, M.A. Matin. J. Phys. Chem. Solids, 148 (2021) 109751.

[40] T.S. Wu, L.Y. Syu, C.N. Lin, et al. *Sci. Rep.*, 9 (2019) 8018.

[41] S.A. Ansari, M.M. Khan, M.O. Ansari, S. Kalathil, J. Lee, M.H. *Cho. RSC Adv.*, 4 (2014) 16782.

[42] M. Shi, Y. Kitamoto, M. Hara, et al. *Appl. Phys. A,* 128 (2022) 968.

[43] C.-C. Chou, C.-F. Huang, T.-H. Yeh. *Ceram. Int.*, 39, Suppl. 1 (2013) S627.

[44] V. Metlenko, W. Jung, S.R. Bishop, H.L. Tuller, R.A. De Souza. *Phys. Chem. Chem. Phys.*, 18 (2016) 29495.

[45] T. Suzuki, I. Kosacki, H.U. Anderson, P. Colomban. J. Am. Ceram. Soc., 84, 9 (2001) 2007.

[46] H. Yamamura, S. Takeda, K. Kakinuma. *Solid State Ionics,* 178, 13–14 (2007) 889.

[47] A. Umar, T. Almas, A.A. Ibrahim, R. Kumar, M.S. AlAssiri, S. Baskoutas, M.S. Akhtar. J. *Electroanal. Chem.*, 864 (2020) 114089.

[48] L. Wang, H. Huang, S. Xiao, D. Cai, Y. Liu, B. Liu, D. Wang, C. Wang, H. Li, Y. Wang, Q. Li, T. Wang. *ACS Appl. Mater. Interfaces*, 6, 16 (2014) 14131.

[49] Q. Zhou, S. Zhu, Z. Ma, Y. Liu, L. Liu, L. Gao. *Ceram. Int.*, 48, 8 (2022) 11313.

[50] D. Coetzee, M. Venkataraman, J. Militky, M. Petru. *Polymers*, 12, 4 (2020) 742.

[51] C.X. Wang, P. Liu, H. Cui, G.W. Yang. *Appl. Phys. Lett.*, 87 (2005) 201913.

[52] P. Manoravi, M. Joseph, N. Sivakumar. *J. Phys. Chem. Solids*, 59, 8 (1998) 1271.

[53] W.M. de Azevedo, S. de L. Campello, D.L. da Cunha, L.T.B. de Mendonça, O.M.M.M. da Costa. *Applications of Laser Ablation, Chapter 9* (2016).

[54] Srinivasan, R. and B. Braren, *Chem. Rev.*, 89, 6, 1989.

[55] Z. Yan, D.B. Chrisey. J. Photochem. *Photobiol. C*, 13, 3 (2012) 204.

[56] P.P. Patil, D.M. Phase, S.A. Kulkarni, S.V. Ghaisas, S.K. Kulkarni, S.M. Kanrtkar, et al. *Phys. Rev. Lett.,* 58 (1987) 238.

[57] E. Fazio, B. Gökce, A. De Giacomo, M. Meneghetti, G. Compagnini, M. Tommasini, F. Waag, A. Lucotti, C.G. Zanchi, P.M. Ossi, M. Dell'Aglio, L. D'Urso, M. Condorelli, V. Scardaci, F. Biscaglia, L. Litti, M. Gobbo, G. Gallo, M. Santoro, S. Trusso. *Nanomaterials*, 10, 11 (2020) 2317.

[58] A. Subhan, A.-H.I. Mourad, Y. Al-Douri. *Nanomaterials*, 12, 13 (2022) 2144.

[59] G.W. Yang. *Prog. Mater. Sci*., 52, 4 (2007) 648.

[60] R. Streubel, S. Barcikowski, B. Gökce. *Opt. Lett*., 41 (2016) 1486.

[61] G. Mourou. *Extreme Light Physics and Application. Nobel Lecture*, December 8, 2018.

[62] M.E. Povarnitsyn, T.E. Itina. *Appl. Phys. A*, 117 (2014) 175

[63] D.B. Geohegan, A.A. Puretzky, G. Duscher, S.J. Pennycook. *Appl. Phys. Lett*., 72 (1998) 2987.

[64] T.E. Itina. *J. Phys. Chem. C*, 115, 12 (2011) 5044.

[65] O. Barthélemy, J. Margot, M. Sabsabi. *Appl. Spectrosc.*, 59, 4 (2005) 529.

[66] D.A. Pelletier, A.K. Suresh, G.A. Holton, C.K. McKeown, W. Wang, B. Gu, N.P. Mortensen, D.P. Allison, D.C. Joy, M.R. Allison. *Appl. Environ. Microbiol*., 76 (2010) 7981.

[67] S. Rojas, J.D. Gispert, S. Abad, M. Buaki-Sogo, V.M. Victor, H. Garcia, J.R.L. Herance. *Mol. Pharm*., 9 (2012) 3543.

[68] H. Zhang, X. He, Z. Zhang, P. Zhang, Y. Li, Y. Ma, Y. Kuang, Y. Zhao, Z. Chai. Environ. *Sci. Technol*., 45 (2011) 3725.

[69] P. Demokritou, S. Gass, G. Pyrgiotakis, J.M. Cohen, W. Goldsmith, W. McKinney, D. Frazer, J. Ma, D. Schwegler-Berry, J. Brain. Environ. *Sci. Technol*., 7 (2013) 1338.

[70] A.S. Fudala, W.M. Salih, F.F. Alkazaz. *Mater. Today Proc.*, 49, Part 7 (2022) 2786.

[71] M. Niederberger. Acc. *Chem. Res*., 40, 9 (2007) 793.

[72] J.A. Darr, J. Zhang, N.M. Makwana, X. Weng. *Chem. Rev*., 117, 17 (2017) 11125.

[73] Z. Zhao, Y. Duan. Sens. *Actuators B: Chem.*, 160, 1 (2011) 1340.

[74] S. Scaramuzza, M. Zerbetto, V. Amendola. *J. Phys. Chem. C,* 120, 17 (2016) 9453.

[75] M. Ullmann, S.K. Friedlander, A. Schmidt-Ott. *J. Nanopart. Res*., 4 (2002) 499.

[76] N.G. Semaltianos. *Crit. Rev. Solid State Mater. Sci.,* 35, 2 (2010) 105.

[77] P.V. Kazakevich, A.V. Simakin, G.A. Shafeev. *Quantum Electron*., 35, 9 (2005) 831.

[78] N.G. Semaltianos, S. Logothetidis, W. Perrie, et al. *Appl. Phys. A*, 94 (2009) 641.

[79] C.L. Sajti, R. Sattari, B.N. Chichkov, S. Barcikowski. *J. Phys. Chem. C*, 114, 6 (2010) 2421.

[80] S. Dadashi, R. Poursalehi, H. Delavari. Procedia *Mater. Sci.*, 11 (2015) 722.

[81] N.A. Inogamov, V.V. Zhakhovsky, V.A. Khokhlov. *JETP Lett.*, 115 (2022) 16.

[82] M. Hashida, H. Mishima, S. Tokita, S. Sakabe. *Opt. Express,* 17, 15 (2009) 13116.

[83] Y. Ishikawa, T. Tsuji, S. Sakaki, N. Koshizaki. Prog. *Mater. Sci.*, 131 (2023) 101004.

Chapter 2

Experiment

2.1 Experimental Procedure of Powder Material in LAL Method

The equipment and light path for the Laser Ablation in Liquid (LAL) method are illustrated in Figure 2-1. The experimental procedure for preparing CeO_2 nanoparticles using powder material involves the following steps:

Preparation of CeO_2 Suspension:

CeO_2 suspension liquids were prepared at various concentrations ranging from 200 to 500 µg/mL. High-purity micro-sized CeO_2 powder (Kanto Chemical Co., INC. 99.99%) was added to pure water and continuously stirred in a 200 mL transparent, square-shaped glass bottle.

Laser Ablation Setup:

The Nd: YAG laser (Spectron Laser Systems Ltd., SL8585G) was utilized as the light source for the ablation process. The laser operated at a wavelength of 532 nm with a frequency of 10 Hz, a maximum output power of 3.6 W, and an energy of 360 mJ per pulse. The pulse width was measured to be 13 ns. The laser beam was split using a polarized beam splitter (PBS), and the highest laser fluence was adjusted to 300 mJ/cm² using a remote controller and measured with a half-wave plate (HWP). Neutral-density filters (ND filters) of 25% and 50% were employed to achieve fluences of 150 mJ/cm² and 75 mJ/cm², respectively.

Ablation Process:

The prepared CeO_2 suspension was subjected to laser ablation for various durations. During this process, the laser beam was directed into the suspension, resulting in the formation of CeO_2 nanoparticles under different conditions.

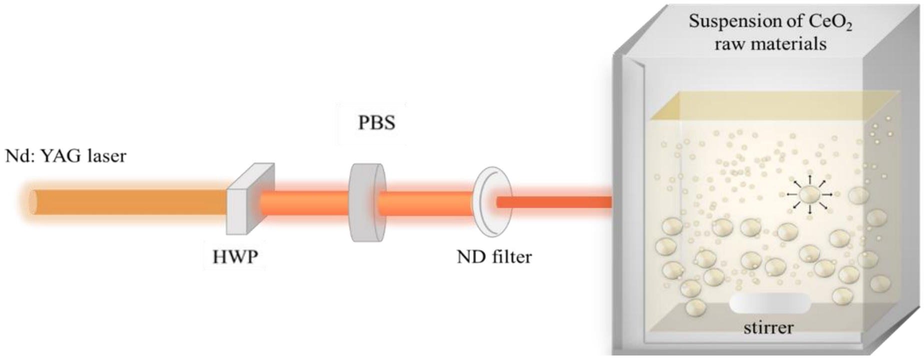

Figure 2-5. schematic of LAL process (powder target)

2.2 Experimental Procedure of LAL Method for Bulk Material with Focused Light

Preparation of CeO_2 tablet:

The process of preparing the sintered bulk CeO_2 sample began with the use of a tablet machine (TOYO HYDRAULIC EQUIPMENT CO. S.E PRESS, ESE-077-00). Approximately 0.6 grams of mixed CeO_2 powders were prepared using an agate mortar (As One Co., 2-887-03). The mixed powders were then compressed into tablets under a pressure of 100 MPa, resulting in tablets with an approximate thickness of 0.3 mm after sintering shrinkage. Following the tablet preparation, the Muffle furnace was employed for the sintering process. The sintering process was divided into two stages (Figure. 2-2). In the first stage, the furnace was heated to 900°C at a rate of 5°C per minute and maintained at this temperature for 2 hours. In the second stage, the temperature was further increased from 900°C to 1250°C, again at a rate of 5°C per minute, and held at 1250°C for an additional 2 hours.

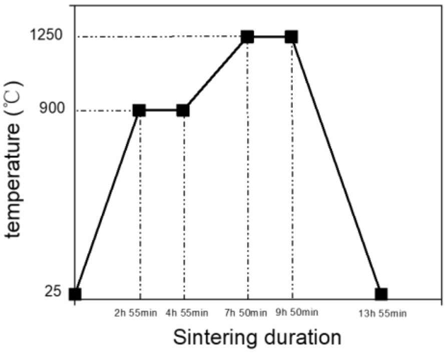

Figure 2-6. Sintering process

Laser Ablation Setup for Bulk Material:

For the laser ablation experiment, the sintered CeO_2 sample was placed at the center of the bottom of a glass bottle and covered with 5 mL of pure water (Figure 2-3). The same Nd: YAG laser, as described previously, was employed, maintaining a frequency of 10 Hz, a wavelength of 532 nm, and a pulse width of 13 ns. The laser beam was split using the polarized beam splitter (PBS) and adjusted with the half-wave plate (HWP). The laser beam was then refracted 90° through a plane mirror and focused onto the bulk target using a condenser.

Ablation Process:

The focused laser beam, with a fluence of 2 J/cm^2, irradiated the bulk CeO_2 target for 30 mins. This focused ablation process was designed to produce CeO_2 nanoparticles from the bulk material.

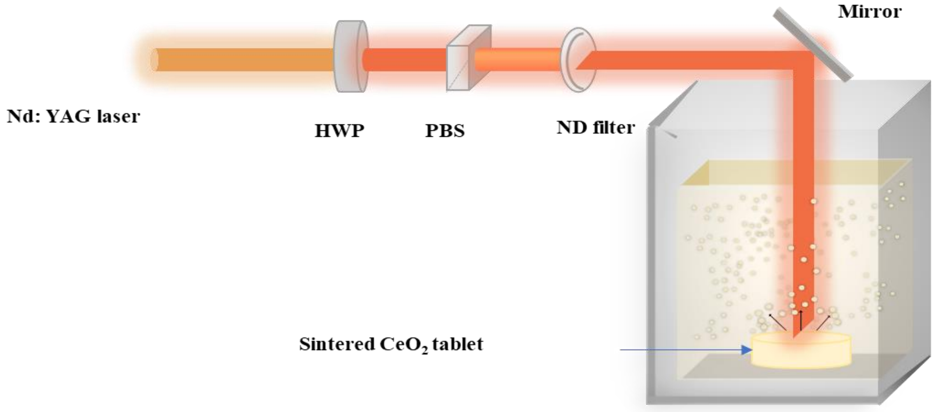

Figure 2-7. Schematic of LAL process (bulk target)

2.3 Characterization

After the preparation of the CeO_2 nanoparticles, several analysis methods were used to characterize their properties. These methods include X-ray powder diffraction (XRD), scanning electron microscopy (SEM), dynamic light scattering (DLS), ultraviolet-visible spectroscopy (UV-vis), energy-dispersive X-ray spectroscopy (EDS), and cyclic voltammetry (CV).

2.3.1 X-ray Powder Diffraction (XRD)

Both the raw materials and CeO_2 nanoparticles were identified using an X-ray diffractometer (XRD, Philips PANalytical, X'Pert-Pro-MRD), as shown in Figure 2.5, with support from the Tokyo Tech OFC Analysis Department. The wavelength of X-rays is close to the distance between the atomic planes inside the crystal, allowing the crystal to act as a spatial diffraction grating for X-rays. When a beam of X-rays is irradiated on an object, it is scattered by the atoms in the object, producing scattered waves. These waves interfere with each other, resulting in diffraction. By analyzing the diffraction results with Bragg's law [84]:

$$2d\sin\theta = n\lambda \tag{2-1}$$

Where n is an integer, λ is the wavelength of the incident wave, d is the plane spacing in the atomic lattice, and θ is the angle between the incident wave and the scattering plane. The crystal structure of the nanoparticles can thus be determined.

2.3.2 Scanning Electron Microscopy (SEM)

After dropping the suspension onto a round copper plate coated with a carbon support film (diameter = 2 mm, Oken Shoji Elastic Carbon ELS-C10 STEM Cu100P grid specification) and drying for 30 minutes, the scanning electron microscope (SEM, Hitachi High-Tech. Co. S-4800) was used to examine the primary particle size and morphology of the remaining nanoparticles. SEM generates an image of the sample surface by scanning it with a focused electron beam. Electrons interact with atoms in the sample, generating various signals containing information about the surface topography and composition [85]. The experimental conditions were set with an acceleration voltage of 5 kV, emission current of 10 A, focus mode of UHR, mixed secondary electron detector, and a working distance of 8 mm.

2.3.3 Dynamic Light Scattering (DLS)

The secondary particle size was measured by dynamic light scattering (DLS, Sysmex Co. Zetasizer Nano) by transferring the solution-containing nanoparticles into a plastic tube (1 mL). The light source of DLS is a He-Ne laser, and the Zetasizer software (version 7.1) was used to analyze the DLS data. Time fluctuations in the signal intensity, determined by the Brownian motion of particles in suspension [86], were analyzed. When light hits particles much smaller than its wavelength, Rayleigh scattering occurs, causing the intensity of scattered light to fluctuate over time due to the Brownian motion of particles. This fluctuation carries information about the movement of particles over time.

2.3.4 Ultraviolet-Visible Spectroscopy (UV-vis)

A spectrophotometer (UV-vis, Jasco. Co. V-670) was employed to analyze the UV absorption of the nanoparticle. This method involves irradiating samples with a continuous spectrum of electromagnetic waves in the ultraviolet-visible region and studying the relative intensity of light absorption by material molecules. Qualitative and quantitative analyses can be carried out through molecular ultraviolet-visible molecular absorption spectroscopy and according to Beer-Lambert law, respectively. Samples were held in a quartz cell, with pure water used to measure the baseline. The measurement range was set from 200 nm to 800 nm, and the Spectrum Manager software was applied to process the absorption spectrum.

2.3.5 Energy-Dispersive X-ray Spectroscopy (EDS)

Energy-dispersive X-ray spectroscopy (EDS, 200kV, JEM-2010F, Co. JEOL) was used to analyze the elemental composition of the CeO_2 nanoparticles. The SEM system equipped with an EDS detector was employed to perform this analysis. By detecting the characteristic X-rays emitted from the sample during electron beam interaction, the elemental composition and distribution within the sample were determined. This technique provides qualitative and quantitative information on the elements present in the nanoparticles.

2.3.6 Cyclic Voltammetry (CV)

Cyclic voltammetry (CV, RRDE-3A Rotating Ring Disk Electrode Apparatus Ver.3.0, Co. BAS) was used to evaluate the electrochemical properties of the CeO_2 nanoparticles, especially when used to modify the glassy carbon electrode (GCE) with reduced graphene oxide (rGO). A standard three-electrode setup was used, with a platinum wire as the counter electrode, Ag/AgCl as the reference electrode, and the modified GCE as the working electrode. The electrolyte solution typically consisted of an aqueous solution of 0.1 M KCl. The potential was cycled at a specific scan rate, and the resulting current was measured to provide information on the redox behavior and electrochemical performance of the nanoparticles.

References

[84] H. Stanjek, W. Häusler. *Hyperfine Interact.*, 154, 1 (2004) 107.

[85] J. Goldstein, D. Newbury, et al. *Scanning Electron Microscopy and X-ray Microanalysis. Third Edition. Academic/Plenum Publishers*, (2003) ISBN 0-306-47292-9.

[86] B.J. Berne, R. Pecora. *Dynamic Light Scattering. Courier Dover Publications* (2000) ISBN 0-486-41155-9.

Chapter 3

Effect of Laser Fluence on CeO_2 Morphology and Optical Properties

3.1 Introduction

The synthesis of CeO_2 nanoparticles using the Laser Ablation in Liquid (LAL) method is significantly influenced by various parameters such as irradiation time, fluence, and suspension concentration. Among these, laser fluence plays a crucial role in determining the morphology and optical properties of the resulting nanoparticles. This chapter explores the impact of laser fluence on CeO_2 nanoparticles, particularly focusing on their UV absorption capabilities. Understanding these effects is essential for optimizing the synthesis process to enhance the performance of CeO_2 in practical applications

3.1.1 Categories of Ultraviolet Radiation

Ultraviolet (UV) irradiation is an electromagnetic wave with a wavelength range between 10 nm to 400 nm, shorter than visible light but longer than X-rays [87]. UV radiation, despite its beneficial role in providing essential vitamin D through natural sunlight [88], is also recognized as a human carcinogen due to its potential to cause significant harm [89]. The damage caused by UV radiation to human skin includes erythema (redness), tanning, and local or systemic immunosuppression, which manifest as sunburn symptoms [90]. Prolonged exposure to UV radiation can lead to more severe health issues such as skin cancer, premature aging, and DNA damage [91].

The discovery of UV radiation dates back to 1801 when German physicist Johann Wilhelm Ritter observed that invisible rays just beyond the violet end of the visible spectrum darkened silver chloride-soaked paper more quickly than violet light [92]. By 1903, it was established that the most effective wavelengths for such reactions were around 250 nm. In 1960, the effects of UV radiation on DNA were confirmed [91], highlighting the potential risks associated with UV exposure. This historical context underscores the dual nature of UV radiation—its essential biological roles and the potential for harm.

UV radiation is typically categorized into three main types based on wavelength [93]: UVC (100 - 280 nm), UVB (280 - 320 nm), and UVA (320 - 400 nm). UVA can be further divided into two subcategories: long UVA-1 (340 - 400 nm) and short UVA-2 (320 - 340 nm). These categories are essential for understanding the different effects and applicati8ons of UV radiation. UVC is the most dangerous but is mostly absorbed by the Earth's ozone layer, UVB is partially absorbed by the atmosphere and can cause direct DNA damage, while UVA, which is not absorbed by the ozone layer, penetrates deeper into the skin, causing indirect DNA damage and contributing to aging and skin cancer. Additionally, the International Organization for Standardization (ISO) provides a detailed subdivision of UV radiation, as shown in Table 3-1. This classification is crucial for optimizing the synthesis and application of CeO_2 nanoparticles, particularly in enhancing their UV absorption properties to develop effective UV protection materials.

Name	Photon energy (eV)	Wavelength (nm)	Notes
UVA	3.10–3.94	315–400	Long-wave UV, black light, not absorbed by the ozone layer: soft UV.
UVB	3.94–4.43	280–315	Medium-wave UV, mostly absorbed by the ozone layer
UVC	4.43–12.4	100–280	Short-wave UV, completely absorbed by the ozone layer and atmosphere
N-UV	3.10–4.13	300–400	Visible to birds, insects, and fish.
M-UV	4.13–6.20	200–300	Middle ultraviolet
F-UV	6.20–10.16	122–200	Ionizing radiation at shorter wavelengths
H Lyman-α	10.16–10.25	121–122	Spectral line at 121.6 nm, 10.20 eV.
E-UV	10.25–124	10–121	Entirely ionizing radiation by some definitions; completely absorbed by the atmosphere.
V-UV	6.20–124	10–200	Strongly absorbed by atmospheric oxygen, can propagate through nitrogen.

Table3-1. Different types of ultraviolet [94]

3.1.2 Damage of Ultraviolet Rays in Different Types

The energy of UV radiation is much higher than that of common molecular bonds in the human body, such as O-H, C-C, and C-H bonds, as shown in Table 3-2. These molecular bonds are crucial for the normal functionality of human bodies. Consequently, UV radiation can easily cause the scission of these molecular chains in organic cells, leading to severe damage, including irreversible DNA damage. In the worst cases, this can lead to cancer.

UV	C-C	C-H	O-H	Si-O
301 ~ 598 kJ / mol	347 kJ /mol	413 kJ / mol	462 kJ /mol	452 kJ / mol

Table3- 2. Energy of molecular chain [95]

UVC, with its extremely short wavelength, possesses very high energy that can kill organic cells almost instantly upon contact. This property makes UVC effective for use in disinfection lamps [96]. However, humans cannot withstand long-term exposure to UVC radiation from sunlight. Fortunately, UVC is mostly obstructed by the Earth's atmosphere and ozone layer, preventing it from causing harm to humans. On the other hand, UVB radiation is partially absorbed by the ozone layer, allowing some of it to reach the epidermal layer of the skin. UVB can cause skin tanning, burns, and erythema [96,97,98]. In the case of UVA, which looks less threatening than UVC and UVB due to its lower energy, showing a significant hazard. Although it is not as energetic as the others, it can easily penetrate the dermis of human skin due to its longer wavelength (Figure 3-1), leading to wrinkles and skin aging. Long-term exposure to UVA, particularly UVA-1 with wavelengths between 340 nm and 400 nm, can cut molecular bonds in DNA (Figure 3-2), causing irreversible damage and potentially leading to skin cancer [99]. This deep penetration and subtle damage make UVA particularly insidious, as the harmful effects may not be immediately noticeable but accumulate over time.

Figure 3- 1. UVA damages to human skin

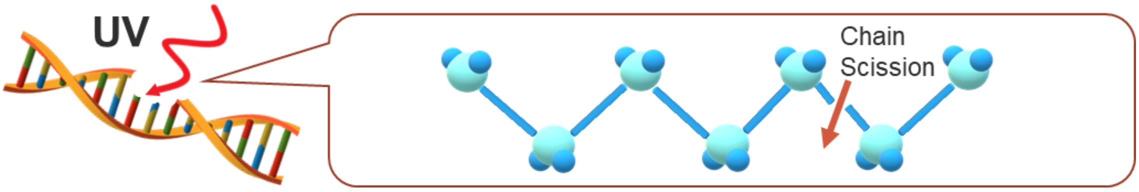

Figure 3- 2. DNA damage

3.1.3 Anti-Ultraviolet Materials

Given the harmful effects of UVB and UVA on human health, it is crucial to develop effective materials for UV protection. Sunburn caused by UVB radiation is typically noticeable due to skin color changes, itching, and peeling, prompting people to take protective measures. Titanium dioxide (TiO_2)-based sunscreens and parasols with TiO_2 coatings have been widely produced and are effective in blocking UVB [100].

However, the damage caused by UVA is less apparent and occurs over a longer period. Because the energy of UVA is relatively weak, it does not cause immediate harm, leading to a false sense of security. UVA can penetrate deep into the skin, causing long-term damage such as skin lesions and cancer. People often neglect UVA protection, particularly on cloudy days when UVA is still present in the solar spectrum. This oversight can lead to serious health consequences over time.

Over the past few years, CeO_2 has attracted significant attention as an anti-ultraviolet material. Recently, the UV absorption properties of CeO_2 have garnered interest due to their potential to protect against UVA radiation. CeO_2 offers several advantages, it has excellent UV absorption properties and less degradation over time [101], making it less harmful to human skin when used in cosmetic products [102]. Additionally, CeO_2 has a lower refractive index ($nCeO_2 = 2.2$) than TiO_2 ($nTiO_2 = 2.5$), which results in less reflection and a more natural appearance when used in cosmetics, avoiding the exaggerated paleness often associated with excessive TiO_2.

3.1.4 Principles of UV Absorption

The principle of UV absorption by CeO_2 nanoparticles is based on the excitation and de-excitation of electrons, resulting in the production of a spectrum, as illustrated in Figure 3-3.

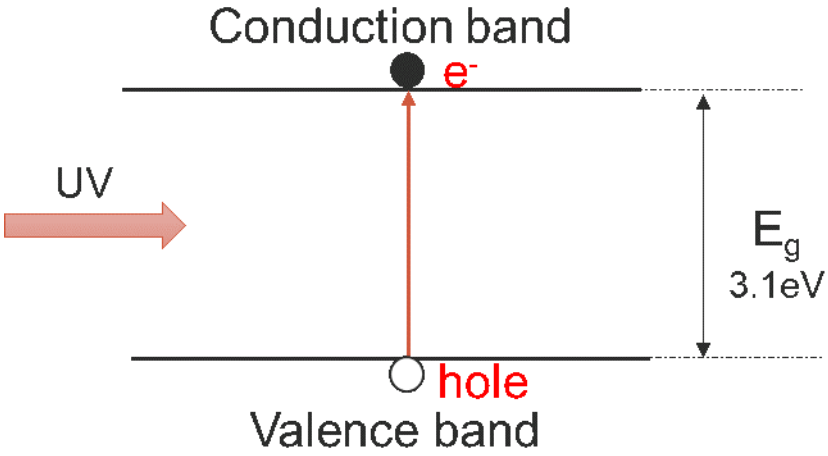

Figure 3-3. Schematic of UV absorption

When matter absorbs ultraviolet radiation, the electrons in it undergo excitation [103]. This causes them to jump from a ground state (an energy state with relatively low energy) to an excited state (an energy state with relatively high energy). In other words, the electron in the valence band may excite to the conduction band, leaving a hole behind. During this process, CeO_2 absorbs the UV radiation. The difference in energies between the ground state and the excited state of the electron is equal to the amount of ultraviolet or visible radiation absorbed.

The Beer-Lambert law, which describes the absorption of light, can be stated as follows [104]:

$$A = log_{10}\frac{I_t}{I_0} = log_{10}\frac{1}{T} = K \cdot l \ \cdot c \qquad (3\text{-}1)$$

Where A represents the absorbance; I_0 is the intensity of incident light; I_t is the intensity of the transmitted light; T is the transmittance; K is a coefficient, which can be absorption coefficient or molar absorption coefficient; l is the thickness of the absorbing medium, c is the concentration of the absorbing substance. When a beam of monochromatic light is made incident on a solution that contains a substance that absorbs the monochromatic light, the rate at which the intensity of the beam decreases along the thickness of the solution is directly proportional to the concentration of the absorbing substance in the solution and is also directly proportional to the intensity of the incident monochromatic radiation. As per the Beer-Lambert law, the greater the number of absorbing molecules (that have the ability to absorb light of a specific wavelength), the greater the extent of absorption of the radiation.

3.2 Experiment

3.2.1 Controlling of Experimental Conditions

In this research, the aim was to study the effects of various factors on the preparation of CeO_2 nanoparticles and to determine the optimal experimental conditions. 3 primary variables were chosen: the concentration of the suspension liquid, the irradiation duration, and the irradiation fluence. Each of these variables was systematically varied to understand their individual and combined impacts on the properties of the CeO_2 nanoparticles.

To investigate the dependency on concentration, different amounts of raw CeO_2 material were used to prepare suspension liquids with increasing concentrations of 200 μg/mL, 300 μg/mL, 400 μg/mL, and 500 μg/mL. This range was selected to observe how varying particle density in the suspension influences the nanoparticle formation and characteristics. For the time dependency study, the irradiation duration was controlled at intervals of 0.5 hours, 1 hour, and 1.5 hours. This range of times was chosen to evaluate the effect of exposure duration on the synthesis process, including how longer or shorter irradiation periods impact the size, morphology, and optical properties of the nanoparticles. Finally, to examine the fluence dependency, the fluence of the laser beam was set at three different levels: 300 mJ/cm^2, 150 mJ/cm^2, and 75 mJ/cm^2. By varying the energy delivered per unit area, this part of the study aimed to elucidate how different fluence levels affect the ablation efficiency, particle size distribution, and overall quality of the CeO_2 nanoparticles.

3.2.2 Experimental Process

Firstly, CeO_2 suspension liquids were prepared at specific concentrations ranging from 200 to 500 μg/mL by adding micro-sized CeO_2 powder (Kanto Chemical Co., INC. 99.99%) to pure water and stirring continuously in a 200 mL transparent, square-shaped glass bottle. CeO_2 nanoparticles were synthesized using the laser ablation in liquid approach, employing an Nd: YAG laser (Spectron Laser Systems Ltd., SL8585G) as previously mentioned (chapter 2.1). Neutral-density (ND) filters with 25% and 50% transmittance were used to achieve lower fluences of 150 mJ/cm^2 and 75 mJ/cm^2, respectively. The suspensions were irradiated for durations of 0.5 hours, 1 hour, and 1.5 hours to study time dependency. Under these conditions, CeO_2 nanoparticles with a comprehensive dataset were synthesized.

3.2.3 Analysis

After the CeO_2 nanoparticles' preparation, several analysis approaches were employed to characterize the nanoparticles' properties. Both the raw materials and CeO_2 nanoparticles were identified by employing an X-ray diffractometer. After dropping the suspension on a round copper plate (diameter = 2 mm) and drying for 30 min, a scanning electron microscope was employed to analyze the remaining nanoparticles' morphology and the primary particle size on copper plates, and morphological analysis was conducted. The second particle size and the aggregation phenomenon were examined using the dynamic light scattering. Additionally, UV absorption properties were analyzed from the UV-vis spectrum.

3.3 Results and Discussion

3.3.1 Phase Analysis

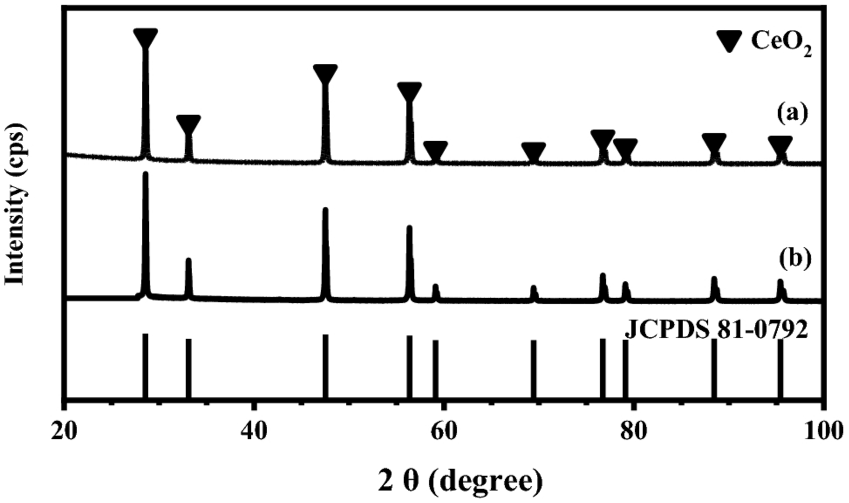

Figure 3-4. XRD patterns of nano-sized CeO_2 particles (a) and raw materials (b)

The phase and structural transitions of CeO_2 before and after laser ablation were analyzed using X-ray diffraction (XRD) patterns, as shown in Figure 3-4. The curve in Figure 3-4 (a) represents CeO_2 nanoparticles prepared under typical conditions: an irradiation duration of 1 hour, a suspension concentration of 400 µg/mL, and a laser fluence of 300 mJ/cm². In contrast, Figure 3-4 (b) depicts the XRD curve of the large-sized raw material. Referring to the standard XRD spectrum for CeO_2 with a lattice parameter of $a=b=c=3.86$ Å (JCPDS 81-0792), no impurity peaks were detected in either sample. The diffraction peaks appeared at 2θ angles of 28.54°, 33.09°, 47.5°, 56.28°, 59.08°, 69.41°, 76.71°, 79.08°, and 88.41°, corresponding to the Miller indices (111), (200), (220), (311), (222), (400), (331), (420), and (422) planes of CeO_2, respectively.

This confirms that the CeO_2 nanoparticles retained their cubic fluorite structure both before and after the laser ablation process. Furthermore, there were no phase transitions or formation of impurities observed following the reduction in particle size using the LAL method.

3.3.2 Morphology of CeO_2 NPs Effected on Fluence

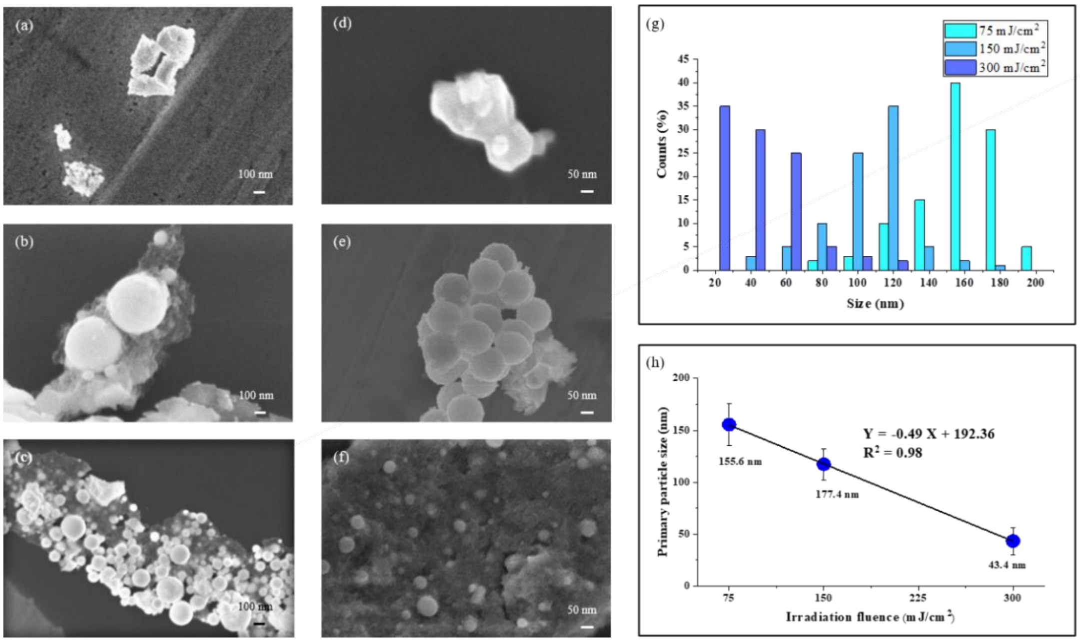

Figure 3-5. SEM morphology graphics of CeO_2 suspension liquid ablated for 1 h, with a concentration of 400 mJ/cm², with irradiation fluence of (a, d) 75 mJ/cm², (b, e) 150 mJ/cm², and (c, f) 300 mJ/cm². (a–c) High magnification, (d–f) low magnification, (g) histogram of particle size, and (h) average size of nanoparticles as a function of laser fluence with a linear fitting.

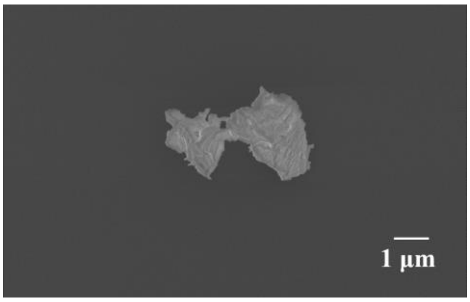

Figure 3-7. CeO_2 raw material

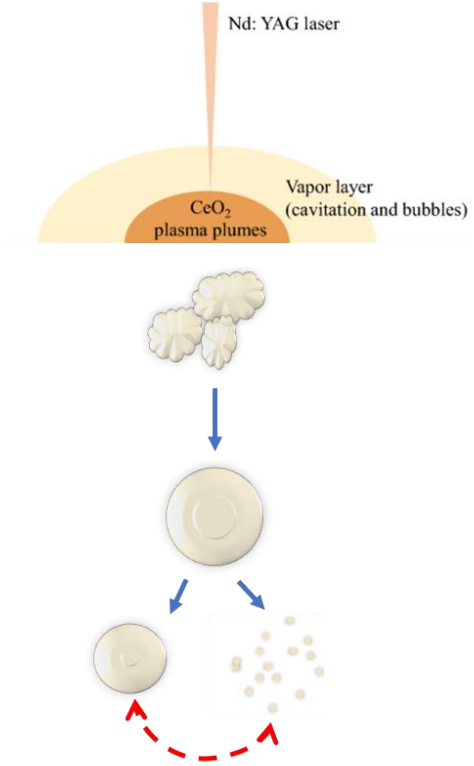

Figure 3-6. Schematic of NPs formation

The morphology of CeO_2 nanoparticles synthesized under varying laser fluence was examined using Scanning Electron Microscopy (SEM). The SEM images (Figure 3-5) reveal that the average primary nanoparticle size decreased from 150 nm to approximately 50 nm as the energy intensity increased. This decrease in primary particle size with increasing energy fluence is quantitatively supported by the high R-squared value in the linear fitting of size versus fluence (Figure 3-5, h).

As the fluence increased, more spherical nanoparticles appeared. This phenomenon can be explained by the laser melting in liquid technique (Figure 3-6). Initially, irregularly shaped raw particles distributed in the liquid are selectively heated by the laser. Rapid heating generates thermally induced nanobubbles at the surface of the irradiation targets, which serve as a thermal barrier and enhance the heating process. With a spinodal temperature below the melting point, the photothermal impact produces spherical shapes under this barrier. Smaller CeO_2 nanoparticles, formed preferentially through laser melting [83] and fragmentation processes, are seen to melt into larger spherical particles at 150 mJ/cm^2 (Figure 3-5, b, e). At higher energy densities (Figure 3-5, c, f), the temperature of the suspension rises significantly, leading to a sudden increase in the concentration of the suspension. This higher energy laser ablation causes the raw materials to fragment into dispersed nanoparticles. The increased concentration of particles in the liquid accelerates the fragmentation of smaller particles, resulting in greater energy scattering. Larger spherical particles (100–200 nm) that obstruct the laser path are fragmented into smaller particles, and repeated laser melting generates smaller spherical particles. Under an energy density of 300 mJ/cm², a significant number of nanoparticles with diameters ranging from 5 to 50 nm were produced, as shown in the size distribution (Figure 3-5, g).

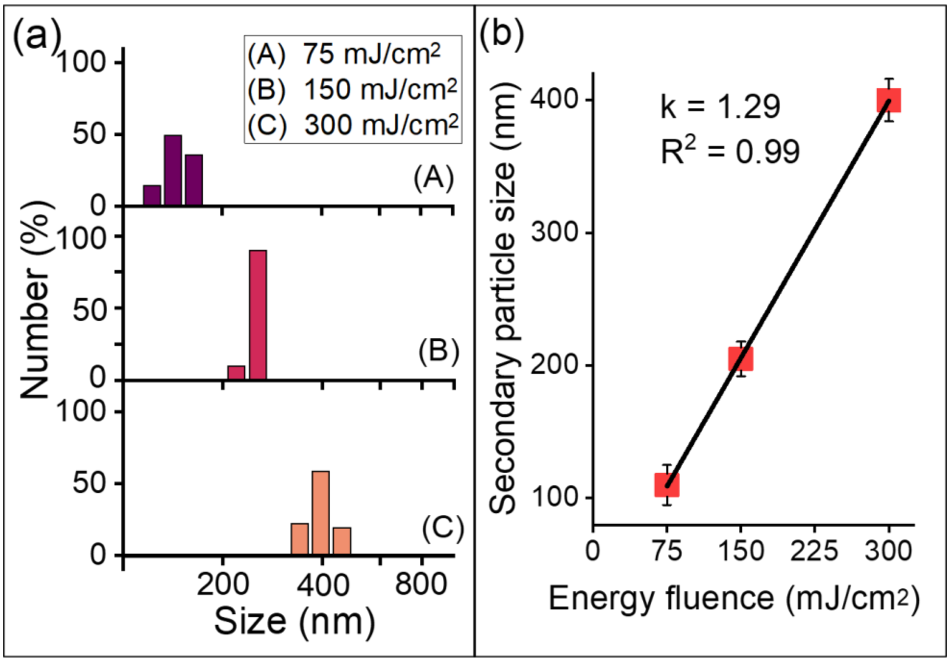

Figure 3-8. (a) DLS histograms of CeO_2 suspension liquid ablated for 1 h, with a concentration of 400 mJ/cm², the secondary particle size of CeO_2 nanoparticles with irradiation fluence at (A) 75, (B) 150, and (C) 300 mJ/cm² and (b) the secondary particle size as a function of energy fluence with the linear fitting

The DLS patterns and size distributions (Figure 3) indicate that the average secondary particle size increased from 105 to 410 nm as the fluence increased from 75 to 300 mJ/cm². This size increase demonstrates an improved aggregation phenomenon of the CeO_2 nanoparticles, resulting in more homogeneous, less aggregated, and more delicate samples at higher fluences. The sharp and exclusive distribution peaks for each condition highlight the uniformity of the secondary particle size distribution.

3.3.3 Discussion of Aggregation Phenomenon with Irradiation Time and Suspension Concentration Affection

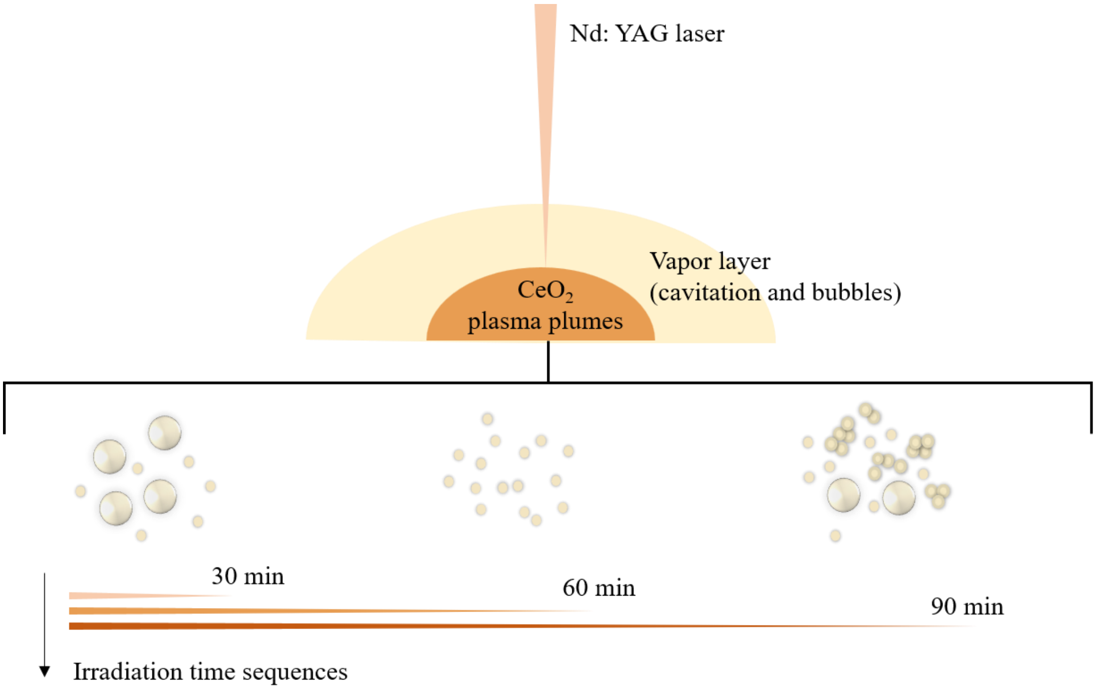

Figure 3-9. .Schematics of the spherical nanoparticles formed using the laser ablation in liquid approach with the impact on the irradiation time

The primary particle size tends to be much smaller at higher fluences, while the larger and more uniformly sized secondary particles represent the aggregation phenomenon between the smaller nanoparticles. This aggregation can be attributed to several factors. Unstable nanoscale particles, due to the accumulation of surface electric charges, tend to aggregate when the van der Waals forces between nanoparticles outweigh their gravitational forces [105]. Additionally, if the nanoparticle surfaces are not perfectly smooth, local nonuniformities in electric potential can result in the accumulation of local electric charges [106,107,108]. Nanoparticles also exhibit a significantly greater specific surface area compared to their macroscale counterparts, leading to the formation of agglomerates that minimize surface energy, thereby maintaining stability. The laser ablation process produces nanoparticles with numerous dangling hydrogen and chemical bonds on their surfaces, resulting in high surface energy. It becomes energetically favorable for these nanoparticles to form larger, stable particles through aggregation. This phenomenon becomes particularly noticeable over time, as illustrated in Figure 3-11. The energy from the laser beam irradiates the target surface and is confined to the plasma plume to generate nanoparticles. With prolonged irradiation duration, cerium oxide nanoparticles gradually agglomerate due to higher concentration (Figure 3-10), forming secondary particles. The schematic in Figure 3-9 demonstrates the impact of irradiation time on nanoparticle formation. Initially, smaller nanoparticles are produced, but as irradiation continues, these particles begin to aggregate, forming larger secondary particles.

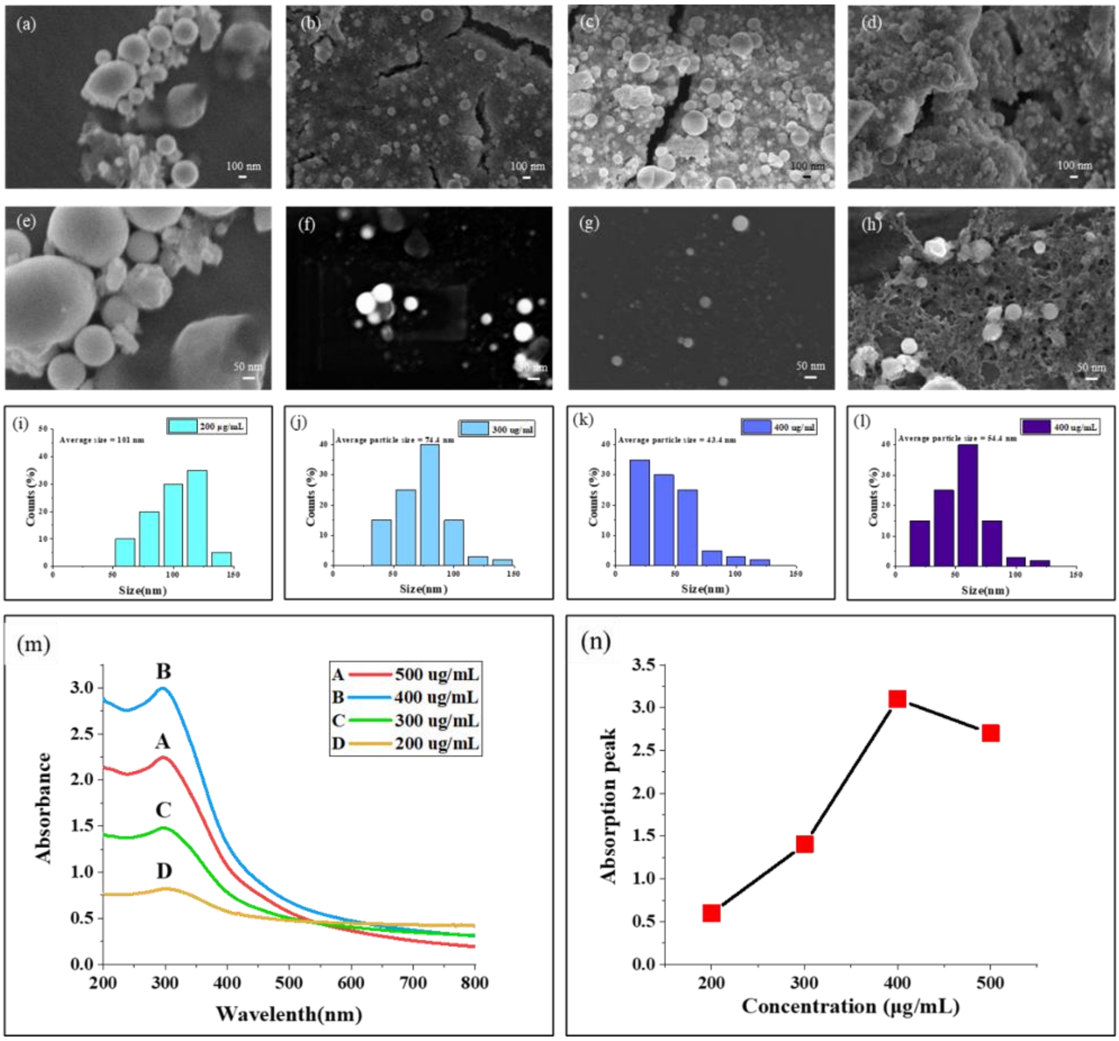

Figure 3-10. Morphology effect on concentration. (a-h) SEM morphology graphics of CeO_2 suspension liquid irradiated for 1 h, irradiation fluence at 300 mJ/cm^2, with concentration of 200, 300, 400, 500 μg/mL. (a-c) SEM observed at low magnification, and (d-f) SEM observed at high magnification. (m) UV-vis spectrum of each concentration. (n) The peak intensity of absorption peaks in the picture (a).

The SEM images in Figure 3-10 (a-h) provide further insights into the aggregation phenomenon as a function of suspension concentration. At lower concentrations (200 μg/mL and 300 μg/mL), the nanoparticles were well-dispersed with minimal clustering and large primary particle sizes. As the concentration increases to 400 μg/mL, the primary particle size decreases, and aggregation becomes apparent. When the concentration reaches 500 μg/mL, significant aggregation occurs, and the particle size increases again due to the formation of larger clusters. This trend is corroborated by the UV-vis spectroscopy results shown in Figure 3-10 (m). At concentrations up to 400 μg/mL, the absorption increased, indicating a higher number of small-sized particles capable of absorbing UV radiation. However, beyond this concentration, the absorption decreases, suggesting a reduction in the number of small particles as aggregation predominates.

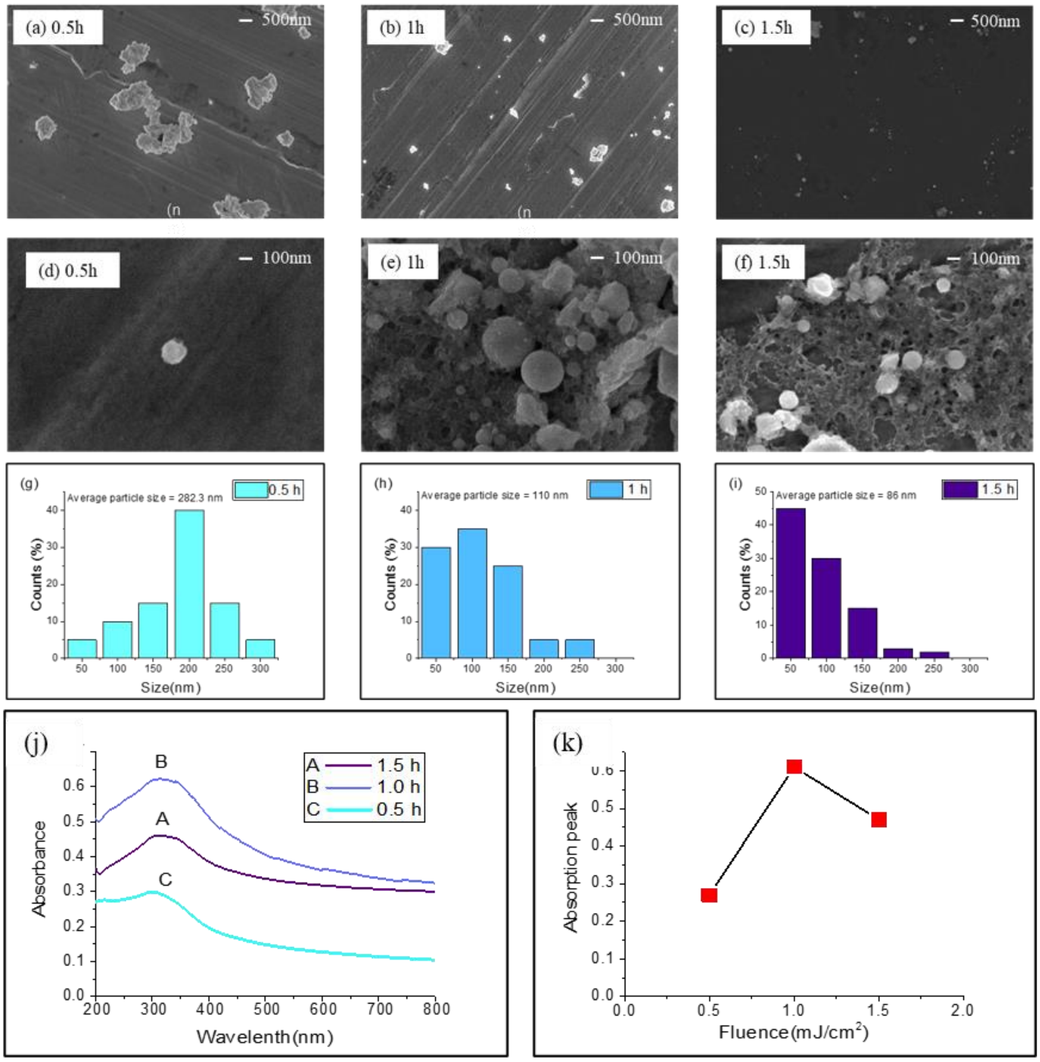

Figure 3-11. Morphology effect on time. (a-h) SEM morphology graphics of CeO_2 suspension liquid at concentration of 200ug/mL, irradiation fluence of 300 mJ/cm^2, with irradiation duration of 0.5 h, 1 h, 1.5 h. (a-c) SEM observed at low magnification, and (d-f) SEM observed at high magnification. (m) UV-vis spectrum of each concentration. (n) The peak intensity of absorption peaks in the picture (a)

Similarly, the study on the effect of the irradiation time (figure 3-11) further demonstrates the influence of the aggregation of CeO_2 nanoparticles. At the initial stage (0.5 hours), some small-sized nanoparticles were observed, however, larger particles still remained, and the UV-vis absorption showed low absorption due to fewer small particles (Figure 3-11, j). As the irradiation time increased to 1 hour, the average particle size decreased, resulting in higher UV absorbance, indicating a greater number of small particles capable of UV absorption (Figure 3-11, k). However, with further prolonged irradiation (1.5 hours), aggregation became more prominent, leading to larger particle sizes again, and a decrease in UV absorbance was observed.

3.3.4 UV Absorption Properties of Synthesized CeO_2 Nanoparticles

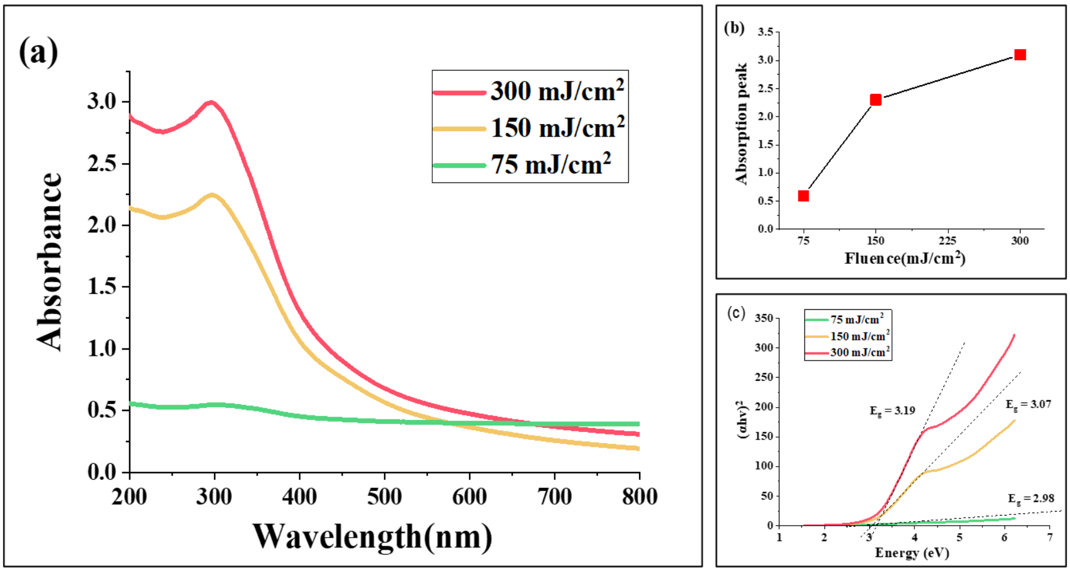

Figure 3-12. (a) UV–Vis spectrum of CeO_2 suspension liquid irradiated for 1 h, with a concentration of 400 mJ/cm^2 and irradiation fluence of 75, 150, and 300 mJ/cm^2, (b) absorption peak intensity, (c) plots of $(\alpha h\upsilon)^2$ vs. eυ for the direct transitions of CeO_2 nanoparticles

The UV absorption properties of CeO_2 nanoparticles were characterized using the ultraviolet-visible (UV-Vis) spectrum, as shown in Figure 3-12, (a). The intensity of the absorbance peaks is detailed in Figure 5b. Due to the electronic transition between O^{2-} (2p) and Ce^{4+} (4f) bands, the CeO_2 nanoparticle suspension demonstrated strong UV absorption between 250 and 400 nm. This range covers the UVA waveband, highlighting the material's excellent UVA-filtering ability.

As the irradiation fluence increased, the absorbance peak also improved significantly, from 0.8 to 3.1, indicating a rapid growth in absorbance with higher energy intensity. Additionally, the absorption band exhibited a slight blue shift as the energy fluence increased, which corresponds to a decrease in nanoparticle size. This shift was further supported by the increase in bandgap energy [109, 110], as estimated by the Tauc plot [111] (Figure 3-12, c). This phenomenon is attributed to the quantum size effect of semiconductors, where the electron energy levels near the Fermi level separate into discrete levels, leading to a wider energy gap as particle size decreases. This blue shift primarily occurs in nanoparticles smaller than 10 nm. The SEM images and DLS patterns (Figures 3-5 and 3-8) also corroborate this, showing smaller and more spherical nanoparticles formed at higher energy intensities, which directly enhances UV absorbance.

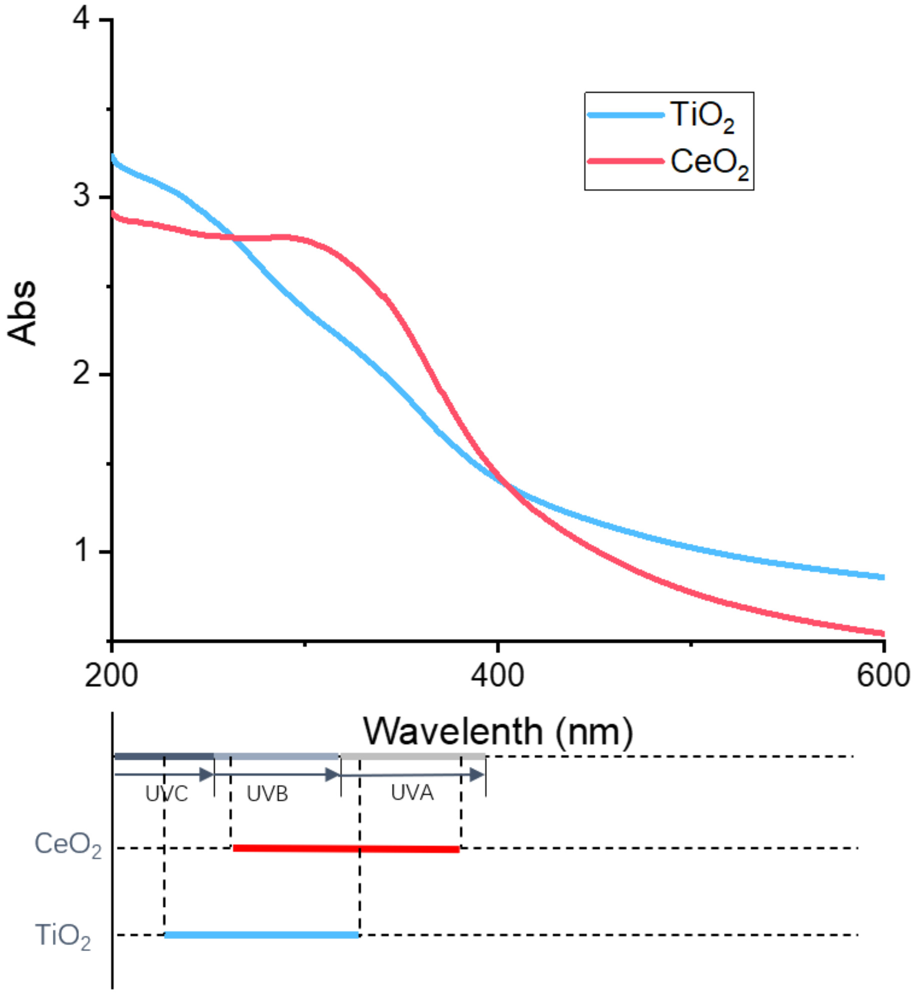

Figure 3-13. UV absorption range of CeO_2 with comparison of TiO_2

When comparing CeO_2 to TiO_2, it is evident that CeO_2 has a broader UV absorption range. CeO_2 absorbs UV light between 260 nm and 390 nm, while TiO_2 absorbs between 220 nm and 320 nm (Figure 3-13). Additionally, the absorption peak of CeO_2 is higher than that of TiO_2, indicating a more effective UV-blocking capability, especially in the UVA range. This broader absorption range and higher peak make CeO_2 a superior material for UV protection applications compared to TiO_2.

The enhanced UV absorption properties of CeO_2 nanoparticles, influenced by the laser fluence during synthesis, underscore their potential as effective UVA-filtering materials. The combination of a wider absorption range and higher absorbance peak positions CeO_2 as an excellent candidate for applications requiring robust UV protection.

3.4 Summary

In this chapter, the effects of laser fluence on the morphology and UV absorption properties of CeO_2 nanoparticles were systematically investigated. The research demonstrated that varying laser fluence significantly impacts the size, shape, and aggregation behavior of the nanoparticles. Higher fluences resulted in smaller primary particles with spherical shape and more uniform secondary particles, indicating reduced aggregation.

SEM and DLS analyses confirmed that both the concentration of the suspension and irradiation time critically affect the nanoparticle characteristics. Lower concentrations and shorter irradiation times produced larger, less aggregated particles, while higher concentrations and prolonged irradiation led to increased aggregation and larger secondary particles. This aggregation phenomenon was further evidenced by UV-Vis spectroscopy, which showed a decrease in UV absorption at higher concentrations due to fewer small particles capable of absorbing UV radiation.

The UV absorption properties of CeO_2 nanoparticles were enhanced with increasing laser fluence, displaying a broader and more intense absorption range compared to TiO_2, particularly in the UVA region. This superior UV absorption capability is attributed to the quantum size effect, where smaller particle sizes result in a wider bandgap and enhanced UV absorption.

Overall, this chapter elucidates the optimal conditions for synthesizing CeO_2 nanoparticles with desirable properties for UV protection and further biosensing applications, highlighting the importance of controlling laser fluence, suspension concentration, and irradiation time.

References

[87] T.V. Schumann. *Astrophys. J.*, 38 (1914) 1.
[88] M.F. Holick. *Am. J. Clin. Nutr.*, 79, 3 (2004).
[89] Y. Matsumura, H.N. Ananthaswamy. Toxicol. *Appl. Pharmacol.*, 195, 3 (2004).
[90] H. Torma, B. Berne. Acta Derm. *Venereol.*, 68, 4 (1988)
[91] J. Bolton, C. Colton. AWWA., ISBN 978-1-58321-584-5, (2008) 3.
[92] J.W. Draper. *The Practical Mechanic and Engineer's Magazine*, (1844) 122.
[93] U.P. Kappes, D. Luo, P. Marisa, S. Thomas, M. Rünger. *J. Investig. Dermatol.*, 126, 3 (2006).
[94] ISO 21348 *Process for Determining Solar Irradiances*.
[95] L. Truffault, et al. *Mater. Res. Bull.*, 45 (2010) 527.
[96] B.D. Wilson, S. Moon, F. Armstrong. *J. Clin. Aesthet. Dermatol.*, 5, 9 (2012).
[97] R.M. Lavker, G.F. Gerberick, D. Veres, et al. *J. Am. Acad. Dermatol.*, 32 (1995) 53.

[98] U.P. Kappes, D. Luo, M. P., K.S. Thomas, M. Rünger. J. *Investig. Dermatol*., 126, 3 (2006).

[99] A. Jaroenworaluck, W. Sunsaneeyametha, N. Kosachan, R. Stevens. *Surf. Interface Anal.*, 10 (2001) 937.

[100] M.J. Muñoz-Batista, M.M. Ballari, A. Kubacka, A.E. Cassano, O.M. Alfano. *Chem. Eng. J.*, 255 (2014) 297.

[101] S. Yabe, T. Sato. *J. Solid State Chem.*, 171 (2003) 1.

[102] M. Harb, D. Masih, S.O. Chikh, P. Sautet, J.M. Basset, K. Takanabe. *J. Phys. Chem. C,* 117, 34 (2013).

[103] J.T. Houghton. *The Physics of Atmospheres*. *2nd ed*. ISBN 0-521-33956-1, Chapter 2.

[104] V.V. Klimov, A. Lambrecht. *Plasmonics*, 4 (2009) 31.

[105] D. Zhang, B. Gökce, S. Barcikowski. *Chem. Rev*., 117 (2017) 3990.

[106] J.M. Goff, S.B. Sinnott, I. Dabo. *J. Chem. Phys*., 152 (2020) 064102.

[107] T.E. Itina. *J. Phys. Chem. C*, 115 (2011) 5044.

[108] S. Tsunekawa, T. Fukuda, A. Kasuya. *J. Appl. Phys*., 87 (2000) 1318.

[109] J. Miao, H. Wang, Y. Li, J. Zhu, J. Zhu. *J. Cryst. Growth*, 281 (2005) 525.

[110] J. Tauc. *Mater. Res. Bull.*, 3 (1968) 37.

Chapter 4

Effect of Focused Laser Ablation on NPs Production and the Morphology Comparison

4.1 Introduction

The synthesis of cerium oxide (CeO_2) nanoparticles (NPs) using laser ablation in liquid (LAL) has garnered significant attention due to its ability to produce high-purity nanoparticles with controlled properties [74, 75]. This chapter explores the enhancement of the LAL method, particularly by employing focused light, to improve the yield of CeO_2 NPs. Focusing the laser beam intensifies the energy density at the target site, promoting more efficient ablation and higher nanoparticle production rates [111]. The focused laser ablation process involves concentrating the laser beam onto a small area of the CeO_2 target immersed in a liquid medium [112], facilitating the rapid formation of NPs [113].

The principle of focused laser irradiation for nanoparticle synthesis involves three main stages [114]: absorption of energy, thermal expansion and evaporation, and cooling and condensation. When the focused laser beam irradiates the target material, the atoms absorb the laser energy, causing them to jump from their ground state to an excited state [115]. This absorbed energy leads to rapid thermal expansion and evaporation, as the excited atoms release energy and cause surface atoms to be ejected or peeled off. These ejected atoms and clusters then rapidly cool and condense in the surrounding liquid medium [116], forming nanoparticles. The rapid cooling stabilizes the nanoparticles in the desired size and shape, preventing further agglomeration or growth [115, 117]. By concentrating the laser energy into a small area, focused laser irradiation enhances the efficiency of these processes, ensuring a high yield and uniformity of the resulting nanoparticles.

In contrast to the laser ablation method, traditional chemical synthesis techniques, such as the precipitation method [118], are widely used for nanoparticle production. The precipitation method typically involves mixing chemical precursors in a solution, leading to the formation of nanoparticles through controlled nucleation and growth processes [119]. While chemical methods can produce large quantities of nanoparticles, they often suffer from issues related to purity, particle size distribution, and the need for extensive post-synthesis purification steps [120]. The controlled environment of laser ablation allows for precise manipulation of particle formation, reducing the occurrence of irregular shapes and sizes commonly seen in chemically synthesized nanoparticles.

To thoroughly compare the effectiveness of these two methods, advanced data science techniques will be employed to analyze the morphology of the synthesized nanoparticles. Specifically, Scanning Electron Microscopy (SEM) data will be processed using a series of computational steps to determine the size distribution of the nanoparticles for plenty of data. The process involves converting the SEM images to grayscale and applying a bilateral filter [121] to smooth the images while preserving the edges. Following this, Otsu's thresholding method [122] is used to segment the particles from the background, and the "Hough Circle Transform" is applied to detect and measure the spherical nanoparticles [123]. This automated analysis provides a robust and unbiased evaluation of the nanoparticle size distribution, crucial for comparing the yields and quality of nanoparticles produced by the focused laser ablation and chemical precipitation methods.

In summary, this chapter will delve into the optimized focused laser ablation process, its advantages over traditional chemical methods, and the critical role of spherical nanoparticles. The comparative analysis, supported by advanced SEM data processing, aims to highlight the superior yield and quality of nanoparticles achieved through the focused laser ablation method.

4.2 Experiment

4.2.1 Laser Ablation in Liquid Method

Micron-sized CeO_2 powder (Kanto Chemical Co., INC., 99.99%) was compacted into 0.3 mm tablets at 150 MPa. The tablets were then sintered at 1250 °C for 2 hours to create a CeO_2 irradiation target bulk. The target was placed at the center of the bottom of a glass bottle and covered with 20 mL of pure water. An Nd: YAG laser operating at a wavelength of 532 nm with a second harmonic generation frequency of 10 Hz was used for laser ablation. The laser settings were as follows: maximum output power of approximately 3.6 W, energy of 360 mJ/pulse, and pulse width of 13 ns. The laser beam was split by a polarizing beam splitter (PBS), adjusted by a half-wave plate (HWP), refracted 90° through a plane mirror, and collected by a condenser. The CeO_2 nanoparticle suspension liquid was prepared by subjecting the target to a 5 J/cm^2 laser beam for 30 minutes. The resulting nanoparticles were filtered to ensure uniformity and to calculate the concentration of the nanoparticles.

4.2.2 Precipitation Method

A precursor solution was prepared by dissolving 4.35 g of $Ce(NO_3)_3 \cdot 6H_2O$ (SIGMA-ALDRICH, Co., 99.99%) in 50 mL of deionized water. Then, 3 mL of ammonia was added drop by drop, and the mixture was stirred for 24 hours. The solution initially had a light brown color, which changed to light yellow after 10 hours, indicating the transition of Ce^{3+} to Ce^{4+}. After centrifugation (3000 rpm, 20 min), the precipitate was obtained. The precipitate was washed several times with DI water and ethanol, then dried overnight. The dried precipitate was sintered at 900 °C for 2 hours to remove impurities and obtain CeO_2 nanoparticles.

4.2.3 Analysis

In this chapter, the morphology of the synthesized CeO_2 nanoparticles was compared using Scanning Electron Microscopy (SEM), Dynamic Light Scattering (DLS), and Ultraviolet-Visible Spectroscopy (UV-Vis). Advanced data science techniques were employed to optimize the SEM analysis. Python was used to enhance image analysis, and this comprehensive approach allowed for accurate determination of nanoparticle size distribution and facilitated a detailed comparison between the laser ablation and precipitation methods.

4.3 Results and Discussion

4.3.1 Comparison of LAL Method vs. Precipitation Method

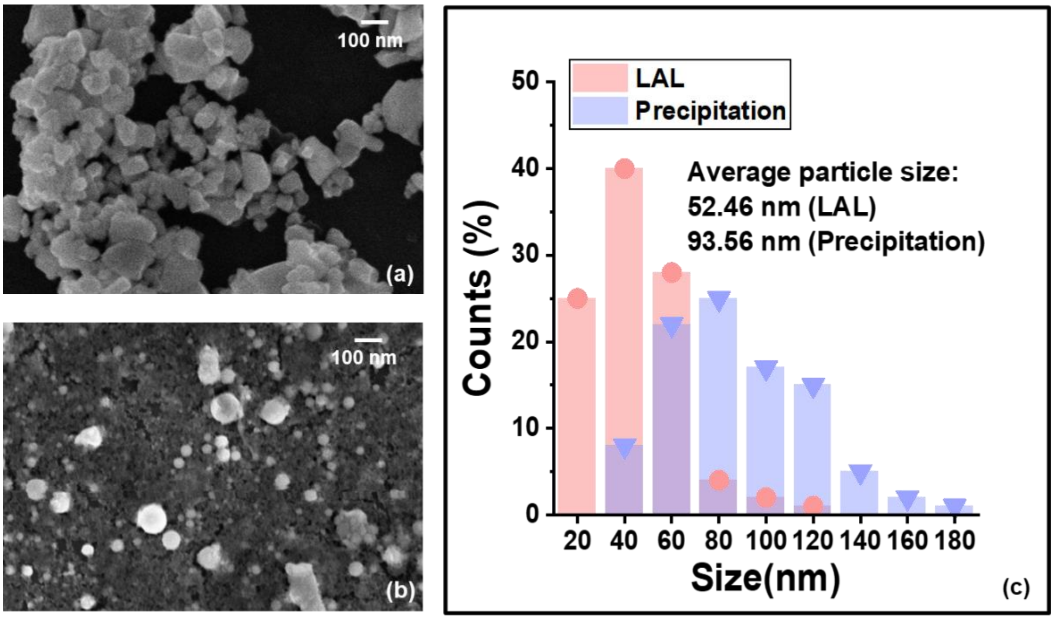

Figure 4-1. SEM images of (a) raw material and nanoparticles at each fluence ((b) 75 mJ/cm^2, (c) 150 mJ/cm^2 and (d) 300 mJ/cm^2

Figures 4-1 (a) and (b) illustrate the SEM images of CeO_2 nanoparticles synthesized by the precipitation and LAL methods, respectively. Figure 4-1(c) presents the primary size distribution obtained from the two methods. The average particle sizes in figure 4-1 (c) were calculated by the sphere diameter of the weighted average volume of spherical nanoparticles. SEM image of the precipitation method (Figure 1(a)) reveals CeO_2 nanoparticles with an average size of 93.56 nm, exhibiting an irregular, bulk, or polyhedral shape. Additionally, the precipitation method demonstrates a higher degree of size dispersity, with a wider range of particle sizes observed. In contrast, the SEM image of the LAL method (Figure 4-1(b)) displays CeO_2 nanoparticles with an average size of 52.46 nm, showing remarkable uniformity in size and spherical shape. The nanoparticles synthesized via the LAL method exhibit a narrow size distribution and a significantly reduced presence of larger aggregates. The formation of spherical CeO_2 nanoparticles in the LAL method can be attributed to the unique process involved. During laser ablation, a high-energy laser pulse is focused on the cerium oxide bulk target submerged in the liquid medium (DI water) [124]. The intense laser energy causes localized heating and vaporization of the target material, resulting in the generation of a high-temperature, high-pressure plasma plume [125]. As the plasma plume rapidly expands and cools upon contact with the surrounding liquid, the supersaturated vapor undergoes rapid nucleation and condensation. This rapid cooling and condensation process promotes the formation of individual spherical nanoparticles [126, 127].

The absence of external perturbations during the LAL method eliminates growth mechanisms that favor anisotropic particle growth [128], which is present in the precipitation method. This results in CeO_2 nanoparticles forming more easily into spherical shapes in pure water. Moreover, the quenching effect [129] induced by the rapid heat transfer from the plasma plume to the liquid medium prevents significant particle aggregation and helps preserve the spherical morphology. Thus, the LAL method produces more uniform, smaller, and spherical CeO_2 nanoparticles compared to the precipitation method, which yields larger, irregularly shaped particles with a broader size distribution.

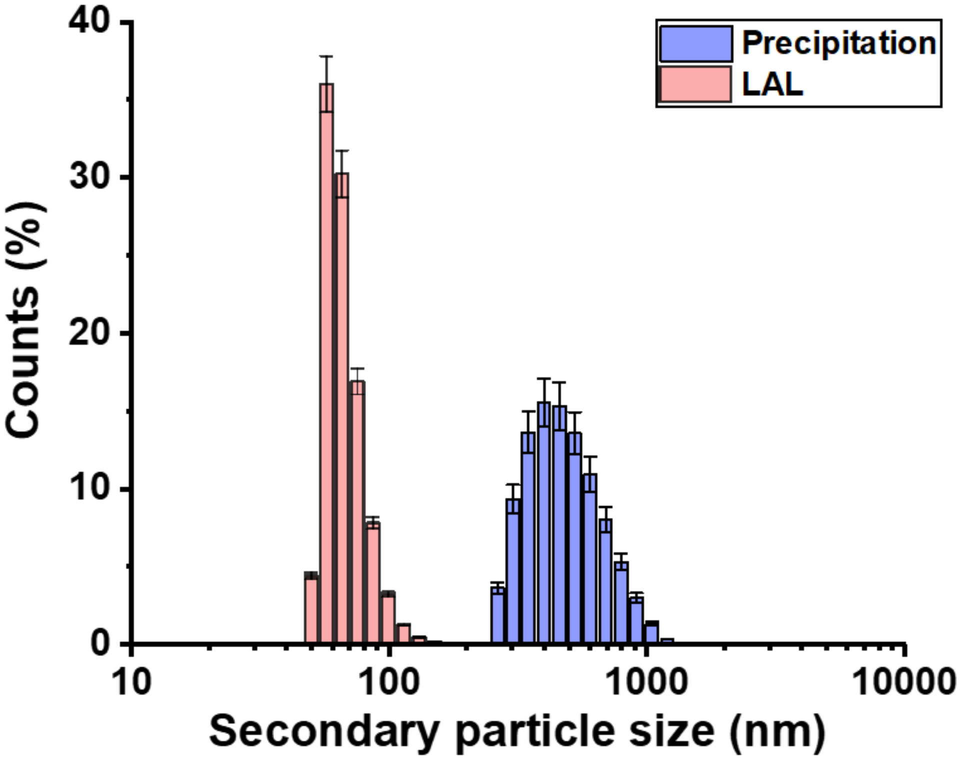

Figure 4-2. DLS comparison of secondary particle size distribution made by precipitation method and laser ablation in liquid method.

Method	Precipitation	LAL
d (nm)	497.98	44.67
σ (nm^2)	464.48	15.47
PDI $(d / σ)^2$	0.87	0.12

Table 4-1.Calculation of the PDI value based on the secondary particle size distribution in Figure 4-2

The comparison of the secondary particle size distributions of the CeO_2 suspension liquids synthesized through the precipitation and LAL methods is shown in the DLS distribution (Figure 4-2). The laser ablation in liquid method shows a narrow distribution peak ranging from approximately 20 to 110 nm. In contrast, the precipitation method exhibits a distribution peak spanning from 200 to 1000 nm, signifying significant aggregation.

To quantify the degree of size uniformity in the colloidal system, Table 4-1 presents the calculated PDI (polydispersity index) values for the secondary particle size distributions [130] depicted in Figure 4-2, with lower values indicating a more monodisperse system. The PDI was calculated using the following equation (4-1):

$$PDI = \left(\frac{d}{\sigma}\right)^2 \tag{4-1}$$

where d is the mean particle size and σ is the second moment (variance). The PDI value for the LAL method was calculated to be 0.12, whereas the precipitation method yielded a PDI of 0.87, signifying a polydisperse system with evident aggregation compared to the LAL method. These findings suggest that the LAL method yields CeO_2 particles with superior dispersion and reduced aggregation compared to the precipitation method. The spherical-shaped CeO_2 nanoparticles produced by the LAL method contribute to a reduction in aggregation. Spherical nanoparticles have a smaller surface area compared to irregular-shaped nanoparticles of the same volume, minimizing the opportunities for particles to come into close contact and adhere to one another. The smaller surface area can result in lower surface energy [131], making it less likely for spherical nanoparticles to aggregate. Additionally, the uniform surface charge distribution of spherical CeO_2 tends to be more stable in solution due to the repulsive forces between similarly charged particles, preventing aggregation and keeping the particles dispersed in the solution.

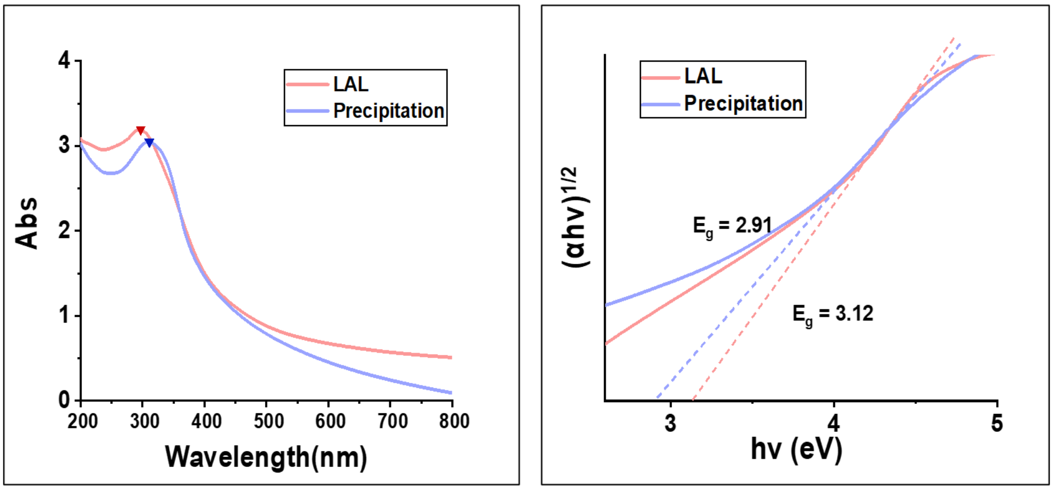

Figure 4-3. (a) UV-vis of LAL and precipitation method. (b) Tauc plot of (a).

Figure 4-3 (a) depicts the UV-Vis spectra obtained for CeO_2 nanoparticles synthesized through the LAL and precipitation methods. Both curves show strong UV absorption peaks approximately between 250 nm and 350 nm, which can be attributed to the electronic transitions between the oxygen 2p and cerium 4f bands in CeO_2. A noticeable blue shift is observed in the absorption peak of the LAL method compared to the precipitation method, indicating smaller nanoparticle sizes produced by the LAL method. To further investigate the optical properties and determine the band gaps, a Tauc plot is presented in Figure 4-3(b). This plot demonstrates a higher band gap for LAL-synthesized CeO_2 nanoparticles (3.12 eV) compared to the precipitation-synthesized sample (2.91 eV). According to the quantum size effect [132], this blue shift phenomenon indicates an increase in nanoparticles under 20 nm and a decrease in average nanoparticle size in the LAL method.

Therefore, CeO_2 nanoparticles synthesized through LAL are smaller, spherical, and have a uniform size distribution, making them ideal for facilitating effective combination with graphene oxide (GO) in the fabrication of CeO_2/rGO complexes (Chapter 5). This uniformity and smaller size contribute to improved optical properties and potential applications in areas requiring high-quality UV absorption and dispersion stability.

4.3.2 Filtering Efficiency and Production Calculation

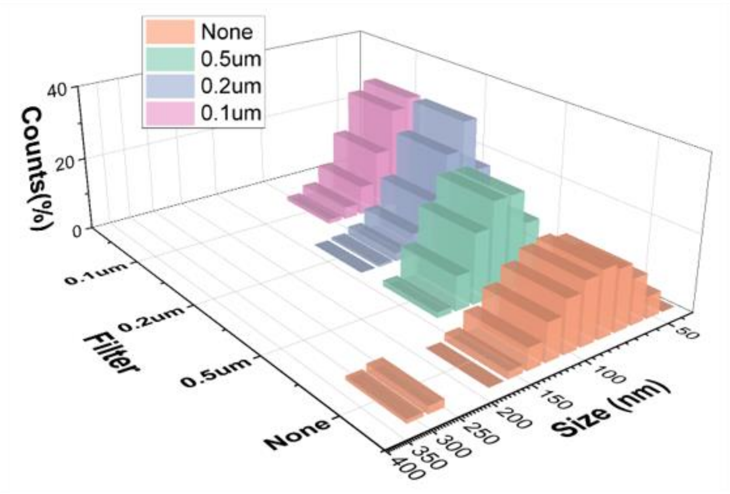

Figure 4-4. DLS of secondary particle sizes after each filter (no filter, 0.5um, 0.2um, 0.1um)

Filter	d (nm)	σ (nm^2)	PDI $(d / \sigma)^2$	Zeta potential (ζ)
None	116.71	99.37	0.725	31.8
0.5um	85.42	42.79	0.251	49.6
0.2um	75.65	27.89	0.136	51.3
0.1um	48.21	13.11	0.074	53.8

Table 4-2. Calculation of the PDI value based on the secondary particle size distribution in Figure 4-4 after each filter and the zeta potential

The particle size distribution and uniformity of CeO_2 nanoparticles after filtration were analyzed using different pore sizes: none, 0.5 µm, 0.2 µm, and 0.1 µm. The results are illustrated in Figure 4-4 and Table 4-2.

As the filter pore size decreased, the average secondary particle size of the CeO_2 nanoparticles also decreased. Specifically, the mean particle size dropped from 116.71 nm with no filter to 48.21 nm with the 0.1 µm filter. This trend indicates that smaller filter sizes are more effective in removing larger particles and aggregates, resulting in a finer and more uniform particle size distribution. The Polydispersity Index (PDI), which measures the breadth of the particle size distribution, also improved with decreasing filter size. The PDI values were 0.725 with no filter, 0.251 with the 0.5 µm filter, 0.136 with the 0.2 µm filter, and 0.074 with the 0.1 µm filter. Lower PDI values indicate a more monodisperse system, signifying that the filtration process effectively narrows the size distribution of the nanoparticles. The PDI values close to zero across all filtered samples reflect a highly uniform distribution of CeO_2 nanoparticles.

Additionally, the zeta potential measurements, shown in Table 4-2, revealed an increase in the stability of the nanoparticle dispersions with smaller filter sizes. The zeta potential increased from 31.8 mV with no filter to 53.8 mV with the 0.1 µm filter. Higher zeta potential values indicate stronger electrostatic repulsion between particles, which prevents aggregation and promotes stable dispersion in the solution.

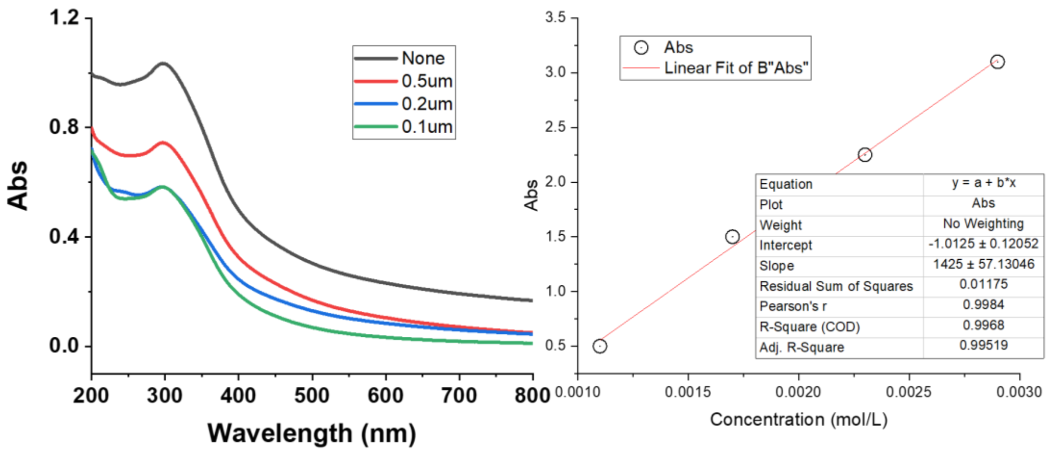

Figure 4-5. UV-vis spectrum after each filter and linear fitting of absorption peak effect on concentration

To determine the concentration of CeO_2 nanoparticles in suspension after filtration, UV-Vis spectroscopy data were utilized. The concentration was calculated using the Beer-Lambert law, which relates the absorbance of a solution to its concentration [133]. The Beer-Lambert law is expressed as (4-2):

$$A = \varepsilon l c \tag{4-2}$$

Where A is the absorbance, ε is the molar absorptivity coefficient, l the optical path length, and c is the concentration of the attenuating species.

Firstly, a calibration curve was established using known concentrations of CeO_2 nanoparticles to determine the molar absorptivity coefficient (ε) and the intercept (y_0). The UV-Vis absorbance values for these known concentrations were plotted, and a linear fit was applied to the data. From this fit, the slope (εl) and the intercept ($y0$) were obtained (Figure 4-5).

The equation derived from the calibration curve is:

$$A = \varepsilon l c + y_0 \qquad (4\text{-}3)$$

$$A=1425c - 1.0125 \qquad (4\text{-}4)$$

For the unknown concentrations of the filtered CeO_2 suspensions, the absorbance values were measured using UV-Vis spectroscopy. These absorbance values were then used in conjunction with the calibration equation to solve for the unknown concentrations. The calculation steps were as follows:

1. Measure the Absorbance: The absorbance (A) of the CeO_2 suspension at a specific wavelength was measured using a UV-Vis spectrophotometer.
2. Apply the Calibration Equation: The calibration equation derived from the known concentrations was used to calculate the concentration. For instance, using the equation (4-4), the concentration (c) was calculated as:

$$c = \frac{A+1.0125}{1425} \qquad (4\text{-}5)$$

Using this method, the concentrations of CeO_2 suspensions after each filtration were calculated. Table 4-3 presents the measured absorbance values, calculated concentrations, and the corresponding yield percentages. The yield was calculated by comparing the concentration after filtration to the initial concentration (before filtration).

Filter	**Abs**	**C (mol/mL)**	**Yield**
None	1.03	1.43	100%
0.5 um	0.74	1.23	86%
0.2 um	0.58	1.12	78%
0.1 um	0.58	1.12	78%

Table 4-3. Calculation on NPs yields after each filter.

These calculations confirmed that filtration effectively reduces the concentration of larger particles, leading to a more uniform nanoparticle suspension with improved stability, as indicated by the zeta potential measurements. This process ensures the production of high-quality CeO_2 nanoparticles suitable for various applications. The use of UV-Vis data and the Beer-Lambert law provides a reliable method for quantifying the concentration of nanoparticles post-filtration, facilitating precise control over the synthesis process.

4.3.3 Advanced Data Science Techniques for SEM Image Analysis

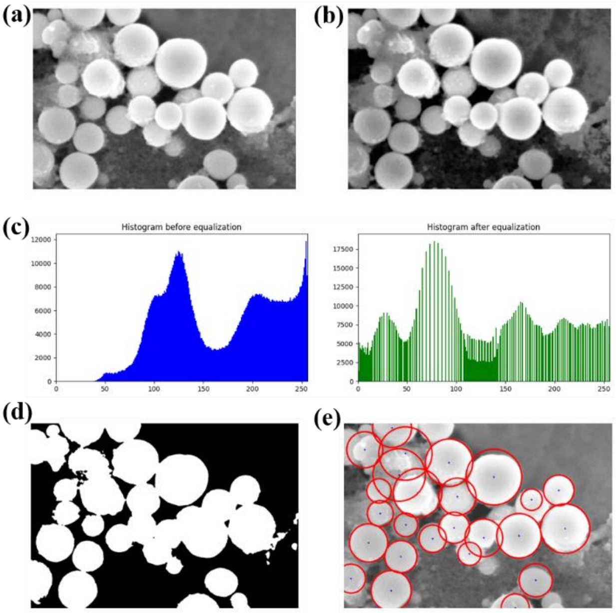

Figure 4-6. Optimization process of SEM data. (a) raw data, (b) SEM data after bilateral filter and histogram equalization, (c) Histogram of grayscale values before and after equalization, (d) Binarized SEM image using Otsu's thresholding, (e) Final image with calculated perimeter

To accurately determine the size distribution of CeO_2 nanoparticles synthesized by different methods, advanced data science techniques were employed to analyze the Scanning Electron Microscope (SEM) images. The process involves several steps to ensure precise identification and measurement of the nanoparticles. Initially, the SEM images were read and converted to grayscale using OpenCV [134]. This conversion is essential for further processing as it simplifies the image data. To enhance the image quality and remove noise while preserving edges, a bilateral filter was applied. Histogram equalization was performed to improve the contrast of the image, making the nanoparticles more distinguishable from the background (Figure 4-6, c). Next, Otsu's thresholding method was used to binarize the image. This technique automatically determines the optimal threshold value to separate the foreground (nanoparticles) from the background. The Hough Circle Transform was then employed to detect circular shapes in the binarized image. This method is effective for identifying spherical nanoparticles. If circles were detected, they were validated based on the percentage of non-zero pixels within each circle's mask. This step ensures that only true nanoparticles are counted, reducing the impact of false positives. Finally, the results were visualized through histograms and annotated images. Histograms before and after equalization were plotted to show the improvement in contrast. The binarized image and the output image with detected nanoparticles were also displayed for verification. Furthermore, the simulated particle sizes from plenty of raw SEM data could be directly analyzed to get the size distribution bar chart in a simple way.

4.4 Summary

This chapter explores the optimization of CeO_2 nanoparticles (NPs) production using the Laser Ablation in Liquid (LAL) method with focused laser irradiation and compares it to the traditional precipitation method. The LAL method, which involves concentrating a laser beam onto a small area of a CeO_2 target in a liquid medium, enhances the energy density and efficiency of nanoparticle production. This process leads to the formation of high-purity, uniformly sized, and spherical nanoparticles. In contrast, the precipitation method, which involves mixing chemical precursors in a solution, often results in impurities and a broad size distribution, requiring extensive purification steps. Advanced data science techniques, including SEM image processing and dynamic light scattering (DLS), were employed to analyze and compare the morphology and size distribution of nanoparticles produced by both methods. The nanoparticles were analyzed using SEM, DLS, and UV-Vis spectroscopy. The SEM analysis revealed that LAL-synthesized nanoparticles were smaller (43.2 nm average size) and more uniform in size and shape compared to those produced by the precipitation method (83.4 nm average size). The DLS analysis confirmed a narrower size distribution and lower polydispersity index (PDI) for LAL nanoparticles, indicating reduced aggregation and better dispersion stability. UV-Vis spectroscopy showed a blue shift in the absorption peak for LAL nanoparticles, indicating smaller particle sizes and a higher bandgap energy.

Further analysis focused on the filtration efficiency and production yield of CeO_2 nanoparticles. Filtration using different pore sizes (0.5 μm, 0.2 μm, and 0.1 μm) resulted in progressively smaller and more uniform particle sizes, with the 0.1 μm filter producing the most stable dispersion with a zeta potential of 53.8 mV. The concentration of nanoparticles after filtration was determined using UV-Vis spectroscopy and the Beer-Lambert law, confirming that filtration effectively reduces the concentration of larger particles. Advanced data science techniques were employed to optimize SEM image analysis, involving grayscale conversion, bilateral filtering, histogram equalization, Otsu's thresholding, and Hough Circle Transform for detecting and measuring spherical nanoparticles. This automated analysis provided a robust evaluation of nanoparticle size distribution.

In summary, the focused laser ablation method produced superior CeO_2 nanoparticles in terms of size uniformity, shape, and UV absorption properties compared to the precipitation method. The optimized LAL process, supported by advanced SEM data processing, highlights the advantages of laser ablation in producing high-quality nanoparticles with potential applications in UV protection and other areas requiring precise nanoparticle characteristics.

References

[111] M. D. Aglio, R. Gaudiuso, O. De Pascale, A. De Giacomo. *Appl. Surf. Sci.*, 348 (2015) 4.

[112] M.P. Mateo, L.M. Cabalín, J. Laserna. *Appl. Opt.*, 42, 30 (2003) 6057.

[113] C.Y. Shih, M.V. Shugaev, C. Wu, L.V. Zhigilei. *Phys. Chem. Chem. Phys.*, 22 (2020) 7077.

[114] M. Ullmann, S.K. Friedlander, A. Schmidt-Ott. *J. Nanopart. Res.*, 4 (2002) 499

[115] T. Takiya, M. Han, M. Yag. *Thermodynamics of Nanoparticle Formation in Laser Ablation. InTech* (2011).

[116] M.F. Becker, J.R. Brock, H. Cai, D.E. Henneke, J.W. Keto, J. Lee, W.T. Nichols, H.D. Glicksman. *Nanostruct. Mater.*, 10, 5 (1998) 853.

[117] F. Taccogna. Nucleation and growth of nanoparticles in a plasma by laser ablation in liquid. *J. Plasma Phys.*, 81, 5 (2015) 495810509.

[118] H. C. Schwarzer and W. Peukert: *Chem. Eng. Commun.*, 1191, (2004) 580.

[119] C. Nayral, E. Viala, P. Fau, F. Senocq, J. Jumas, A. Maisonnat, and B. Chaudret., *Eur. J. Chem.*, 6, (2000) 4082

[120] J. Knipping, H. Wiggers, B. Rellinghaus, P. Roth, D. Konjhodzic, C. Meier. *J. Nanosci. Nanotechnol.*, 4, 8 (2004) 1039.

[121] S. Paris, P. Kornprobst, J. Tumblin, F. Durand. *Found. Trends Comput. Graph. Vis.*, 4, 1 (2009) 1.

[122] C. Sha, J. Hou, H. Cui. *J. Vis. Commun. Image Represent.*, 41 (2016) 339.

[123] J. Illingworth, J. Kittler. *Comput. Vis. Graph. Image Process.,* 44, 1 (1988) 87.

[124] E. Fazio, B. Gökce, A.D. Giacomo, M. Meneghetti, G. Compagnini, M. Tommasini, F. Waag, A. Lucotti, C.G. Zanchi, P.M. Ossi, M. Dell'Aglio, L. D'Urso, M. Condorelli, V. Scardaci, F. Biscaglia, L. Litti, M. Gobbo, G. Gallo, M. Santoro, S. Trusso, F. Neri. *Nanomaterials (Basel)*, 10 (2020) 2317.

[125] D. Zhang, B. Gökce, C. Notthoff, S. Barcikowski. *Sci. Rep.*, 5 (2015) 13661.

[126] H. Wang, A.A. Pyatenko, K. Kawaguchi, X. Li, Z. Warkocka, N. Koshizaki. Angew. Chem. Int. Ed., 122 (2010) 6505.

[127] A. Pyatenko, M. Yamaguchi, M. Suzuki. *J. Phys. Chem.*, 22 (2007) 111.

[128] M.P. Navas, R.K. Soni, N. Tarasenka, N. Tarasenko. *Appl. Surf. Sci.*, 414 (2017) 413.

[129] A. Kanitz, M.R. Kalus, E.L. Gurevich, A. Ostendorf, S. Barcikowski, D. Amans. *Plasma Sources Sci. Technol.*, 28 (2019) 103001.

[130] Z. Yang, R. Tian, J. Wu, Q. Fan, B.C. Yung, G. Niu, O. Jacobson, Z. Wang, G. Liu, G. Yu, W. Huang, J. Song, X. Chen. *ACS Nano*, 11, 4 (2017) 4247.

[131] V. Khoshkava and M. R. Kamal, *Biomacromolecules*, 14, (2013) 3155.

[132] A.M. Ali and S. Hasegawa, *Thin Solid Films*, 437, (2003) 68.

[133] L. Kocsis, P. Herman, A. Eke. *Phys. Med. Biol.,* 51 (2006) N91.

[134] T. Celebi, I. Shayea, A.A. El-Saleh, S. Ali, M. Roslee. *Histogram Equalization for Grayscale Images and Comparison with OpenCV Library.* 2021 IEEE 15th Malaysia International Conference on Communication (MICC), Malaysia, 2021, 92.

Chapter 5

Electrochemical Properties of CeO_2 NPs in Modifying the rGO-GCE Electrode

5.1 Introduction

5.1.1 Ammonia Monitoring in the Biomedical Field

Monitoring ammonia (NH^{4+}) levels in the biomedical field is of critical importance due to its direct implications on human health [135, 136], particularly in patients with liver disease [137]. The liver is responsible for processing ammonia, converting it into urea for excretion. However, in conditions such as cirrhosis [138], the liver's capacity to handle ammonia diminishes, leading to its accumulation in the blood. This elevated ammonia level can precipitate hepatic encephalopathy [139], a serious neuropsychiatric syndrome characterized by cognitive dysfunction, altered consciousness [140], and even coma [141]. The necessity of effective ammonia monitoring is underscored by the metabolic origins of ammonia in the body. Ammonia is primarily produced from the catabolism [142] of amino acids in various organs, including the intestines, muscles, and kidneys. Certain amino acids, such as arginine (Arg), asparagine (Asn), glutamine (Gln), histidine (His), lysine (Lys), and methionine (Met), have a higher potential to generate ammonia, exacerbating the condition in individuals with impaired hepatic function.

Given the potential for ammonia to cause severe health complications, real-time monitoring of blood NH^{4+} levels is essential. Ammonia sensors play a pivotal role in this regard, providing a means to continuously assess ammonia levels in the blood. Such sensors are vital tools in the management of liver diseases, helping to prevent the onset of hepatic encephalopathy by enabling timely medical interventions.

5.1.2 Electrochemical Gas Sensor

Electrochemical gas sensing is a widely used and effective technique for detecting and monitoring gases in various applications [143]. This method is favored for its high sensitivity, selectivity, and rapid response times, making it essential for safety, environmental monitoring [144], and industrial processes [145]. The principle of electrochemical gas sensing relies on the interaction between target gas molecules and electrodes to generate electrical signals [146].

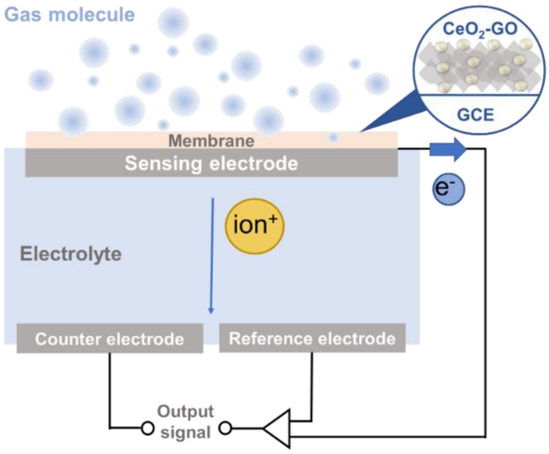

Figure 5-1. schematic of electrochemical gas sensor

In this research, the electrochemical sensor is designed to detect ammonia using a CeO_2/rGO/GCE electrode (Figure 5-1). When gas molecules come into contact with the membrane of the sensing electrode, a significant accumulation of ions and electrons occurs. These ions then migrate through the electrolyte toward the counter electrode, while the electrodes establish an external circuit to generate an output signal. The sensing electrode acts as a transducer, converting gas interactions into measurable electrical signals [147]. The CeO_2/rGO/GCE electrode used in this study combines cerium oxide nanoparticles with graphene oxide and a glassy carbon electrode, enhancing the sensor's performance. The oxidation-reduction reaction at the sensing electrode is detected, producing an anodic peak that allows for quantitative analysis. This setup ensures a high level of sensitivity and specificity in detecting ammonia, making it a reliable tool for monitoring this gas in biomedical applications.

5.1.3 Modification of Graphene Oxide to Reduced Graphene Oxide

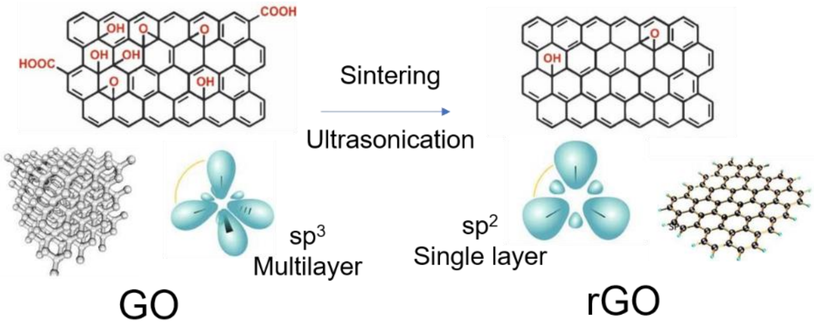

Figure 5-2. Material structure of GO and rGO [159]

In recent years, graphene oxide (GO) has emerged as a promising material for gas sensing applications [148]. GO possesses excellent chemical stability [149], a large surface area [150], and tunable properties [151], making it an ideal candidate for sensing electrode fabrication. However, the pristine form of GO typically exhibits lower electrical conductivity due to the presence of oxygen functional groups [152,153]. This lower conductivity can limit its sensing performance and response time. To overcome this limitation, efforts have been made to improve the electrical properties of GO by reducing it to reduced graphene oxide (rGO) through various methods such as chemical [154] or thermal reduction [155]. The reduction process removes a significant portion of the oxygen functional groups, thereby restoring the sp^2 carbon network and significantly improving the electrical conductivity of the material.

The principle behind this modification involves breaking the oxygen-carbon bonds and removing the functional groups through heat or chemical processes. This transformation enhances the desirable properties of GO, such as its electrical conductivity [156], which is crucial for efficient gas sensing. Reduced graphene oxide (rGO) features more defects and dangling bonds [157], which can further enhance its gas sensing capabilities by providing more active sites for gas molecule interaction [158]. In this research, the preparation of rGO from GO is essential to enhance the performance of the CeO_2/GO/GCE electrode. By improving the conductivity and maintaining the large surface area, the modified rGO can contribute to a more responsive and sensitive ammonia sensor, ensuring better monitoring and detection in biomedical applications.

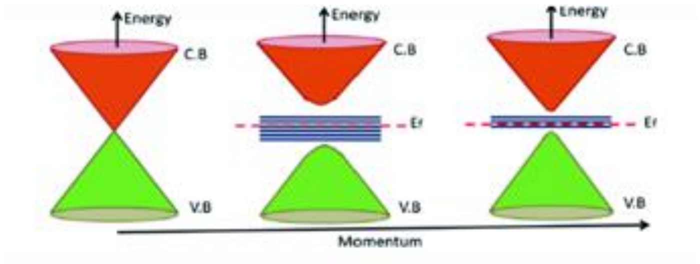

Figure 5- 3. Energy band gap of graphene, GO and rGO (left to right) [160]

The transition from graphene to graphene oxide (GO) and subsequently to reduced graphene oxide (rGO) not only involves significant changes in the lattice structure but also in the energy band gap, which directly affect the material's electrical conductivity and sensitivity [160].

Graphene as a previously used sensing electrode material is a single layer of carbon atoms arranged in a hexagonal lattice [161]. It exhibits exceptional electrical conductivity due to its unique band structure, where the conduction band (C.B) and the valence band (V.B) meet at the Dirac points with no band gap [162]. This zero band gap allows electrons to move freely, resulting in high electrical conductivity. However, the lack of functional groups on graphene limits its chemical reactivity and sensitivity in gas sensing applications, as there are fewer sites for gas molecules to interact with the graphene surface [163]. When graphene is oxidized to form GO, oxygen-containing functional groups such as hydroxyl (-OH), carboxyl (-COOH), and epoxy (-O-) groups are introduced onto the graphene plane [164]. These functional groups disrupt the sp^2 hybridized carbon network, converting some of the sp^2 bonds to sp^3 bonds [165]. This disruption introduces a band gap between the conduction band and the valence band, as shown in the middle diagram. The presence of a band gap reduces the electrical conductivity of GO compared to pristine graphene, as the electrons require additional energy to jump across the band gap [166]. The functional groups, however, provide active sites for chemical interactions, increasing the sensitivity of GO in sensing applications. Through processes like ultrasonication and sintering, GO can be reduced to rGO by removing a significant portion of the oxygen-containing functional groups [167]. This reduction process partially restores the sp^2 hybridized carbon network, thereby decreasing the band gap and enhancing the electrical conductivity [168]. The structure of rGO retains some residual functional groups, but the overall conjugated structure is more restored compared to GO. The transition from graphene to GO introduces a band gap that reduces conductivity but increases chemical sensitivity. The reduction of GO to rGO decreases the band gap, enhancing both the electrical conductivity and sensitivity of the material.

Traditionally, improving the electrical properties of GO involves reducing it to reduced graphene oxide (rGO) through harsh chemical treatments [169] or high-temperature annealing [170]. These methods often utilize strong reducing agents or extreme temperatures, which can introduce impurities or damage the graphene structure, thereby compromising its electrical conductivity and gas sensing performance. In contrast, the ultrasonication method offers a milder and innovative approach to preparing rGO from GO [171]. The ultrasonication method uses ultrasonic energy to break the weak intermolecular forces in GO [172], effectively peeling off layers to form rGO. This technique involves immersing GO in a liquid medium and subjecting it to high-frequency ultrasonic waves. The ultrasonic energy generates cavitation bubbles in the liquid, which collapse violently, producing shock waves that peel off the graphene oxide layers [173]. This process results in the exfoliation of GO into thinner and smaller sheets of rGO, significantly improving its electrical conductivity. Sintering is another method employed to convert GO to rGO by heating GO at controlled temperatures. The combination of sintering and ultrasonication provides an efficient way to produce high-quality rGO. Sintering helps in partially reducing the GO and breaking down its structure, while ultrasonication further exfoliates these reduced structures into fine, single-layer or few-layer graphene sheets. This dual approach not only preserves the structural integrity of graphene but also enhances its electrical properties, making rGO more suitable for gas sensing applications.

5.1.4 Synergistic Effect

The combination of CeO_2 and reduced graphene oxide (rGO) creates a synergistic effect [174] that significantly enhances the performance of the ammonia sensor. This synergistic effect is primarily achieved through two mechanisms: enhanced redox chemistry and improved dispersion.

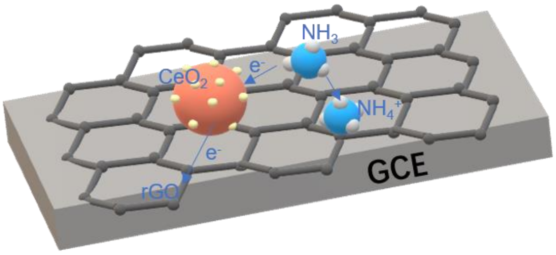

Figure 5-4. Schematic of synergistic effect

Firstly, CeO_2, being an n-type semiconductor, has the ability to donate or accept oxygen vacancies and electrons. When combined with rGO, which contains oxygen-functional groups acting as electron acceptors (p-type), a p-n heterojunction is formed. This heterojunction facilitates efficient redox reactions on the surface of CeO_2, enhancing the electron transfer and oxygen exchange between CeO_2 and the target gas [175]. The redox reactions between CeO_2 and NH^{4+} generate electrons for the circuit, significantly improving the sensor's sensitivity and conductivity.

Secondly, rGO serves as an excellent support material for CeO_2 nanoparticles, aiding in their uniform dispersion. The large surface area and presence of functional groups on rGO help to disperse CeO_2 nanoparticles more uniformly, reducing agglomeration and providing a higher surface area for interaction with NH^{4+} ions. This uniform dispersion further enhances the conductivity of the sensor, as the well-dispersed CeO_2 nanoparticles ensure consistent and efficient electron transfer [176].

5.2 Experiment

5.2.1 Preparation of CeO_2-rGO Nanocomposite

Initially, the graphene oxide (GO) was transformed into reduced graphene oxide (rGO) by sintering at three different temperatures: 300°C, 500°C, and 700°C. Further reduction of the rGO was achieved through ultrasonication, which involves dispersing 8 mg of rGO (SIGMA-ALDRICH, Co., 15-20 sheets, 10% edge-oxidized) in 50 mL of pure water and applying ultrasonic energy for 2 hours. This method provides a milder and more efficient way to obtain rGO without the need for harsh chemical treatments, thus preserving the integrity of the graphene structure and enhancing its properties for gas sensing applications.

Following the ultrasonication, CeO_2 nanoparticles prepared via the laser ablation in liquid method were introduced into the rGO suspension. The mixtures were prepared in various mole ratios of rGO to CeO_2: specifically, 4:1, 2:1, 1:1, 1:2, and 1:4. The suspension was then subjected to an additional 30 minutes of ultrasonication and stirring under a pH value of 7.4 to ensure thorough mixing and interaction between the CeO_2 nanoparticles and the rGO sheets.

After this process, the suspension was left undisturbed for 24 hours to facilitate precipitation. The resulting precipitate was collected by centrifugation and subsequently freeze-dried to remove any residual moisture. This process yielded the CeO_2-rGO nanocomposite samples with different rGO to CeO_2 ratios, ready for further analysis and application in electrochemical sensors for NH_3 monitoring.

5.2.2 Morphology Analysis

The synthesized CeO_2-rGO nanocomposites were characterized using a combination of XRD, SEM, and EDS techniques. These methods provided comprehensive insights into the doping situation of the nanocomposite, as well as its morphology and particle size distribution. XRD was utilized to determine the crystalline structure and phase purity of the composites, while SEM provided detailed images of the doping morphology. EDS offered elemental composition analysis to confirm the presence of CeO_2 and rGO.

5.2.3 Electrochemical Analysis

UV-Vis Spectroscopy

UV-Vis spectroscopy was conducted to estimate the band gap of the CeO_2-rGO nanocomposites. The band gap estimation served as a preliminary indicator of the electrical conductivity of the composites. The Tauc plot method was used to determine the optical band gap, which provided insights into the electronic structure and potential applications in sensing.

Cyclic Voltammetry (CV) Test

The prepared suspensions of CeO_2-rGO composites (4:1, 2:1, 1:1, 1:2, 1:4 in molar ratio) and pure CeO_2 or rGO suspensions were drop-cast onto glassy carbon electrodes (GCE). The coating material was applied five times, followed by oven drying at 80°C to ensure proper adhesion and uniformity.

The first experiment aimed to detect the redox peak positions and evaluate the baseline electrochemical properties of the electrodes without exposure to the target gas. A standard redox probe solution (1 mM $K_3[Fe(CN)_6]$ in 0.5M KCl) was used as the electrolyte. The CV measurements were conducted with varying scan rates (5, 10, 20, and 40 mV/s). The working electrode area was 0.07 cm^2, and the potential range was set from 0.8 V (anodic limit) and -0.2 V (cathodic limit), sample at intervals of 5 mV for 3 cycles.

The second experiment aimed to detect characteristic redox peaks of ammonia and evaluate the sensitivity of the sensor. Ammonia solutions of varying concentrations (0.5, 1, and 2 M/L) were added to the 0.5M KCl electrolyte. The CV measurements were repeated for different coatings (each ratio of the composite, pure CeO_2 and rGO) and scan rates (10, 20, 30, and 40 mV/s). The working electrode area was 0.07 cm², and the potential range was set from 1.5 V to 0 V, sample at intervals of 5 mV for 3 cycles.

5.3 Results and Discussion

5.3.1 Characteristic of CeO_2-rGO composite

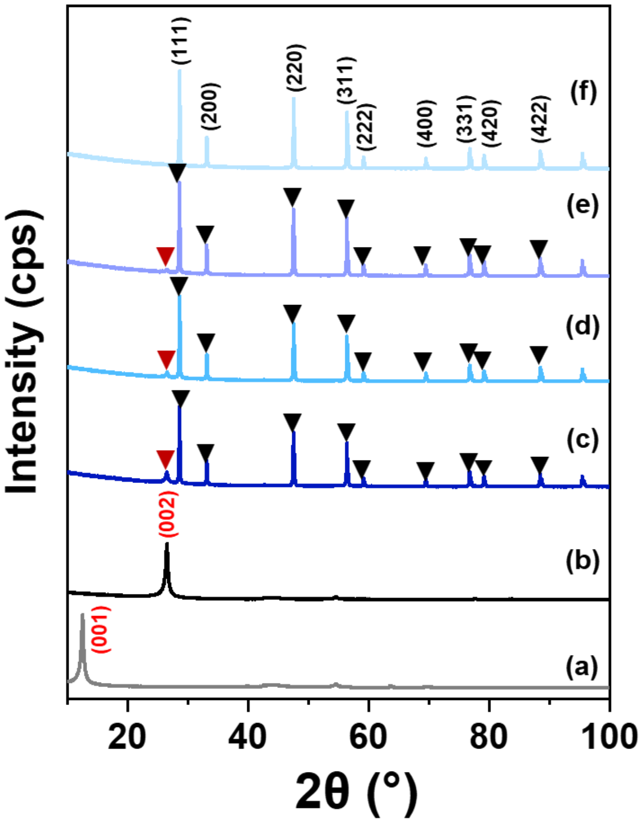

Figure 5- 5. XRD pattern of (a) GO (b) rGO (c) $1CeO_2/2rGO$ (d) $1CeO_2/1rGO$ (e) $2CeO_2/1rGO$ (f) CeO_2

The XRD patterns of raw GO, rGO, and CeO_2/rGO nanocomposites in varying mole ratios, alongside pure CeO_2, are illustrated in Figure 5-5. The characteristic peak of GO, identified at (001), confirms the structured layers of graphene oxide in the raw GO sample (Figure 5-5, a). Upon sintering and ultrasonication, this (001) peak is replaced by the (002) peak in the rGO sample (Figure 5-5, b), signifying the successful reduction and exfoliation of GO into rGO, resulting in thinner, more separated layers. The diminished intensity of the peaks in rGO compared to GO indicates the increased content of single-layer carbon structures [177], which is a typical outcome of the ultrasonication process.

In the XRD patterns of CeO_2/rGO nanocomposites (Figures 5-5, c-e), the diffraction peaks corresponding to CeO_2 are marked with black inverted triangles at (111), (200), (220), (311), (222), (400), (331), (420), and (422) planes. These peaks confirm the presence of CeO_2 in a cubic fluorite structure within the composites. Notably, as the ratio of CeO_2 increases in the nanocomposites, the characteristic peaks of rGO diminish and nearly disappear. This observation suggests a successful integration of CeO_2 nanoparticles into the rGO matrix, where the CeO_2 nanoparticles are likely intercalated between the rGO layers, reducing the interlayer spacing and contributing to the attenuation of X-ray diffraction signals from rGO.

In comparison with pure CeO_2 nanoparticles (Figure 5-5, f), the CeO_2/rGO nanocomposites exhibit similar characteristic CeO_2 diffraction peaks, indicating that the crystalline structure of CeO_2 is maintained even after composite formation. The nearly absent rGO peaks in the composite samples with higher CeO_2 content (Figures 5-5, d and e) imply a significant interaction between CeO_2 and rGO. This interaction is possibly due to the reduction of rGO by Ce^{3+} ions, leading to a more compact and restored sp^2 carbon network structure. This structural restoration contributes to the shift of the rGO XRD peak to higher angles [178], indicating decreased interlayer spacing.

The absence of additional peaks in the XRD patterns of the nanocomposites suggests that no significant secondary phases are present, affirming the successful synthesis of CeO_2/rGO composites without undesirable byproducts. This comprehensive analysis highlights the structural transformations and successful integration of CeO_2 into the rGO matrix, enhancing the properties of the resulting nanocomposite material.

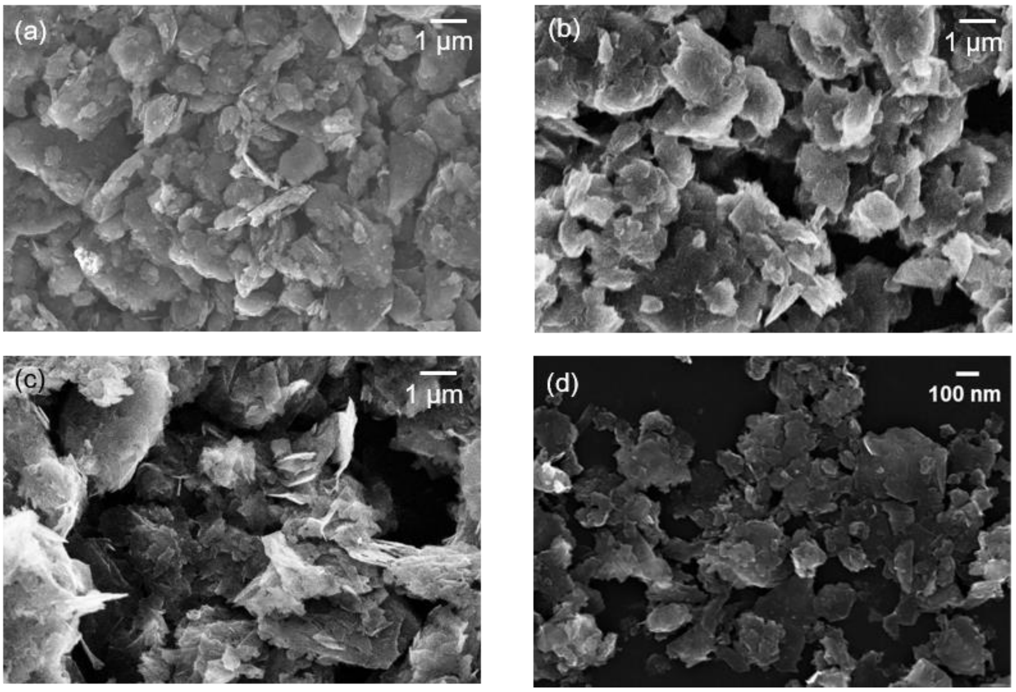

Figure 5-6. SEM images of (a) pure GO, (b) GO after 300 °C sintering, (c) GO after 500°C sintering, (d) rGO after sintering and ultrasonication

The SEM images in Figure 5-6 illustrate the morphology and structure of GO and rGO at different stages of preparation. Figure 5-6 (a) displays pure GO, characterized by its large, multilayered structure with rough surfaces. This image serves as a baseline for understanding the changes induced by thermal and ultrasonic treatments.

In Figure 5-6 (b), GO sintered at 300°C shows a transition from a bulk structure to smaller, more fragmented sheets. The high-temperature sintering causes the large 3D structures to break down into smaller, more manageable 2D sheets. This reduction in size and the formation of more defined sheets indicate partial exfoliation of the graphene layers. Further heating to 500°C, as shown in Figure 5-6 (c), results in even sharper and thinner layers. The SEM image demonstrates a significant structural change, with the GO becoming more distinct and separated. This observation suggests that higher sintering temperatures effectively reduce the interlayer spacing, transforming the GO into a more refined rGO structure. In contrast, when GO is sintered at 700°C, it combusts completely, indicating that this temperature is too high for the preservation of the graphene structure.

Furthermore, Figure 5-6 (d) presents the rGO after sintering and subsequent ultrasonication. The image reveals even smaller and more uniformly distributed sheets compared to the previous stages. The ultrasonic treatment further breaks down the layers, promoting the formation of single-layer or few-layer graphene sheets. This enhanced separation and reduction in size are crucial for improving the electrical conductivity and overall performance of rGO in various applications. The

SEM analysis confirms the structural evolution of GO to rGO through sintering and ultrasonication, highlighting the effectiveness of these methods in producing high-quality rGO with desirable morphological characteristics. The process effectively peels the rGO into thinner, smaller sheets, enhancing its properties for further application.

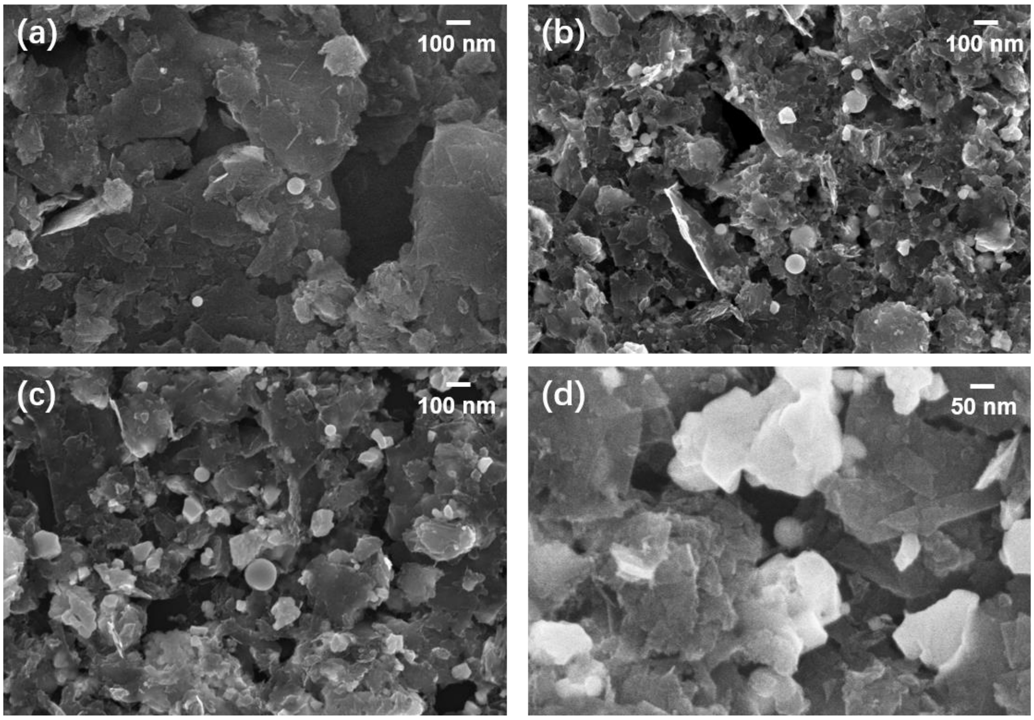

Figure 5-7. SEM images of (a) 1CeO_2/2rGO (b) 1CeO_2/1rGO (c)2CeO_2/1rGO (d) 2CeO_2/1rGO in high magnification

Material	Zeta potential （ζ）
rGO	-42.4 ± 0.2
CeO_2	53.6 ± 2.1

Table 5-1. Zeta potential of rGO and CeO_2

The SEM images in Figure 5-7 illustrate the morphology of CeO_2-rGO nanocomposites with varying proportions of CeO_2. As the CeO_2 content increases from images (a) to (c), the adsorption of CeO_2 nanoparticles on the rGO sheets becomes more pronounced. In these images, spherical CeO_2 nanoparticles can be seen decorating the gaps between rGO sheets, indicating successful incorporation of CeO_2 into the rGO matrix. Figure 5-7 (a) at a lower proportion of CeO_2, the nanoparticles are dispersed relatively uniformly across the rGO sheets. The interaction between CeO_2 and rGO appears to be facilitated by the presence of oxygen-containing functional groups on rGO, which likely bind with Ce^{3+} ions, enhancing the stability of the composite. Figure 5-7 (b) with an increased proportion of CeO_2, the nanoparticles become more densely packed within the rGO framework. The electrostatic attraction between the negatively charged rGO and the positively charged CeO_2 nanoparticles promotes uniform distribution and stable adsorption of CeO_2 between the gaps of the rGO sheets. This uniform dispersion helps in enhancing the electrical conductivity and the overall performance of the composite. Also, at higher CeO_2 concentrations (Figure 5-7, c), while the nanoparticles continue to be adsorbed onto the rGO sheets, the aggregation phenomenon start to appear. The localized heating effect caused by acoustic cavitation during ultrasonication can lead to the aggregation and partial melting of CeO_2 nanoparticles. This effect results in the formation of larger CeO_2 aggregates and platelet-like structures, as seen in the image.

The zeta potential measurements further support these observations (Table 5-1). The zeta potential of rGO is - 42.4 ± 0.2 mV, indicating a negative surface charge, while CeO_2 has a zeta potential of 53.6 ± 2.1 mV, indicating a positive surface charge. The significant difference in zeta potential between rGO and CeO_2 promotes electrostatic attraction, aiding in the uniform adsorption of CeO_2 nanoparticles onto the rGO sheets and enhancing the stability of the nanocomposite. Under high magnification (Figure 5-7 d), it is evident that spherical CeO_2 nanoparticles are well-adhered to the rGO sheets, confirming an effective combination of CeO_2 and rGO. The synergy [179] between rGO and CeO_2 is facilitated by their opposite surface charges, which enhance the uniform adsorption and stability of the nanocomposite. The effective combination of CeO_2 and rGO is attributed to the electrostatic interactions and the binding of Ce^{3+} ions with oxygen-based functional groups on rGO, which improve the charge mobility and the overall conductivity of the nanocomposite.

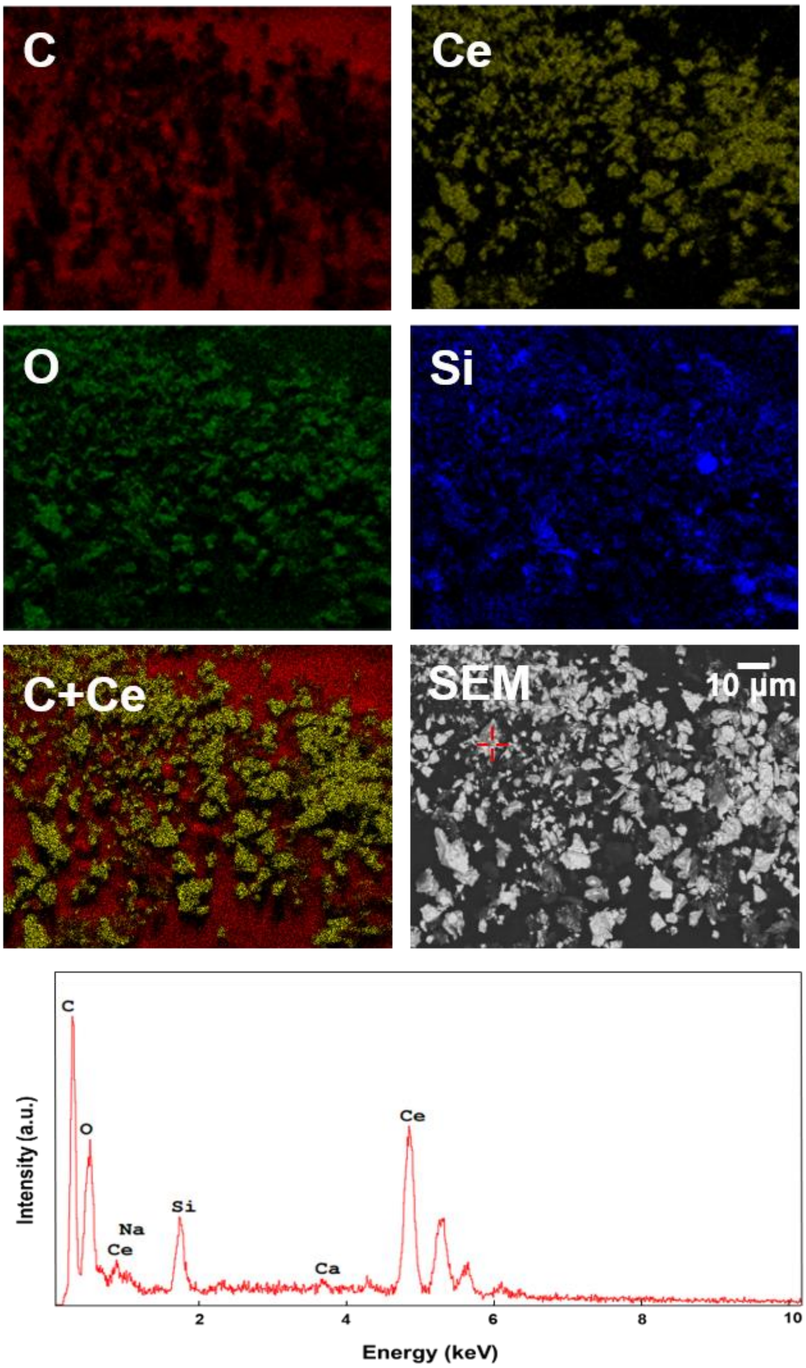

Figure 5-8. SEM image and EDS mapping with enhanced contrast of the element distribution and uniformity analysis of the CeO_2-rGO complex in a molar ratio of 1:1.

To further validate the uniform distribution, point analysis was conducted at several randomly selected locations (as indicated by the red cross in the SEM image). The Energy-Dispersive X-ray Spectroscopy (EDS) mapping in Figure 5-8 provides a detailed analysis of the elemental composition and distribution within a CeO_2-rGO nanocomposite with a molar ratio of 1:1. The SEM image (bottom right) offers a structural overview, which is crucial for correlating the elemental distribution observed in the EDS maps. The individual EDS maps for carbon (C), cerium (Ce), oxygen (O), and silicon (Si) are displayed, revealing the spatial distribution of these elements within the nanocomposite. Notably, the combined EDS map (C + Ce) clearly shows that carbon and cerium are uniformly distributed across the sample, indicating a successful and homogeneous decoration of CeO_2 nanoparticles on the rGO sheets. The combined EDS map (C + Ce) emphasizes the successful integration of CeO_2 with rGO, highlighting the uniform decoration of cerium on the carbon matrix. This homogeneity is crucial for ensuring consistent electrical properties and sensor performance.

5.3.2 Calculation of Energy Band Gap by UV-vis

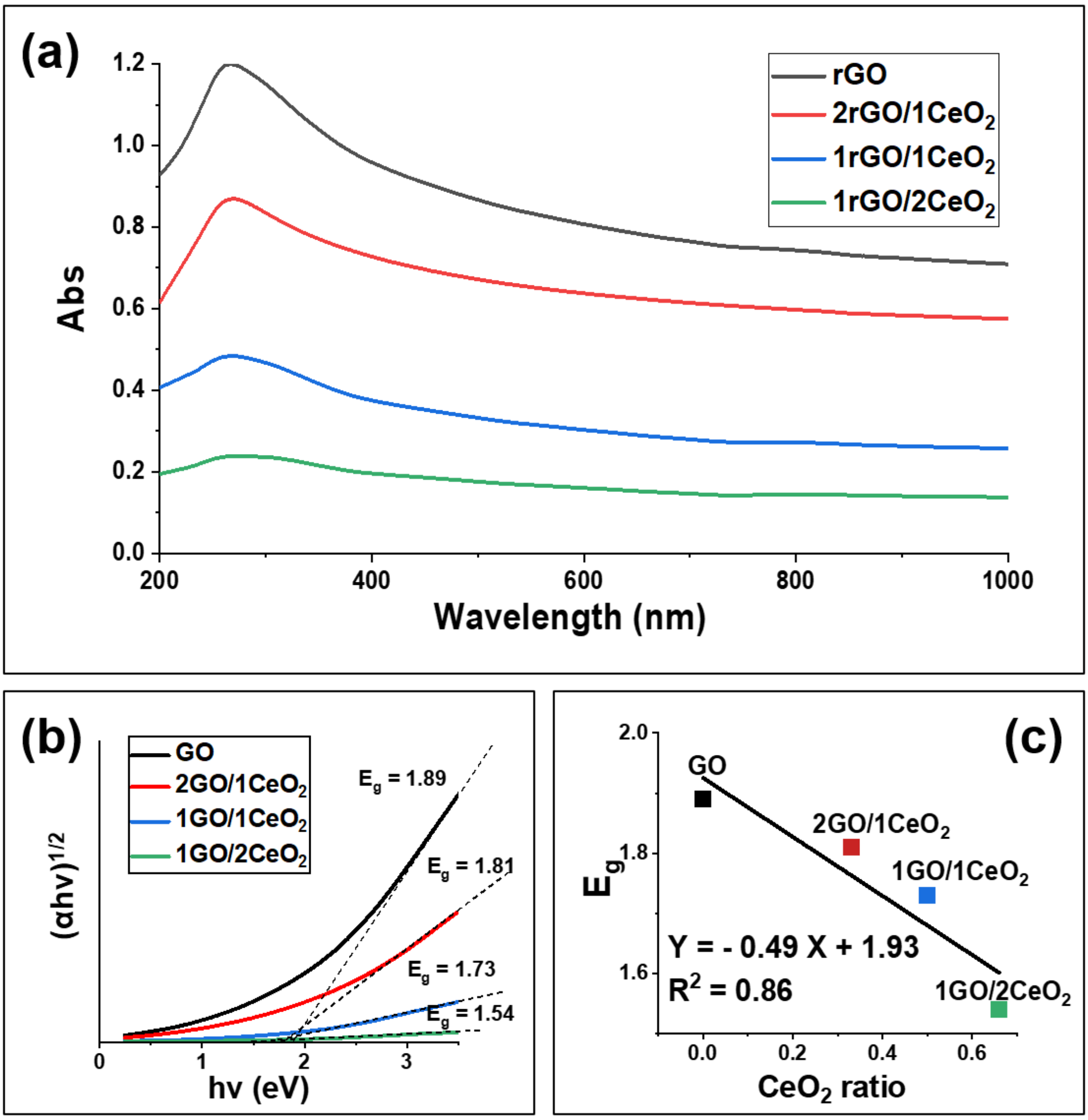

Figure 5-9. (a) UV-vis of the effect on the complex ratio. (b) Tauc plot of (a). (c) Eg as a function of the CeO_2 ratio with the liner fitting

Figure 5-9 illustrates the UV-vis spectra and Tauc plots for CeO_2-rGO nanocomposites with varying mole ratios of CeO_2. The UV-vis spectra in Figure 5-9 (a) show the absorption peaks of the nanocomposites, with the absorption intensity decreasing as the CeO_2 ratio increases. This trend indicates a direct correlation between the CeO_2 content and the optical properties of the nanocomposites, suggesting that higher CeO_2 content leads to reduced UV absorption.

To further analyze the energy band gap, Tauc plots were constructed based on the UV-vis spectra (Figure 5-9, b). The Tauc plot is a method used to estimate the optical band gap of a material. The energy band gap (Eg) can be determined by plotting $(\alpha h v)^2$ versus photon energy (hv) and extrapolating the linear portion of the plot to the hv axis, where α is the absorption coefficient, h is Planck's constant, and v is the frequency of the incident photon. The Tauc plot in Figure 5-9 (b) reveals that the energy band gap decreases as the CeO_2 content increases. This phenomenon can be attributed to the synergistic effect between rGO and CeO_2 within the nanocomposites. rGO possesses exceptional electrical properties due to its two-dimensional hexagonal lattice structure and high charge carrier mobility. When CeO_2 nanoparticles are incorporated into the rGO matrix, they can act as conductive bridges, enhancing the electron transfer between graphene nanosheets and significantly improving the overall electrical conductivity [180]. Furthermore, the incorporation of CeO_2 nanoparticles introduces defects and surface states into the nanocomposites, which can influence the energy band structure. These defects and surface states contribute to the reduction in the energy band gap, particularly near the interface with rGO [181]. The reduction in the band gap is beneficial for applications requiring efficient charge transport, such as in electrical components. The presence of these defects enhances the charge mobility and facilitates better electrical performance of the nanocomposites.

Figure 5-9 (c) illustrates the linear relationship between the CeO_2 ratio and the energy band gap, confirming that the energy band gap decreases proportionally with the increase in CeO_2 content. This correlation has an R^2 value of 0.86, indicating a strong linear relationship and this fitting demonstrates that for every unit increase in the CeO_2 ratio, there is a significant decrease in the energy band gap.

Overall, the UV-vis and Tauc plot analyses demonstrate that increasing the CeO_2 ratio in CeO_2-rGO nanocomposites effectively reduces the energy band gap, thereby enhancing the electrical conductivity and potential applications in electronic devices. The synergistic effects between rGO and CeO_2 lead to improved electrical properties, making these nanocomposites suitable for various advanced technological applications.

5.3.3 The Standard Test of Sensitivity for Modified Electrode Coating

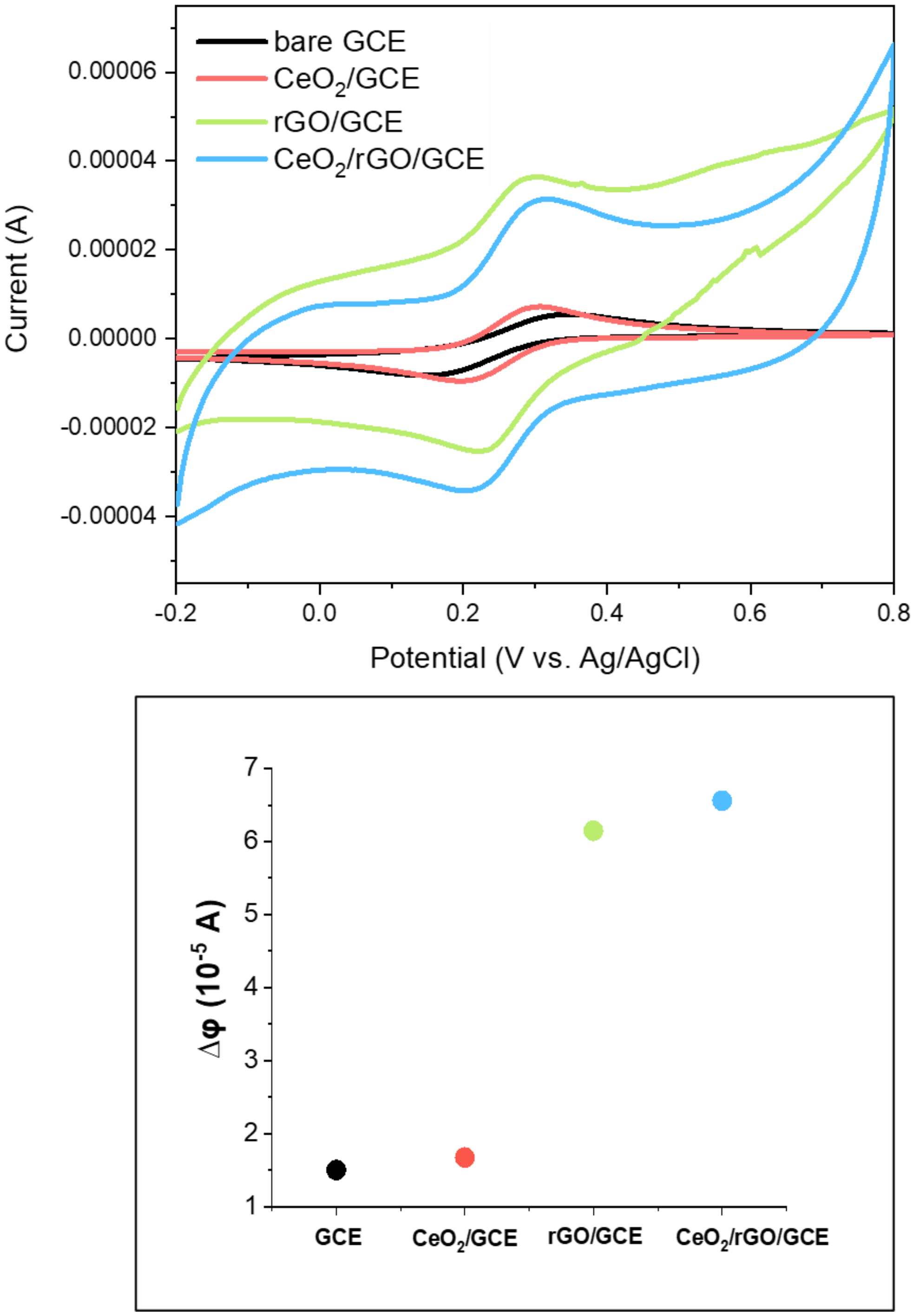

Figure 5-10. Cyclic voltammetry plots of GCE with different coatings (bare GCE, CeO_2/GCE, rGO/GCE, CeO_2/rGO/GCE) in the presence of 1 mM $K_3[Fe(CN)_6]$ in 0.5 M KCl, with a scan rate of 10 mV/s and the Δφ value between each redox peak

Figure 5-10 of cyclic voltammetry plots illustrates the electrochemical behavior for different GCE coatings (bare GCE, CeO_2/GCE, rGO/GCE, CeO_2/rGO/GCE) in a 1 mM $K_3[Fe(CN)_6]$ solution with 0.5 M KCl electrolyte at a scan rate of 10 mV/s. The CV measurements were conducted within a potential range of -0.2 V to 0.8 V to evaluate the electrochemical properties of the modified electrodes.

The black curve representing the bare GCE shows negligible current response, indicating poor electrochemical activity. This is expected as the bare GCE lacks any modification to enhance its electrochemical properties. The absence of significant redox peaks highlights the low sensitivity and conductivity of the bare electrode. The red curve corresponding to CeO_2/GCE exhibits a slight increase in current response ($\Delta\varphi=1.67\times10^{-5}$ A) compared to the bare GCE, indicating that the CeO_2 modification has introduced some electrochemical activity. Although redox peaks are present, the current is not significantly higher, suggesting limited improvement in sensitivity and conductivity with CeO_2 alone. In contrast, The green curve, representing rGO/GCE, shows a much higher current response compared to both the bare and CeO_2-modified GCE. This indicates that rGO significantly enhances the electrochemical activity due to its high electrical conductivity and large surface area. The redox peaks are more pronounced, but they are not perfectly symmetric, indicating some degree of irreversibility in the electrochemical process. The blue curve for CeO_2/rGO/GCE demonstrates the highest electron transform and current response among all tested electrodes, as the difference between 2 redox peak is $\Delta\varphi=6.67\times10^{-5}$ A. The pronounced redox peaks indicate enhanced electrochemical activity. The peaks, however, are more separated compared to rGO ($\Delta E_p = 0.08$V), and single CeO_2 ($\Delta E_p = 0.1$V) suggesting that the combination of CeO_2 and rGO introduces a larger potential difference between the anodic peak potential (E_{pa}) and the cathodic peak potential (E_{pc}). This larger separation ($\Delta E_p = 0.12$V, $E_{pa} = 0.31$ V, $E_{pc} = 0.19$ V) may be attributed to the synergistic effect between CeO_2 and rGO, which enhances electron transfer but also increases the potential window due to differing reaction kinetics.

The peak current increases with the addition of coatings, and the sensitivity and conductivity of the composite electrode (CeO_2/rGO/GCE) are higher than those of single coatings or the bare GCE electrode. This synergistic effect can be attributed to the combined properties of CeO_2 and rGO, where CeO_2 provides catalytic activity, and rGO offers high conductivity and surface area for electron transfer, which suggest that the CeO_2/rGO composite material significantly improves the electrochemical properties of the GCE, making it a promising candidate for electrochemical applications requiring high sensitivity and conductivity. The enhanced performance of the CeO_2/rGO/GCE electrode underscores the potential of this composite material in various sensing and catalytic applications.

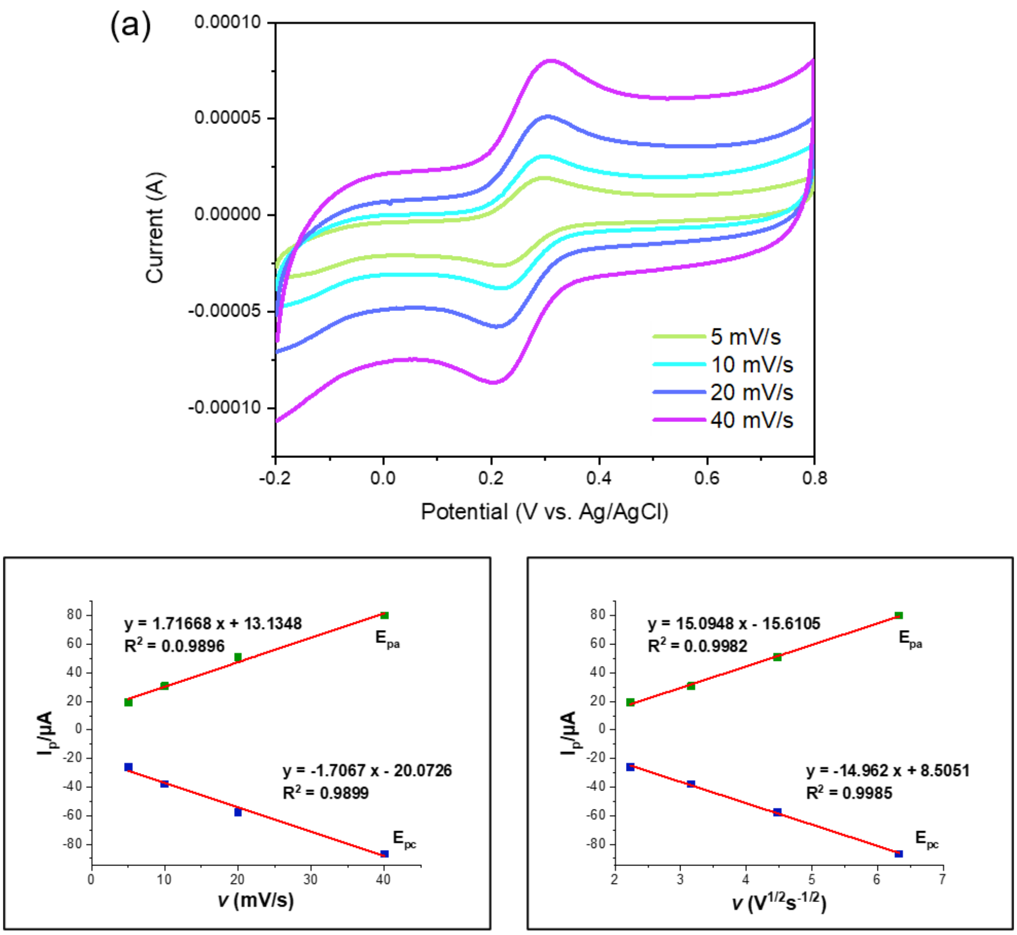

Figure 5-11. (a) Cyclic voltammetry plots of CeO$_2$/rGO/GCE (in 1:1 molar ratio) with increased scan rate (5, 10,20,40 mV/s)in the presence of 1 mM K$_3$[Fe(CN)$_6$] in 0.5 M KCl, (b) Redox peak (E$_{pa}$, E$_{pc}$) current as a function of scan rate with the liner fitting (c) Redox peak current as a function of the square root of scan rate with the liner fitting

Figure 5-11 illustrates the cyclic voltammetry (CV) responses of the CeO$_2$/rGO/GCE composite electrode at various scan rates (5, 10, 20, and 40 mV/s) in a 1 mM K$_3$[Fe(CN)$_6$] solution with 0.5 M KCl electrolyte. The potential range for the CV measurements is from -0.2 V to 0.8 V, and the scan rates influence the electrochemical behavior of the electrode significantly. As depicted in the CV curves, the peak currents for both anodic and cathodic processes increase with the scan rate. This increase in peak current with the scan rate suggests that processes such as charge transfer and proton transfer require a finite time to occur. At higher scan rates, these processes are not fully completed within the scanning period, resulting in higher peak currents. This behavior can be attributed to the limited electrolyte transport across the electrode surface, which leads to concentration polarization effects and restricts the full participation of active sites on the electrode surface in the electrochemical reaction.

The relationship between the peak current and scan rate is further analyzed in the insets of Figure 5-11. The linear relationship between the peak current and scan rate (Figure 5-11, b) indicates that the electrode process is controlled by a kinetic reaction mechanism. This is confirmed by the high correlation coefficient ($R^2 = 0.9985$ for E_{pc} and $R^2 = 0.9985$ for E_{pa}), demonstrating a strong linear dependence. In addition, the peak current plotted against the square root of the scan rate (Figure 5-11, c) also shows a linear relationship, suggesting that the electrode process is influenced by diffusion control. The high correlation coefficients ($R^2 = 0.9982$ for E_{pc} and $R^2 = 0.9985$ for E_{pa}) further support this observation. The diffusion-controlled behavior indicates that the rate of electron transfer is dependent on the diffusion of the electroactive species to the electrode surface. The CV analysis affected on the scan rates reveals that the CeO_2/rGO/GCE composite electrode exhibits both kinetic and diffusion-controlled behavior. The increase in peak current with scan rate, combined with the linear relationships observed in the insets, indicates effective electron transfer and high electrochemical activity of the composite material.

5.3.4 Sensitivity test of Ammonia by Modified Electrode Coating

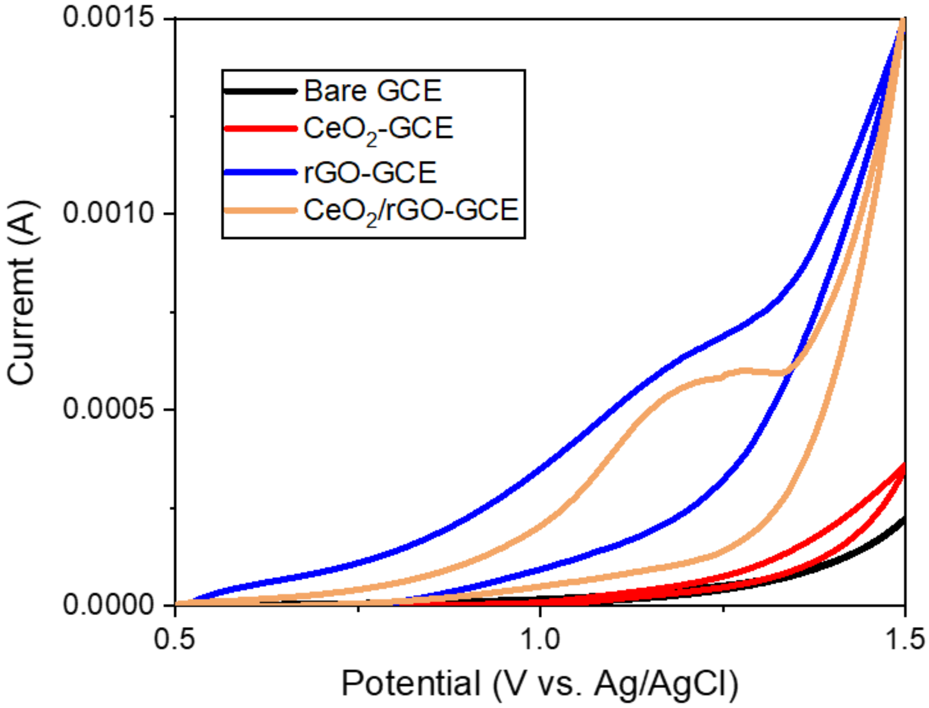

Figure 5-12. Cyclic voltammetry plots of GCE with different coatings (bare GCE, CeO_2/GCE, rGO/GCE, CeO_2/rGO/GCE) in the presence of 1 M NH^{4+} in 0.5 M KCl, with a scan rate of 20 mV/s

Figure 5-12 illustrates the cyclic voltammetry (CV) plots of glassy carbon electrodes (GCE) with different coatings (bare GCE, CeO_2/GCE, rGO/GCE, and CeO_2/rGO/GCE) in the presence of 1 M NH_4^+ in 0.5 M KCl, with a scan rate of 20 mV/s. The CV measurements were conducted to assess the electrochemical response of the electrodes to the target ion, NH^{4+}.

The black curve representing the bare GCE shows negligible current response, indicating no significant electrochemical reaction with NH_3. This suggests that the bare GCE lacks the necessary surface properties to interact effectively with the target gas, resulting in poor sensitivity. The red curve corresponding to CeO_2/GCE exhibits a slight increase in current response compared to the bare GCE. This indicates that CeO_2 modification introduces some electrochemical activity. However, the increase is not substantial, suggesting that CeO_2 nanoparticles don't have a direct oxidation reaction with the target ion, indicating zero enhancement of the sensitivity to NH^{4+}, though it aids in modifying the electrode's conductivity. The green curve for rGO/GCE demonstrates a much higher current response compared to both the bare and CeO_2-modified GCEs. This indicates that rGO enhances the electrochemical activity due to its high electrical conductivity and large surface area, facilitating better interaction with NH^{4+}. The anodic peak (E_{pa}) for rGO/GCE is observed at 6.34×10^{-4} A at 1.19 V, indicating effective electron transfer and interaction with the target gas. However, the peaks are not perfectly symmetric, indicating some degree of irreversibility in the electrochemical process, and the current value keeps increasing with the potential increasing, the This inconspicuous oxidation peak indicates that rGO is insensitive to the oxidation reaction of NH^{4+}, which also indicates its weak sensing performance. The blue curve for CeO_2/rGO/GCE shows the highest current response among all tested electrodes, with an anodic peak (E_{pa}) at 6.01×10^{-4} A at 1.28 V. The clear and pronounced redox peaks indicate enhanced electrochemical activity, attributed to the synergistic effect between CeO_2 and rGO. The rGO sheets provide catalytic activity, while the CeO_2 nanoparticles offer high conductivity and a large surface area for electron transfer. This combination results in high sensitivity and clear peak detection of NH^{4+}.

These cyclic voltammetry plots reveal that the CeO_2/rGO/GCE composite electrode exhibits superior electrochemical properties, making it a promising candidate for applications requiring high sensitivity and conductivity in electrochemical sensors. The enhanced performance is due to the synergistic effect of combining CeO_2 and rGO, which improves electron transfer and interaction with the NH^{4+} ion.

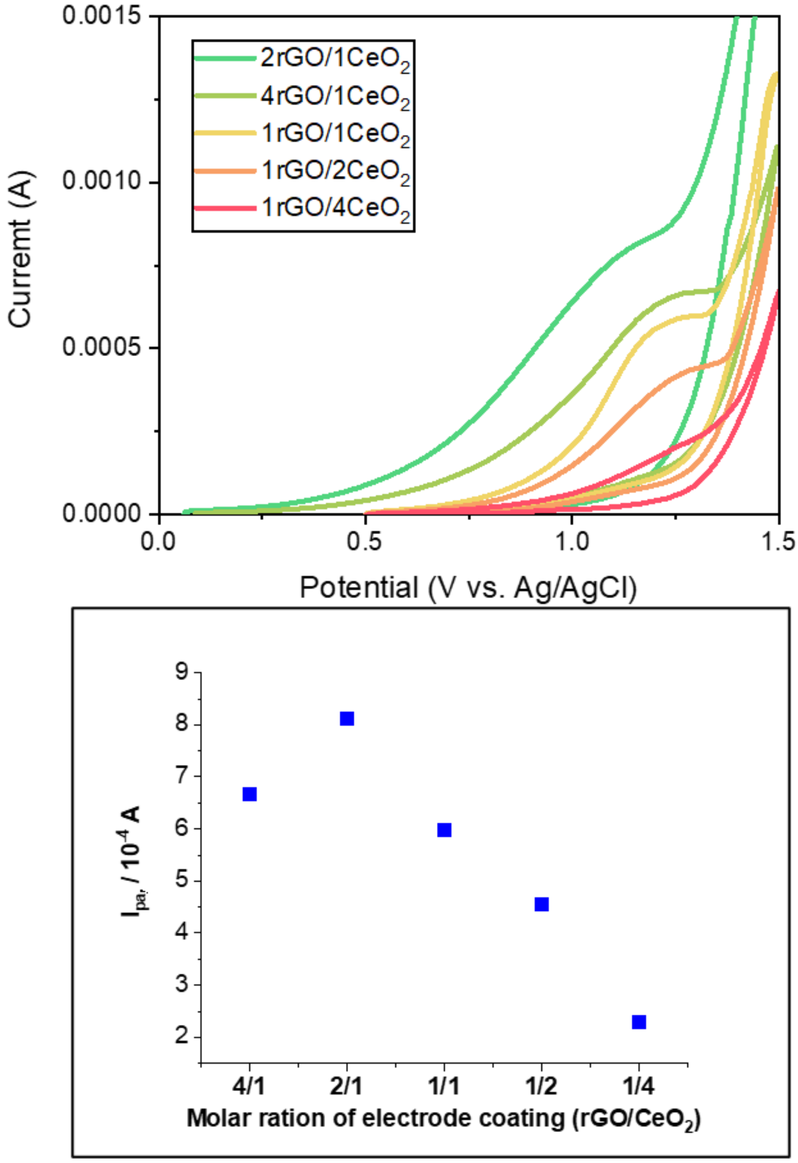

Figure 5-13. Cyclic voltammetry plots of CeO_2/rGO/GCE in different molar ratios (rGO/CeO_2 = 4:1, 2:1, 1:1, 1:2, 1:4) in the presence of 1 M NH^{4+} in 0.5 M KCl, scan rate at 20 mV/s (b) Anodic peak current (I_{pa}) value of each composite ratio

Figure 5-13 presents the cyclic voltammetry (CV) plots of glassy carbon electrodes (GCE) coated with various CeO_2/rGO nanocomposite ratios (2rGO/1CeO_2, 4rGO/1CeO_2, 1rGO/2CeO_2, 1rGO/4CeO_2) in the presence of 1 M NH^{4+} in 0.5 M KCl, with a scan rate of 20 mV/s. The CV measurements were conducted to examine the electrochemical response and performance of the different nanocomposite ratios in detecting ammonia.

The green curve, representing the 2rGO/1CeO_2 ratio, exhibits the highest current response among the tested ratios. This indicates that this particular ratio provides the most effective combination of rGO and CeO_2, enhancing the electrochemical activity and sensitivity to NH_3. The high current response suggests a strong synergistic effect, where the high surface area and conductivity of rGO, combined with the catalytic properties of CeO_2, facilitate efficient electron transfer. The light green curve for the 4rGO/1CeO_2 ratio also shows a significant current response, albeit slightly lower than the 2rGO/1CeO_2 ratio, but higher than single rGO coating as shown in Figure 5-12. The yellow and orange curves, representing the 1rGO/2CeO_2 and 1rGO/4CeO_2 ratios, respectively, exhibit moderate current responses. These results indicate that increasing the CeO_2 content beyond a certain point may not provide additional benefits and could potentially hinder the electrochemical performance due to possible agglomeration and low sensitivity of CeO_2 nanoparticles. The red curve, corresponding to the 1rGO/4CeO_2 ratio, shows the lowest current response among the tested ratios. This suggests the CeO_2 nanoparticles leading no oxidation reaction with the NH^{4+} ion, as suggest in Figure 5-12.

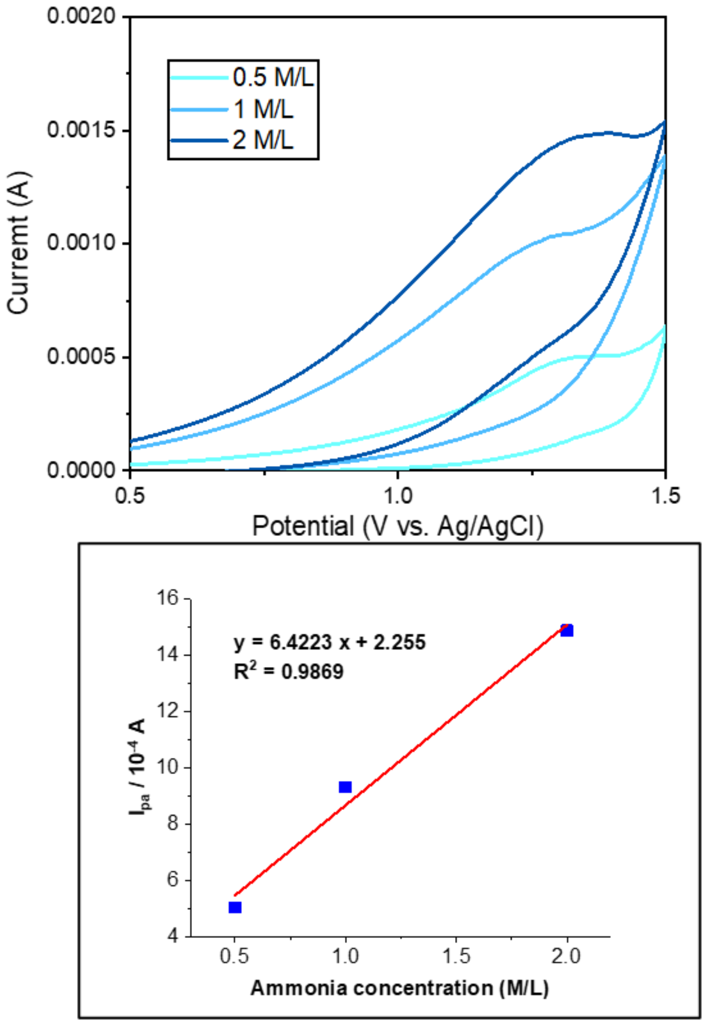

Figure 5-14. (a) Cyclic voltammetry plots of CeO_2/rGO/GCE (in 1:1 molar ratio) in the presence of increased ammonia concentration (0.5, 1, 2 M/L) in 0.5 M KCl solution, (b) Anodic peak current (I_{pa}) as a function of ammonia concentration with the liner fitting

Figure 5-14 illustrates the cyclic voltammetry (CV) plots of CeO_2/rGO/GCE (in a 1:1 molar ratio) in the presence of increased ammonia concentrations (0.5, 1, and 2 M/L) in 0.5 M KCl, and the corresponding anodic peak current (I_{pa}) as a function of ammonia concentration with linear fitting. In Figure 5-14 (a), the CV plots display the electrochemical response of the CeO_2/rGO/GCE electrode with varying ammonia concentrations. As the concentration of ammonia increases from 0.5 M/L to 2 M/L, the current response also increases significantly. This indicates a strong interaction between the ammonia molecules and the CeO_2/rGO nanocomposite, which enhances the electron transfer process. The increased current response suggests that the electrode is highly sensitive to changes in ammonia concentration. Figure 5-14 (b) shows the relationship between the anodic peak current (I_{pa}) and the ammonia concentration. The data points exhibit a clear linear trend, which is confirmed by the linear fitting. The linear relationship demonstrates that the peak current increases proportionally with the concentration of ammonia, indicating that the electrode's response is directly related to the amount of ammonia present in the solution. This linearity is crucial for practical sensing applications, as it allows for accurate quantification of ammonia concentration based on the measured current. The enhanced current response and linearity in the CV analysis highlight the effectiveness of the CeO_2/rGO/GCE electrode for ammonia detection. The high sensitivity and linear response make this nanocomposite electrode a promising candidate for applications in ammonia sensing, providing reliable and accurate measurements in various environmental and industrial settings.

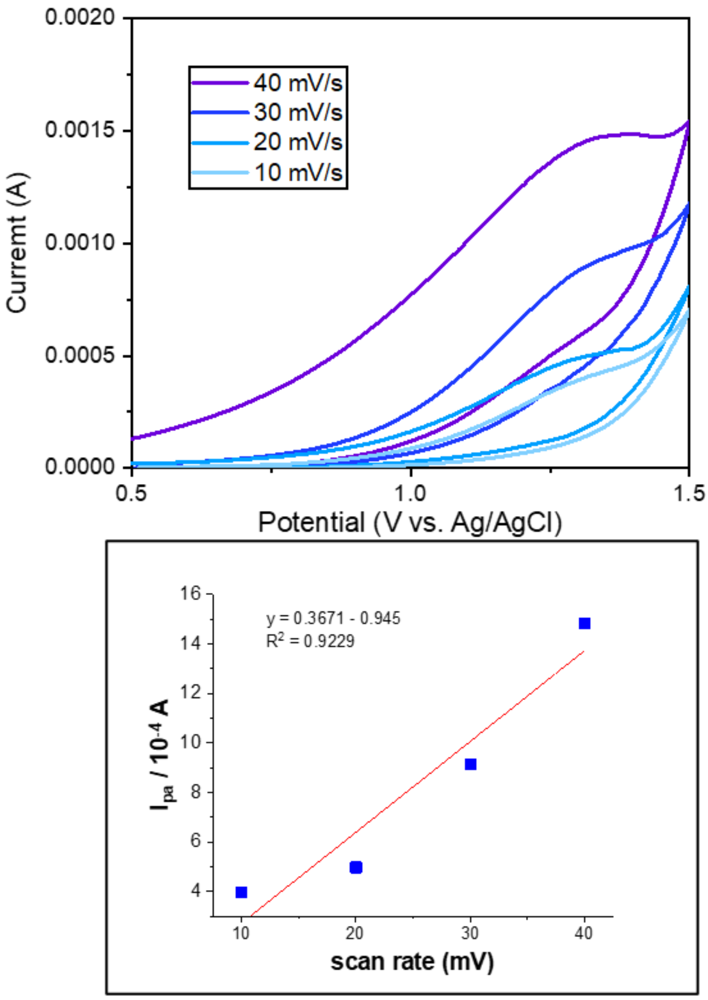

Figure 5-15. (a) Cyclic voltammetry plots of CeO_2/eGO/GCE (in 1:1 molar ratio) with increased scan rate (10, 20, 30, 40 mV/s) in the presence of 1 M/L in 0.5 M KCl, (b) Anodic peak current (I_{pa}) as a function of ammonia concentration with the liner fitting

Figure 5-15 illustrates the cyclic voltammetry (CV) plots of CeO_2/rGO/GCE (in a 1:1 molar ratio) with increased scan rates (10, 20, 30, and 40 mV/s) in the presence of 1 M/L ammonia in 0.5 M KCl and the corresponding anodic peak current (I_{pa}) as a function of scan rate with linear fitting. In Figure 5-15(a), the CV plots display the electrochemical response of the CeO_2/rGO/GCE electrode with varying scan rates. As the scan rate increases, the current response also increases significantly. This indicates that the electrode is capable of responding to changes in scan rate, which is an essential characteristic of dynamic sensing applications. The anodic peak current (I_{pa}) increases with increasing scan rate, showing a more pronounced peak at higher scan rates. Figure 5-15 (b) shows the relationship between the anodic peak current (I_{pa}) and the scan rate. The data points exhibit a clear linear trend, which is confirmed by the linear fitting. The linear relationship demonstrates that the peak current increases proportionally with the scan rate, indicating that the electrode process is controlled by surface reaction kinetics.

5.4 Summary

This chapter investigates the electrochemical properties of CeO_2 nanoparticles (NPs) in modifying reduced graphene oxide (rGO) glassy carbon electrodes (GCE) for enhanced ammonia detection. It underscores the importance of monitoring ammonia levels in biomedical applications, particularly for patients with liver diseases, where elevated ammonia can lead to severe conditions such as hepatic encephalopathy. To address this, a CeO_2/rGO/GCE electrode is developed to improve sensitivity and specificity in detecting ammonia. Graphene oxide (GO) is reduced to rGO through sintering and ultrasonication, enhancing its electrical conductivity and surface area, making it an ideal material for gas sensing. The combination of CeO_2 and rGO creates a synergistic effect, enhancing redox reactions and uniform dispersion, thus improving the overall performance of the ammonia sensor.

The experimental analysis involved synthesizing CeO_2-rGO nanocomposites and characterizing their morphology and electrochemical properties using techniques such as X-ray diffraction (XRD), scanning electron microscopy (SEM), energy-dispersive X-ray spectroscopy (EDS), ultraviolet-visible (UV-Vis) spectroscopy, and cyclic voltammetry (CV). The XRD patterns confirmed the successful integration of CeO_2 into the rGO matrix, maintaining the cubic fluorite structure of CeO_2 and showing reduced interlayer spacing in rGO. SEM images demonstrated morphological transitions from GO to rGO, with further refinement and uniform dispersion of CeO_2 nanoparticles in the rGO matrix. EDS mapping validated the uniform distribution of CeO_2 on rGO sheets. UV-Vis spectroscopy and Tauc plots revealed a decrease in the energy band gap with increasing CeO_2 content, indicating enhanced electrical conductivity. The linear relationship between CeO_2 ratio and band gap reduction supports the improved electrical properties of the nanocomposite, making it suitable for electronic applications.

Cyclic voltammetry (CV) tests demonstrated that the CeO_2/rGO/GCE composite electrode exhibited superior electrochemical behavior, with enhanced electron transfer and higher sensitivity compared to single coatings or bare electrodes. The CV plots showed pronounced redox peaks and a higher current response for the composite electrode, confirming the synergistic effect between CeO_2 and rGO. Sensitivity tests for ammonia detection indicated that the CeO_2/rGO/GCE electrode exhibited the highest current response among different coatings, with the optimized ratio of 2rGO/1CeO_2 providing the most effective electrochemical activity. The electrode displayed a strong linear relationship between peak current and ammonia concentration, confirming its high sensitivity and practical applicability for real-time monitoring. Additionally, increasing scan rates further enhanced the current response, indicating the electrode's capability for dynamic sensing applications. Overall, this study highlights the potential of CeO_2/rGO nanocomposites for advanced sensing applications, particularly in biomedical fields for real-time ammonia monitoring and environmental monitoring, due to their improved sensitivity, conductivity, and robust performance.

References

[135] K.E. Wyer, D.B. Kelleghan, V. Blanes-Vidal, G. Schauberger, T.P. *J. Environ. Manage*., 323 (2022) 116285.

[136] N.T. Brannelly, J.P. Hamilton-Shield, A.J. Killard. *Crit. Rev. Anal. Chem.*, 46, 6 (2016) 490.

[137] P. Ott, H. Vilstrup. *Metab. Brain Dis*., 29 (2014) 901.

[138] M. Holecek. *Nutr.*, 31, 1 (2015) 14.

[139] R.F. Butterworth. *Metab. Brain Dis*., 17 (2002) 221.

[140] A. Watanabe. J. Gastroenterol. *Hepatol.*, 13, 7 (2008) 752.

[141] L. Zieve. Metab. *Brain Dis*., 2 (1987) 147.

[142] M. Mazelis. Amino Acid Catabolism. In B.J. Miflin (Ed.), *Academic Press* (1980) 541.

[143] W. Weppner. *Sensors Actuators*, 12, 2 (1987) 107.

[144] R. Hanafi, R.D. Mayasari, Masmui, Agustanhakri, J. Raharjo, R. Nuryadi. *AIP Conf. Proc.,* 2169 (2019) 030007.

[145] S.S. Bhoga, K. Singh. *Ionics,* 13 (2007) 417.

[146] E. Gorbova, F. Tzorbatzoglou, C. Molochas, D. Chloros, A. Demin, P. Tsiakaras. *Catalysts*, 12, 1 (2022) 1.

[147] T. Zhang, M.B. Nix, B.-Y. Yoo, M.A. Deshusses, N.V. Myung. *Electroanalysis*, 18, 12 (2006) 1153.

[148] T. Hibino, S. Kakimoto, M. Sano. *J. Electrochem. Soc*., 146 (1999) 3361.

[149] M.M. Shahid, P. Rameshkumar, A. Pandikumar, H.N. Lim, Y.H. Ng, N.M. Huang. *J. Mater. Chem. A,* 3 (2015) 14458.

[150] H. Beitollahi, F.G. Nejad. *Electroanalysis,* 28 (2016) 2237.

[151] S. Yang, B. Xu, J. Zhang, X. Huang, J. Ye, C. Yu. *J. Phys. Chem.*, 114 (2010) 4389.

[152] C.R. Minitha, V.S. Anithaa, V. Subramaniam, R.T.R. Kumar. *ACS Omega*, 3 (2018) 4105.

[153] X. Wang, X. Li, Y. Zhao, Y. Chen, J. Yu, J. Wang. *RSC Adv.*, 6 (2016) 52339.

[154] M. Fathy, A. Gomaa, F.A. Taher. *J. Mater. Sci.*, 51 (2016) 5664.

[155] A. Ahmed, A. Singh, S. Young, V. Gupta, M. Singh, S. Arya. *Compos. Part A Appl.*, 165 (2023) 107373.

[156] L.G. Guex, B. Sacchi, K.F. Peuvot, R.L. Andersson, A.M. Pourrahimi, V. Ström, S. Farris, R.T. Olsson. *Nanoscale*, 9 (2017) 9562.

[157] G. Di Filippo, A. Liscio, A. Ruocco. *Appl. Surf. Sci.*, 512 (2020) 145605.

[158] F. Li, J. Li, Z. Cao, X. Lin, X. Li, Y. Fang, X. An, Y. Fu, J. Jin, R. Li. *J. Mater. Chem. A,* 3 (2015) 21772.

[159] A. Apicella, R. Aversa, F.I.T. Petrescu. Am. *J. Eng. Appl. Sci.*, 11, 2 (2018) 766.

[160] N.S. Rajput, S. Al Zadjali, et al. *RSC Adv.*, 11 (2021) 27381.

[161] M. Neek-Amal, F.M. Peeters. *Appl. Phys. Lett.*, 104, 17 (2014) 173106.

[162] W.J. Yu, L. Liao, S.H. Chae, Y.H. Lee, X. Duan. *Nano Lett.*, 11, 11 (2011) 4759.

[163] B. Chen, L. Huang, X. Ma, L. Dong, Z. Zhang, L.-M. Peng. *Carbon,* 94 (2015) 585.

[164] N.S. Suhaimin, M.F.R. Hanifah, M. Azhar, J. Jaafar, M. Aziz, A.F. Ismail, M.H.D. Othman, M.A. Rahman, F. Aziz, N. Yusof, R. Mohamud. *Mater. Chem. Phys.*, 278 (2022) 125629.

[165] C. Vacacela Gomez, E. Robalino, D. Haro, T. Tene, P. Escudero, A. Haro, J. Orbe. *Mater. Today Proc.*, 3, 3 (2016) 796.

[166] A. Riaz, A. Usman, M. Faheem, Z. Hussain, A.N. Khan, S. Soomro. *Int. J. Electrochem. Sci.*, 12, 3 (2017) 1785.

[167] M.T.U. Malik, A. Sarker, S.M.S.M. Rahat, S.B. Shuchi. *Mater. Today Commun.*, 28 (2021) 102685.

[168] B. Gupta, N. Kumar, K. Panda, et al. *Sci. Rep.*, 7 (2017) 45030.

[169] T. Kuila, A.K. Mishra, P. Khanra, N.H. Kim, J.H. Lee. *Nanoscale*, 5 (2013) 52.

[170] J.D. Renteria, S. Ramirez, H. Malekpour, B. Alonso, A. Centeno, A. Zurutuza, A.I. Cocemasov, D.L. Nika, A.A. Balandin. *Adv. Funct. Mater.*, 25 (2015) 4664.

[171] J. Saranya, P. Saminathan, S.R. Ankireddy, M.R. Shaik, M. Khan, B. Shaik.

Biomedicines, 11 (2023) 531.

[172] S. Ida, P. Wilson, B. Neppolian, M. Sathish, A.R.M. Shaheer, P. Ravi. *Ultrason. Sonochem.*, 64 (2020) 104866.

[173] M.F. Zainuddin, et al. *IOP Conf. Ser.: Mater. Sci. Eng.*, 358 (2018) 012046.

[174] S.G. Babu, P. Karthik, M.C. John, S.K. Lakhera, M. Ashokkumar, J. Khim, B. *Neppolian. Ultrason. Sonochem.*, 50 (2019) 218.

[175] R. Karthika, M. Govindasamy, S. Chen, T. Chena, J.V. Kumar, A. Elangovan, V. Muthuraj, M. Yu. *RSC Adv.*, 7 (2017) 25702.

[176] S. Panda, V. Marla, V.S. Aditya, V.S. Sarma. *Sustain. Energy Fuels*, 5 (2021) 4414.

[177] Y. Liu, J.S. Xue, T. Zheng, J.R. Dahn. *Carbon*, 34 (1996) 193.

[178] R. Phillips, K. Jolley, Y. Zhou, R. Smith. *Carbon Trends*, 5 (2021) 100124.

[179] R. Pasricha, S. Gupta, A.K. Srivastava. *Small*, 5 (2009) 2253.

[180] C. Zhao, Q. Wang, H. Zhang, S. Passerini, X. Qian. *ACS Appl. Mater. Interfaces*, 8 (2016) 15661.

[181] P.V. Tuan, H.B. Tuong, V.T. Tan, L.H. Thu, N.D. Khoang, T.N. Khiem. *Opt. Mater.*, 123 (2022) 111916.

Chapter 6

General Conclusion

6.1 Conclusion

This dissertation comprehensively explored the synthesis, characterization, and application of cerium oxide (CeO_2) nanoparticles (NPs) with a focus on enhancing UV protection and biosensor technologies. The primary objectives were to investigate the effects of laser parameters on CeO_2 NPs synthesis via the Laser Ablation in Liquid (LAL) method, compare this method with traditional chemical methods, and optimize the application of 2 NPs in electrochemical sensors. The research findings provided significant insights into the optimal conditions for producing high-quality CeO_2 NPs and their practical applications.

6.1.1 Synthesis of CeO_2 Nanoparticles

CeO_2 nanoparticles were successfully synthesized using the LAL method, demonstrating several advantages over traditional methods such as chemical precipitation. By varying the irradiation parameters, including laser fluence, irradiation time, and suspension concentration, CeO_2 NPs with controlled sizes and high uniformity were achieved. Specifically, the study revealed that increasing the laser fluence and irradiation time resulted in smaller primary nanoparticles with improved sphericity and reduced aggregation. The average primary particle size decreased from 150 nm to approximately 50 nm as the laser fluence increased, showcasing the ability of the LAL method to produce nanoparticles with precise size control.

Furthermore, this research confirmed that the LAL method can produce CeO_2 NPs with a high degree of crystallinity and fewer impurities compared to those synthesized by traditional chemical methods. The X-ray diffraction (XRD) analysis showed distinct diffraction peaks corresponding to the cubic fluorite structure of CeO_2, indicating the successful synthesis of highly crystalline nanoparticles.

6.1.2 Morphological and Optical Properties

The morphology of the synthesized CeO_2 nanoparticles was thoroughly analyzed using Scanning Electron Microscopy (SEM) and Dynamic Light Scattering (DLS). The results indicated that higher laser fluences and longer irradiation times led to the formation of more spherical and uniformly sized nanoparticles. SEM images revealed a transition from irregularly shaped particles at lower fluences to well-defined spherical nanoparticles at higher fluences. The particle size distribution analysis confirmed a narrower size distribution for nanoparticles synthesized at optimal laser parameters.

The UV absorption properties of CeO_2 NPs were significantly influenced by the laser synthesis parameters. The UV-vis spectra demonstrated that CeO_2 NPs synthesized at higher fluences exhibited enhanced UV absorption capabilities, particularly in the UVA range. This was attributed to the quantum size effect, where smaller nanoparticles showed a wider bandgap, thereby enhancing their UV-blocking properties. The absorption spectra indicated a shift towards shorter wavelengths as the particle size decreased, confirming the effective tuning of optical properties through laser parameters.

6.1.3 Comparative Analysis with Traditional Methods

A comparative analysis between the LAL method and the traditional precipitation method was conducted to evaluate the efficiency and quality of CeO_2 NPs production. The LAL method produced nanoparticles with higher purity, uniformity, and spherical morphology compared to the precipitation method, which resulted in irregularly shaped and aggregated particles. The focused laser ablation technique proved to be superior in achieving a high yield of uniformly sized CeO_2 NPs, highlighting its potential for scalable and efficient nanoparticle production. In addition to morphological advantages, the LAL method demonstrated superior control over the chemical composition of the nanoparticles. This purity is critical for applications in UV protection and biosensors where the presence of impurities can significantly affect performance.

6.1.4 UV Protection Applications

The UV absorption studies confirmed that CeO_2 NPs possess excellent UV-blocking properties, making them suitable for UV protection applications. The nanoparticles demonstrated a broad absorption range and high absorption peaks in both UVB and UVA regions. Compared to other UV filtering material, CeO_2 NPs offered a wider absorption range and higher UV absorption efficiency, positioning them as superior candidates for developing advanced UV protection materials, including sunscreens and protective coatings.

The effectiveness of CeO_2 NPs in UV protection was further validated through in vitro UV exposure tests, where the nanoparticles provided significant protection to UV-sensitive substrates. The incorporation of CeO_2 NPs into polymer matrices showed improved UV stability and prolonged the lifetime of the polymers under UV exposure, highlighting their practical applicability in protective coatings.

6.1.5 Application in Electrochemical Sensors

The synthesized CeO_2 NPs were employed to modify the glassy carbon electrode

(GCE) by creating a CeO_2/rGO composite. This modification aimed to enhance the sensitivity of the GCE for ammonia (NH^{4+}) detection. Cyclic voltammetry (CV) studies revealed that the CeO_2/rGO/GCE composite exhibited significantly improved electrochemical performance compared to bare GCE, CeO_2/GCE, and rGO/GCE electrodes. The synergistic effect between CeO_2 and rGO was evident, as the composite showed higher current responses and better redox peak separation, indicating enhanced electron transfer and conductivity.

The anodic peak current (I_{pa}) was linearly related to the scan rate, confirming that the electrode process was controlled by diffusion, which is essential for high-sensitivity electrochemical sensors. Additionally, the presence of CeO_2 improved the stability and reproducibility of the electrochemical signals, making the CeO_2/rGO/GCE composite a robust platform for ammonia detection. The successful reduction of graphene oxide to rGO and its effective doping with CeO_2 nanoparticles were confirmed by SEM-EDS mapping, which showed a uniform distribution of CeO_2 on the rGO surface.

6.1.6 Summary

In summary, this dissertation successfully achieved its objectives by demonstrating the advantages of the LAL method in synthesizing high-quality CeO_2 nanoparticles, optimizing their morphological and optical properties, and enhancing their application in UV protection and electrochemical sensors. The research provided valuable insights into the synthesis process, established the superiority of the LAL method over traditional chemical methods, and showcased the practical applications of CeO_2 NPs in improving UV protection and biosensor technologies.

The findings contribute to the advancement of CeO_2-based nanotechnologies and open new avenues for their application in various scientific and industrial fields. The LAL method's ability to produce nanoparticles with controlled size, high purity, and enhanced properties presents a promising approach for scalable and environmentally friendly nanoparticle production. Additionally, the improved electrochemical performance of CeO_2/rGO composites underscores their potential in developing high-sensitivity sensors for environmental monitoring and healthcare applications. These advancements highlight the significance of CeO_2 NPs in addressing current technological challenges and promoting the development of next-generation materials and devices.

6.3 Prospect

The outcomes of this research lay a strong foundation for future explorations and advancements in the field of nanotechnology, particularly concerning the synthesis and application of CeO_2 nanoparticles. Several promising prospects emerge from the findings of this study.

The successful application of the Laser Ablation in Liquid (LAL) method for synthesizing CeO_2 nanoparticles opens up new possibilities for refining and optimizing this technique. Future research can focus on further tuning the laser parameters to achieve even finer control over nanoparticle size and morphology. Additionally, exploring the use of different liquid environments and target materials in the LAL process could expand the range of nanoparticles that can be synthesized using this method. The scalability of LAL for industrial applications also presents a significant area for investigation, aiming to develop cost-effective and high-throughput production processes for high-quality nanoparticles.

The demonstrated UV absorption capabilities of CeO_2 nanoparticles highlight their potential in advanced material applications beyond traditional UV protection. Future studies could explore their integration into a variety of polymer matrices to develop advanced composites with superior UV resistance and mechanical properties. This could lead to the creation of more durable and efficient UV protective coatings, sunscreens, and other related products. Moreover, the unique properties of CeO_2 nanoparticles could be leveraged in developing materials for other applications such as photocatalysis, energy storage, and environmental remediation.

The research has established the CeO_2/rGO composite as an effective material for enhancing the sensitivity of electrochemical sensors. Building on this, future research can explore the development of a broader range of biosensors using CeO_2 nanoparticles. Investigating the potential of these sensors for detecting various analytes, such as heavy metals, glucose, and other biomarkers, could significantly impact environmental monitoring and healthcare diagnostics. The integration of CeO_2 nanoparticles with other nanomaterials could also lead to the development of multifunctional sensors with enhanced performance characteristics. The observed synergistic effects between CeO_2 and rGO in enhancing the electrochemical performance of sensors pave the way for exploring other nanoparticle combinations. Future studies could investigate the synergistic interactions between CeO_2 and other conductive materials, such as carbon nanotubes, metal oxides, and conductive polymers. Understanding these interactions could lead to the design of novel composite materials with tailored properties for specific applications. Additionally, studying the mechanisms behind these synergistic effects at the molecular level could provide deeper insights into the design principles for advanced nanocomposites.

As the use of CeO_2 nanoparticles expands, it becomes crucial to assess their environmental and health impacts comprehensively. Future research should focus on understanding the toxicity, bioaccumulation, and environmental fate of CeO_2 nanoparticles. Developing eco-friendly synthesis methods and conducting thorough risk assessments will be essential for ensuring the safe and sustainable use of these nanoparticles in various applications. Collaborations between material scientists, toxicologists, and environmental scientists will be key to addressing these challenges and promoting the responsible development of nanotechnologies. The findings of this research underscore the importance of interdisciplinary approaches in advancing nanotechnology. Future work should continue to foster collaborations between physicists, chemists, materials scientists, and engineers to drive innovation. Interdisciplinary research initiatives can facilitate the development of new methodologies, enhance the understanding of fundamental processes, and accelerate the translation of laboratory discoveries into practical applications. Engaging with industry partners can also help align research objectives with real-world needs and promote the commercialization of advanced nanomaterials.

In conclusion, this research has made significant contributions to the field of nanotechnology by demonstrating the potential of CeO_2 nanoparticles synthesized through the LAL method for various applications. The prospects outlined here provide a roadmap for future research endeavors, aiming to harness the full potential of CeO_2 nanoparticles and contribute to the development of innovative materials and technologies that address pressing global challenges.

Acknowledgment

First and foremost, I would like to express my deepest gratitude to my advisor, Professor Wada. His kind teaching, gentle demeanor, and rigorous, realistic attitude toward scientific research have profoundly influenced my work, instilling in me better behavior and confidence in my results. His modesty and politeness have greatly alleviated the pressures of my doctoral studies, and he has been an invaluable support throughout this journey.

I would like to offer my special thanks to Professor Kitamoto, Professor Nakamura, Professor Hosoda, and Professor Hayashi for reviewing my thesis and providing invaluable advice.

I am particularly grateful to Professor Arai for his support with the CV test, including lending equipment and offering advice. I also extend my gratitude to Professor Kitamoto and Professor Hara for their assistance with the DLS measurements in my first and second experiments, respectively. My heartfelt thanks also go to Mrs. Katsumi Suda from the Analysis Center at Suzukakedai campus, Tokyo Tech, for her help with XRD analysis.

I would like to thank all the members of the Wada Laboratory. Without their company and assistance, my path to graduation would not have been as smooth. They have taken great care of me both in life and in my studies. My Japanese peers often helped me overcome language barriers, and my international peers provided companionship throughout my school life. In particular, Mrs. Wang and Mrs. Tei have been my greatest support, offering guidance and assistance that have been crucial to my success. Their friendship is one of the most important rewards of joining the Wada Lab. The positive and healthy atmosphere in the Wada Lab has made my PhD journey free of academic pressure, allowing me to enjoy this period in a healthy and happy manner. I am deeply grateful for the opportunity to be a part of this wonderful group.

I would like to thank my family. Their support has been crucial, not only materially but also spiritually. My family has provided great encouragement and understanding during my doctoral studies, especially my mother and grandmother. They have given me all their love and have been with me through my weakest moments. Their wisdom and tolerance have set high standards for my life and have taught me to be independent and fearless. I also thank my father for igniting my interest in science from a young age, and my boyfriend for his understanding and patience while I studied abroad. In particular, I want to thank my grandfather. His achievements as a medical professor and his passion for his career have been a role model for me, one that I will pursue and strive to emulate throughout my life.

I would also like to thank my friends for their company and for making me laugh all the time. I am also grateful to the group of friends who lived with me in Chuorinkan: Dr. Wang, Dr. Liu, Dr. Xie, and Mrs. Wang from Tokyo Tech. Their companionship and support were the most enjoyable parts of my life abroad. I also thank my old friend Dr. Liu from UNC, who has provided remote support and advice for my research. Additionally, I want to express my gratitude to my pet parrot, Tietie, who stayed up with me every night and brought me joy, becoming an indispensable companion in my PhD journey.

Finally, I want to thank myself for maintaining an open and learning mindset, for embracing everything with acceptance, and for enduring countless nights to meet deadlines. I am incredibly fortunate to have encountered all the people surrounding me who have supported and preserved my sense of self, allowing my life to progress steadily and keep my life in linear regression. I am grateful to be an ordinary person, and I hope to stay true to myself, maintain my sense of normalcy, and continue to passionately pursue the career and life I love.

At last, I extend my gratitude to Tokyo Tech for providing a valuable platform for learning, high-quality interpersonal relationships, and lifelong friends. Though it can only exist independently till my graduation, I hope that the merged entity, Science Tokyo, will grow stronger and strive to reach the QS Top 50!